Politecnico di Torino

Corso di laurea in ingegneria aerospaziale
Anno accademico 2022/2023
Sessione di laurea Ottobre 2023

Fluid-structure interaction of two inverted flags in echelon formation

RELATORI:
Prof. Marco Petrolo
Prof. Matteo Filippi

RELATORE ESTERNO:
Prof. Vrishank Raghav

CANDIDATO:
Antonio Di Paolo
Matricola: 288825

A mamma e papà

Acknowledgements

I want to thank professors Marco Petrolo and Matteo Filippi for their constant support during this project. A big thanks goes to professor Vrishank Raghav and the Applied Fluid Research Group at Auburn University who taught me so many things in so few time. Finally I want to thank my family, because without them I would have not been able to accomplish this goal.

Abstract

Lately piezoelectric energy harvesters became very popular for micro electro-mechanical systems (MEMS) applications because of their reliability and long operating life. One particular configuration turned out to be extremely advantageous for extracting energy from fluid flows naturally occurring in the environment by using these devices, the inverted flag. This investigation aims at optimizing the efficiency of two slender inverted flags in a tandem echelon configuration, which was inspired by formation flight. The results can potentially help designing a farm of harvesters to scale this technology to applications which require higher electrical power than MEMS. So far only 2D arrangements of multiple inverted flags have been studied and reported in the literature, but when it comes to practice all of the three spatial dimensions have to be considered. The results show that an overlapping of the two flags between 0% and 50% of their width in the transverse direction to the undisturbed fluid flow velocity causes a drop of the performance of the rear flag of the formation. On contrary the same overlap turns out to be the most beneficial to birds and aircraft close formation flight. Finally the highest efficiency of the whole configuration is measured when the rear flag is far away from the frontal flag in the transverse direction to the undisturbed fluid flow velocity.

Contents

Chapter 1

Introduction

Fluid structure interactions (FSI) of flags immersed in a fluid flow have received much interest for giving insights both in natural phenomena and industrial applications. In principle the main reason was to understand how to get rid of flow induced vibrations, as an example the stability of plates within a flow characterizes panel flutter and wing divergence in aeronautics and the integrity of nuclear plants' cores in nuclear engineering ([12] and [13]). But recently the dynamics of the unstable flag turned out to be useful to better understand some natural phenomena, like propulsion of aquatic animals and snoring induced by the soft palate in human airways.

1.1 Flag applications

At present the main engineering fields for flag application are three:

1. energy harvesting;

2. heat transfer enhancement;

3. mixing enhancement.

Other recent areas of study regarding flags' applications concern bluff bodies' drag reduction by means of wake modification [10] and waves absorption for shores' protection and energy harvesting [31].

1.1.1 Energy harvesting

Usually flag energy harvesting is meant to power micro electronic systems because the output power range is usually low, this aspect is not directly related to the efficiency of the device, instead it is linked to the difficult scalability of this technology to large applications, in fact in this last case there is the need of much free space for both the harvester and the supporting structure, a typical large application is the extraction of energy from ocean waves [40]. The conversion of energy from vibrations to electricity happens through either deformation-based or displacement-based mechanism.
Conversion by means of piezoelectric material is a deformation-based process, stretching and compression of the membrane due to the local curvature of the flags induce charge transfer between different points of the piezoelectric device, this is known as the piezoelectric effect. Instead displacement-based conversion can be implemented by using a magnetic element mounted on the flag which moves with respect to a conductor, the variation of the magnetic flux through the conductor generates an induced current, a concept is presented in [39]. Another technique involved in displacement-based energy harvesting is to exploit the triboelectric effect, triboelectricity is the phenomenon through which it is possible to load a potential difference by rubbing two different materials, one of which is an insulator. By using this method the dynamics of the flag will be affected by the presence of the surface with whom the rubbing will occur.
Figure 1.1 depicts the typical energy conversion, storage and terminal user for the energy harvesting applications of flags. The flag configurations which are represented
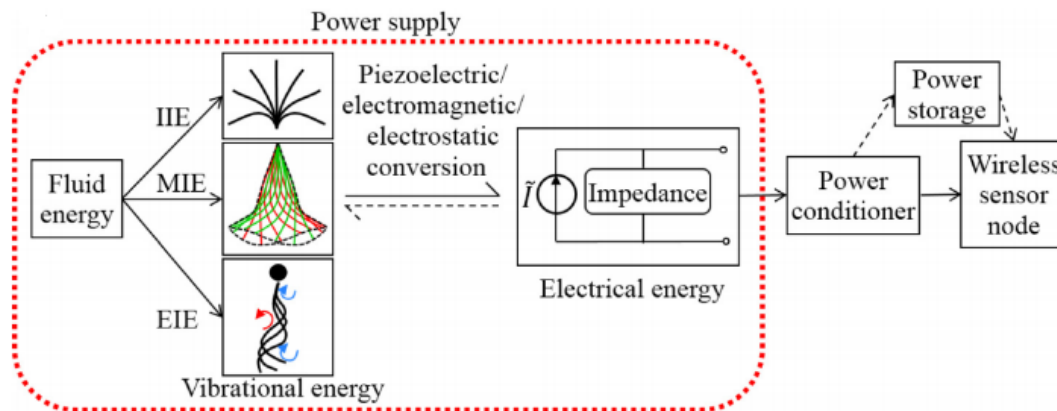
Figure 1.1: Applications of fluid-induced flag vibrations: energy harvesting, by [42]

in the picture will be described in section 1.3. Displacement-based solutions are much more efficient than deformation-based, but they introduce a high structural damping to the flag system, that is its oscillations have smaller amplitude and the final system is much more stable with respect to a normal flag. The importance of stability for energy harvesting will be described better in section 1.5.

1.1.2 Heat transfer enhancement

Convective heat transfer enhancement in channel flow is commonly required in cooling systems for electronics, heating and refrigeration engineering, and process industries in order to prevent thermal damage and ensure proper operation of systems.
Heat transfer enhancement using flags is a concept that involves employing passive heat transfer techniques, the flags consist in small protrusions or obstacles placed at an optimum distance from the surface of a heat exchanger or other heat transfer equipment. These flags disturb the boundary layer and induce turbulence, leading to increased heat transfer rates, a simple scheme is reported in figure 1.2.
The heat transfer performance evaluation criteria are the Nusselt[1] ratio at constant Re and the Nusselt ratio at constant pumping power. The Nusselt ratio at constant Re quantifies the increased heat flux due to flag vibration, which is defined as in equation 1.1, where Nu is the Nusselt number in the presence of vibrating flag, and the subscripts 0 and Re denote the parameter in plain channel at constant Re.

$$Nu_{Re} = \frac{Nu}{Nu_{0,Re}} \tag{1.1}$$

The pressure expenditure induced by the vibrating flag is taken into account in the Nusselt ratio at constant pumping power which is defined in expression 1.2 and where the subscripts 0 and p denote the parameter in plain channel at constant pumping power.

$$Nu_p = \frac{Nu}{Nu_{0,p}} \tag{1.2}$$

Research in this area has demonstrated that the presence of flags can substantially augment convective heat transfer. Studies, such as the work by Zhong et Al. [43], found that these structures can enhance the heat transfer efficiency by up to 100% compared to smooth surfaces. Another study by Chen et al. [5] investigated the effects of different tandem inverted flags configurations and reported that the local Nusselt ratio was higher behind the rear flag.

---

[1]The Nusselt number is the ratio of convective to conductive heat transfer across a boundary: $Nu = \frac{hL}{k}$, where h is the convective heat transfer coefficient of the flow, L is the characteristic length, and k is the thermal conductivity of the fluid
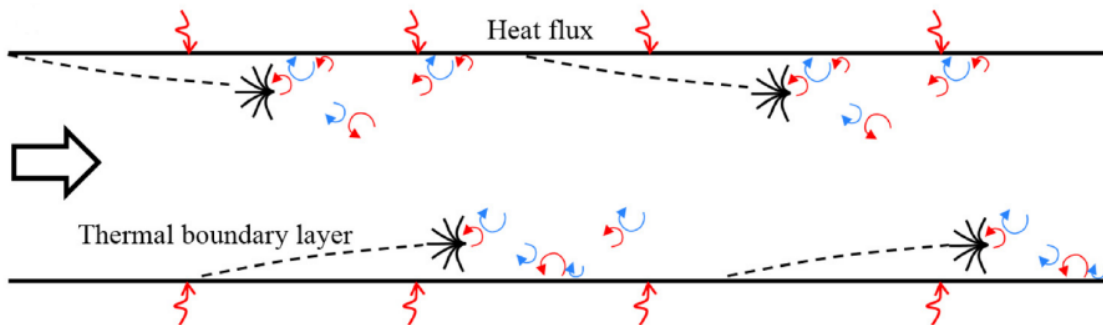
Figure 1.2: Applications of fluid-induced flag vibrations: heat transfer enhancement, by [42]

Researchers, like Suman et al. [38], have utilized numerical simulations and experimental techniques to gain a deeper understanding of the fluid dynamics and heat transfer phenomena associated with classic flag geometries as well.

It is worth noting that the effectiveness of flags as a heat transfer enhancement technique depends on various factors, such as flag geometry, flag configuration, flow velocity, fluid properties, and surface characteristics. Moreover, the optimal flag configuration may vary for different applications, and further research is continuously being conducted to explore new designs and applications of this technique. Overall, the use of inverted flags as a passive heat transfer enhancement strategy shows promising results, with the potential to improve the thermal efficiency and performance of heat exchangers and other heat transfer equipment in various engineering applications.

1.1.3 Multi phase flows mixing enhancement

In recent years, researchers and engineers have been exploring innovative methods to improve the mixing efficiency of complex fluid systems, especially when dealing with multiple flows or multi-phase flows. One intriguing approach gaining significant attention is the utilization of inverted flags, which has proven to be a promising solution. Fluid induced flag vibrations serve as passive agitators or passive stirrers in place of mechanically driven agitators, this means that they do not require external power sources and can be easily manufactured at low cost.
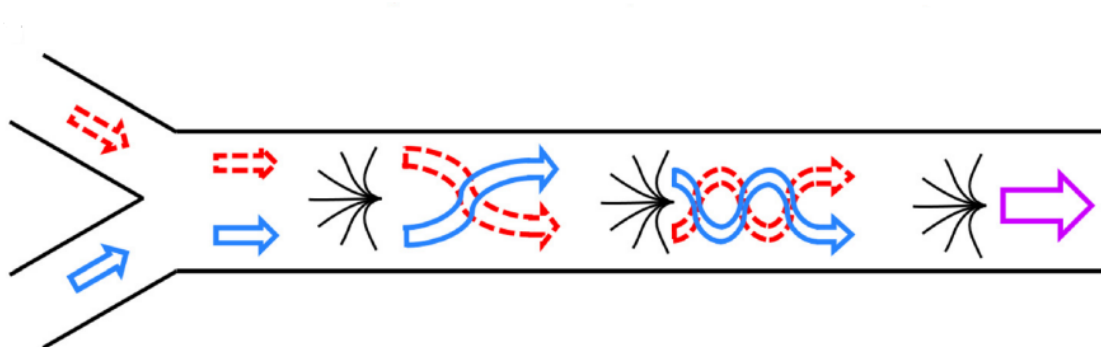
Figure 1.3: Applications of fluid-induced flag vibrations: mixing enhancement, by [42]

These inverted flags, strategically placed within the flow channels or vessels exhibit remarkable capabilities in manipulating fluid dynamics, a schematic example is depicted in figure 1.3. As the flows encounter the inverted flags, they induce controlled turbulence and generate intricate vortices. These turbulent structures facilitate the intimate interaction between different fluid streams or phases, leading to a substantial enhancement in the mixing process. The mixing efficiency can be quantified by the transport of a passive scalar through the channel, Ali et al. [1] show that the mixing efficiency can be improved of the 98% with respect to the rigid case, that is with no flexible passive membranes. Furthermore with this solution engineers can optimize

3

chemical reactions, and improve overall system performance, thus presenting exciting opportunities for a wide range of applications across various industries.

1.2 The application context

This investigation will focus on the energy harvesting aspect of the flags, specifically on how to accommodate a double flag configuration to improve its performance. Before moving into the details of the research, it is important to highlight to which specific case it will be useful to deploy this application. To this purpose a comparison with other technologies for renewable energy collection is helpful.
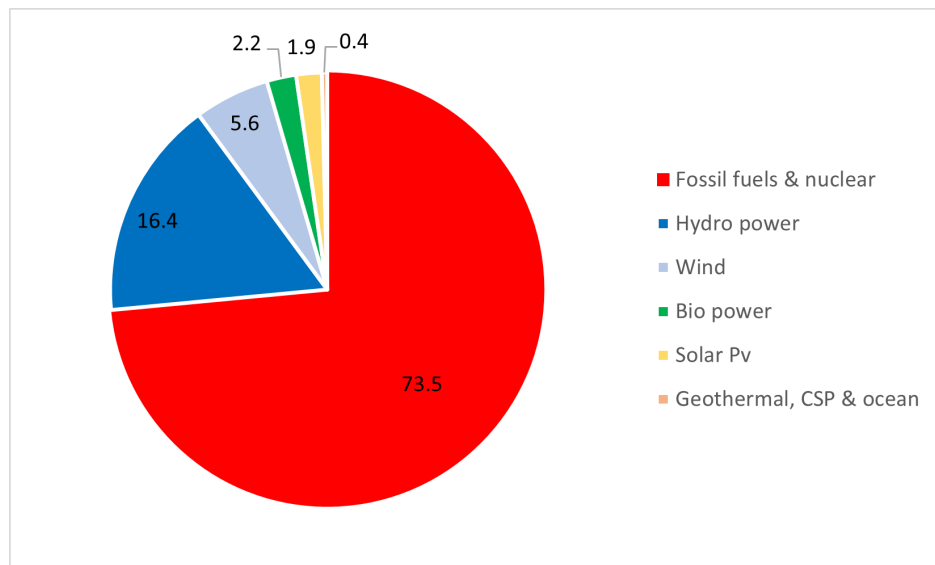

Figure 1.4: Global electricity sources estimation in 2017, see [29]

Graph 1.4 reports the global amount of electricity produced with different technologies, both renewable and not, in 2017. The overall percentage of the renewable electricity is 26.5%, and a consistent part of this energy is produced from hydroelectric sources (16.4%) and wind turbines (5.6%). Therefore it makes sense to compare the energy harvesting through piezoelectricity, which mainly serves low power applications like MEMS, with wind and hydro sources which are used to produce high power electricity, which can be delivered for industrial usage too.

1.2.1 Comparison: large-scale against small-scale energy production

Hydroelectric Harvesting
Application fields: hydroelectric power plants are commonly used to generate electricity on a large scale. Dams and reservoirs are constructed to harness the potential energy of water, converting it into kinetic energy through turbines, and then into electrical energy.
Grid stabilization: hydro power provides grid stability due to its ability to respond quickly to changes in electricity demand, making it valuable for maintaining a consistent power supply.
Base load power: hydro power can serve as a base load power source, providing a continuous supply of electricity due to its predictability.
Average electric power production: the average electric power production from a hydroelectric power plant varies significantly based on the size of the facility. Large-scale hydro power plants can generate hundreds of MW to several GW of power, while smaller run-of-river installations may produce a few MW.

Wind Harvesting
Application fields: wind turbines are commonly installed in onshore wind farms or

offshore wind parks to capture wind energy and convert it into electricity.

Distributed generation: small wind turbines can be used for distributed generation in remote areas or individual properties, supplementing the electricity supply.

Grid integration: wind power is integrated into the electricity grid to meet the increasing demand for renewable energy and reduce greenhouse gas emissions.

Average electric power production: the average electric power production from a wind turbine depends on factors like wind speed, turbine size, and efficiency. Onshore wind farms typically have capacities ranging from a few MW to hundreds of MW per facility. Offshore wind farms can reach GW-scale capacity.

Piezoelectric harvesting

Application fields: piezoelectric materials can be integrated into wearable devices to scavenge energy from human movement or into small devices for harvesting energy from mechanical vibrations induced by the environment, extending battery life or powering low-power electronics.

Structural health monitoring: piezoelectric sensors can be used to monitor structural integrity by converting mechanical stress or vibrations into electrical energy for wireless sensing systems.

Internet of Things (IoT) devices: piezoelectric harvesting is suitable for powering low-energy IoT devices where replacing batteries may not be feasible.

Average electric power production: the average electric power production from piezoelectric harvesting is relatively low compared to hydro and wind. It depends on the size of the piezoelectric element, the frequency and intensity of vibrations, and the application. Typically, piezoelectric harvesters produce mW to a few W of electrical power.

1.2.2 Prospective application of the research

In summary, hydroelectric and wind harvesting are major contributors to large-scale renewable energy production, with hydro serving as a reliable base load power source and wind providing grid integration and distributed generation. On the other hand, piezoelectric harvesting is suitable for low-power applications, particularly in wearable electronics, structural health monitoring, and IoT devices. While hydro and wind technologies can generate significant amounts of electricity, piezoelectric harvesting is more limited in power output but offers unique opportunities for self-powered small-scale devices and systems.

Obviously the purpose of this research is not focused on wearable applications, instead it is about fluid kinetic energy harvesting to supply remote sensors and micro electro-mechanical systems, possibly also low power actuators. By looking back at hydro and wind harvesting, the hydroelectric source is certainly more consistent in time because the water flow intensity changes much less frequently with respect to the wind, in fact the water flow is not likely to change its direction, unless some natural phenomena as mudslides or earthquake modify the water course. For this reason multiple inverted flags systems are most effective in naturally occurring water flows or channel flows (air, water or exhaust gas) within industrial piping, where the flow keeps its direction constant, at least at a local level. When there is few space a choice between one big flag or two or more smaller flags depending on the blockage[2] effect on the fluid flow and on the amount of required power for the users has to be made. Smaller flags can produce more power with less blockage if placed in the right fashion. In fact the flags interact one with the others by means of the fluid, and this interaction can be constructive or destructive to the membranes' motion depending on their relative positioning.

---

[2]the blockage effect will be used as a design parameter for the experiment of the investigation and it will be presented later on, in section 2.2

1.3 Flag configurations

All problems related to flags' fluid structure interactions are described by the same equations, but different boundary conditions apply depending on the configuration.

1.3.1 Single flag configurations

The most known single flag arrangements are represented in figure 1.5, for the two of them the undisturbed velocity is the same in the horizontal direction with right to left verse, while only the flags' edge is used to represent the solid flags. Usually the 2D flag is represented as an overlap of different phases of its dynamics.
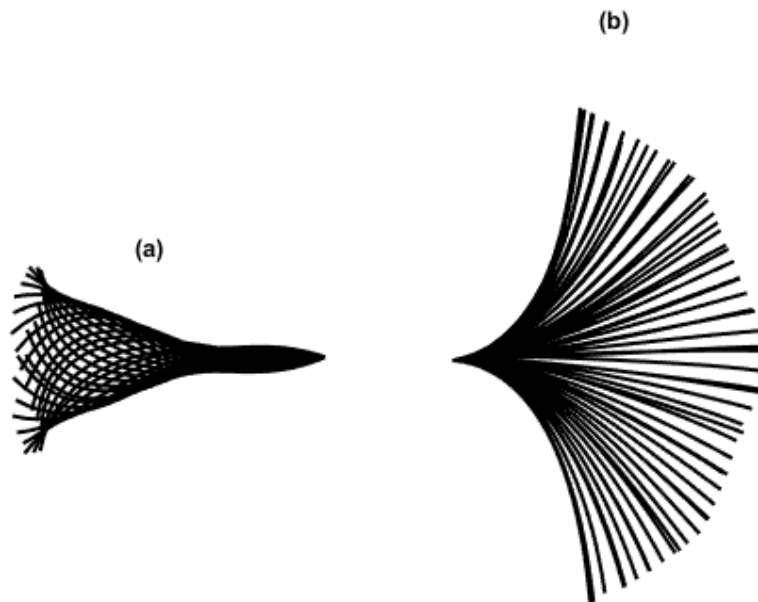
Figure 1.5: Single flag: configurations

Figure 1.5 (a) is the most common arrangement, the standard flag, basically it is a flagpole with the clamp at its leading edge, it is depicted in its flapping mode. The configuration of figure Figure 1.5 (b) is the inverted flag, as its name says, it is a reversed flag with the clamp at the trailing edge, this change in boundary conditions strongly modifies the flag flapping dynamics, as displayed in the picture, but also its stability. One more design, which is not reported in the picture, is the excited flag, usually it consists in a normal flag immersed in the wake of a bluff body, but an inverted flag can replace the normal one for some applications.

Instability classification The dynamics of the flag varies depending on the configuration, the vibrating behaviour has been classified into three main categories [27]: movement induced excitation (MIE), instability induced excitation (IIE) and extraneously induced excitation (EIE).
Each one of these elements applies to one of the previously mentioned configurations, specifically:
MIE - standard flag;
IIE - inverted flag;
EIE - excited flag.
The classification is based on the source of excitation which in the case of the EIE is simply the wake produced by the bluff body, while for the other two cases the excitation is due to instability of the configuration. The normal flag shows flutter instability, instead the inverted flag presents divergence instability.

6

1.3.2 Double flag configurations

Recently multiple flags configurations were investigated to understand if they had better performance with respect to the single flag in the different application fields previously explored. Basically to produce performance optimization it is necessary for the flags to interact constructively, so that the flapping amplitude increases over the one of the isolated flag. Multiple flags configurations are explored for inverted flags interaction mainly, therefore only double inverted flags systems will be presented in this section.

The two main arrangements reported in the literature are the tandem flags, figure 1.6 (a), in which two flags are aligned along the stream direction, and the parallel flags, figure 1.6 (b), where two flags are placed side by side. More configurations have been analyzed in the literature by combining together these two basic arrangements to obtain echelons of flags in different shapes with two or more flags, see for example the work of [9] and [16], but they are not a topic of discussion in this work.
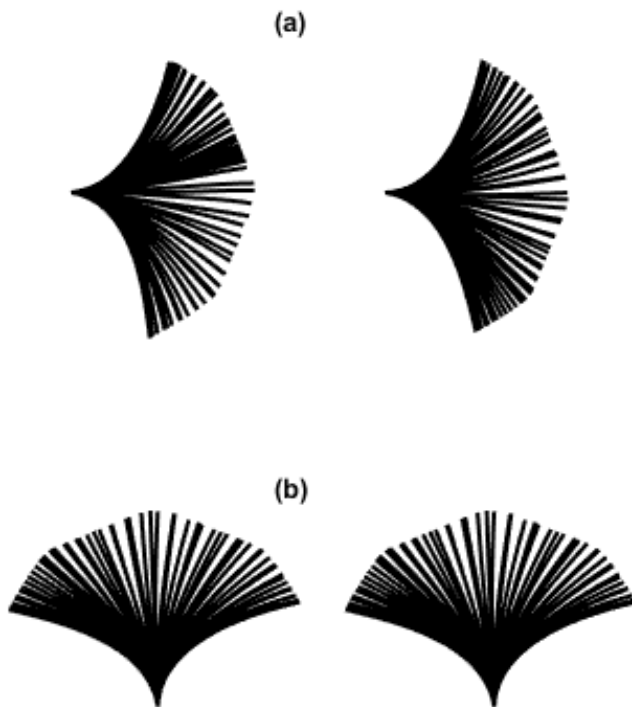

Figure 1.6: Double flag configurations

The fluid structure interaction of multiple bodies is much more complex with respect to the case of a single body because the number of parameters necessary to define the whole problem can be high, for this reason it is convenient to have flags with the same properties in terms of geometry and material.

The configurations depicted in figures 1.5 and 1.6 were obtained by post processing the data collected in this experiment.

1.3.3 Tandem echelon configuration

The focus of the thesis is the energy harvesting by the flag, in this case it is convenient to have highly unstable configurations to induce vibrations in the system also for external perturbations of low entity.

Particularly the aim of the project will be to assess if the energy capturing can be improved by moving the rear flag along the $\mathbf{x}$ and $\mathbf{z}$ directions of the reference frame in figure 1.7 where the upstream flow velocity is directed along $\mathbf{x}$ and the two flags are clamped along the orange stripes, moreover the flags are geometrically identical

7

and made of the same material. This possibility was inspired by birds formation flight during migrations [28], in this last case the phasing of the flapping between the front and rear birds is determining for the exploitation of upwash only and consequent drag reduction.
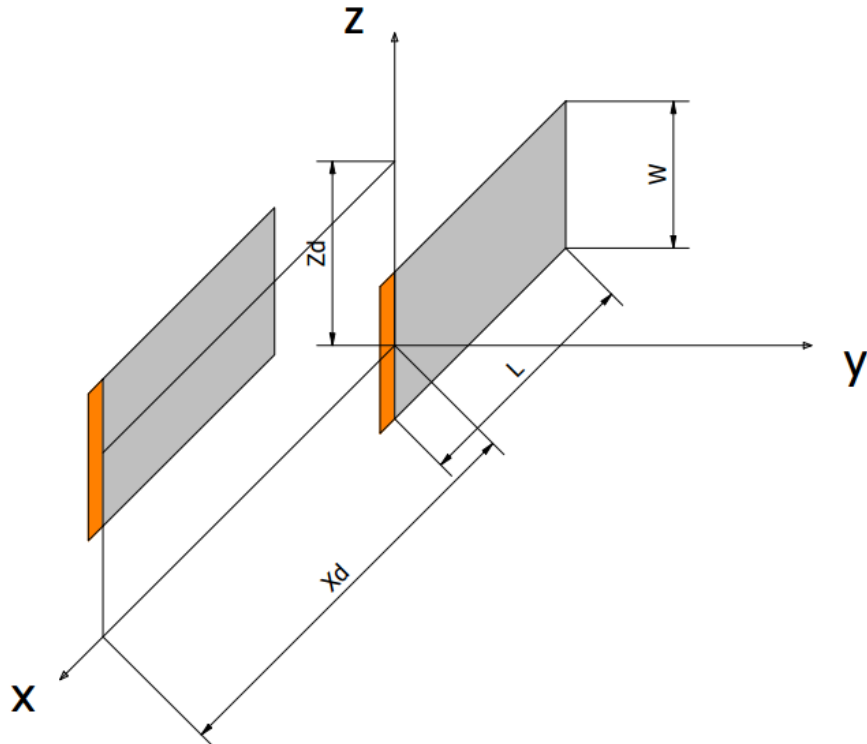
Figure 1.7: Novel configuration

Differently from birds' wings flapping, the flapping of the inverted flag occurs because of instabilities growth and it is not possible to control its frequency and amplitude without modifying the upstream flow velocity, for this reason the phase between the two flag is not controllable and emerges passively depending on their relative position in space [30]. The overall performance of coupled flags has always been found to be lower than an equal number of isolated flags due to the natural destructive vortex merging which takes place in classic configurations. Only in one case, which is reported in the numerical simulation by [16], the overall performance of the coupled configuration turned out to have higher efficiency than the isolated case, that is when a periodic staggered arrangement is deployed. To look for new arrangements where constructive vortex merging could potentially occur, the configuration shown in figure 1.7 will be investigated.

1.4 Dimensional analysis

In this section the parameters which describe the phenomenon will be pointed out, as previously mentioned it is important to keep the number of degrees of freedom as low as possible to simplify the experiment, in this way it will be easier to obtain a complete dataset since the number of arrangements to analyze will be reduced. A dimensional analysis turns out to be very useful in this case.

The analysis is based on the Buckingham theorem and it will make it possible to extract the non dimensional Π-groups which describe the problem. As can be observed in figure 1.7, basically there are $n = 9$ parameters which need to be defined:

$$\{W, L, \rho_s h, B, x_D, z_D, U_0, \rho_f, \nu_f\}$$

where

$$B = \frac{Eh^3}{12(1 - \nu^2)} \tag{1.3}$$

is the bending stiffness defined for a thin body like a plate, while ρ_s and ρ_f are the densities of the solid and of the fluid respectively, h is the thickness of the two flags (the flags have identical geometries), finally ν_f is the kinematic viscosity of the fluid. Usually the term $\rho_s h$ is written in this way because h is usually very small compared to the other dimensional lengths, but it is essential to understand how important the weight of the flag relative to the fluid inertia is.

Mass, length and time, which are the $k = 3$ magnitudes necessary to define the dimensions of the previous parameters, will be addressed as M, L and T respectively. The Buckingham theorem states that equation 1.4 holds true if the phenomenon is physically consistent.

$$[W^{\alpha_1} L^{\alpha_2} (\rho_s h)^{\alpha_3} B^{\alpha_4} x_D^{\alpha_5} z_D^{\alpha_6} U_0^{\alpha_7} \rho_f^{\alpha_8} \nu_f^{\alpha_9}] = 0 \tag{1.4}$$

To obtain the $n - k = 9 - 3 = 6$ Π-groups, first substitute in 1.4 the dimensions of each term as follows:

$$\begin{array}{lllll} [W] = L & [L] = L & [\rho_s h] = ML^{-2} & [B] = ML^2 T^{-2} & [x_D] = L \\ [z_D] = L & [U_0] = LT^{-1} & [\rho_f] = ML^{-3} & [\nu_f] = L^2 T^{-1} \end{array} \tag{1.5}$$

then, by collecting the three magnitudes, equation 1.6 is obtained.

$$L^{(\alpha_1 + \alpha_2 - 2\alpha_3 + 2\alpha_4 + \alpha_5 + \alpha_6 + \alpha_7 - 3\alpha_8 + 2\alpha_9)} M^{(\alpha_3 + \alpha_4 + \alpha_8)} T^{(-2\alpha_4 - \alpha_7 - \alpha_9)} = 0 \tag{1.6}$$

For equation 1.6 to be true, each exponent must be zero, the system of equations 1.7 is obtained.

$$\begin{cases} \alpha_1 + \alpha_2 - 2\alpha_3 + 2\alpha_4 + \alpha_5 + \alpha_6 + \alpha_7 - 3\alpha_8 + 2\alpha_9 = 0 \\ \alpha_3 + \alpha_4 + \alpha_8 = 0 \\ -2\alpha_4 - \alpha_7 - \alpha_9 = 0 \end{cases} \tag{1.7}$$

Since there are not enough equations to evaluate the exponents, it was chosen to rewrite α_2, α_4 and α_7 as functions of the remaining α_i. By substituting them in equation 1.4 and collecting the terms according to the exponents, it is finally possible to find the Π-groups:

$$\Pi_1 = \frac{W}{L}; \quad \Pi_2' = \frac{\rho_s h U_0^2 L^2}{B}; \quad \Pi_3 = \frac{x_D}{L}; \quad \Pi_4' = \frac{z_D}{L}; \quad \Pi_5' = \frac{\rho_f U_0^2 L^3}{B} \quad \Pi_6' = \frac{\nu_f}{U_o L}. \tag{1.8}$$

To have the same parameters as the literature for the 2D case, the groups Π_i' are changed as follow.

$$\begin{aligned} \Pi_2 &= \frac{\Pi_2'}{\Pi_5'} = \frac{\rho_s h}{\rho_f L} \\ \Pi_4 &= \frac{\Pi_4'}{\Pi_1} = \frac{z_D}{W} \\ \Pi_5 &= \frac{1}{\Pi_5'} \\ \Pi_6 &= \frac{1}{\Pi_6'} \end{aligned}$$

Now it is easy to recognize the same parameters from the literature along with the Reynolds number.

$$AR = \frac{W}{L} = \Pi_1$$
$$M_S = \frac{\rho_s h}{\rho_f L} = \Pi_2$$
$$K_B = \frac{B}{\rho_f U_0^2 L^3} = \Pi_5 \qquad (1.9)$$
$$Re = \frac{U_o L}{\nu_f} = \Pi_6$$

AR is the aspect ratio of the flag, M_S is called the mass ratio and it represents the weight of the flag with respect to the fluid, the higher the mass ratio the more important the inertia of the flag will become. K_B is called the non dimensional bending stiffness and compares the elastic restoring forces of the flag to the inertia of the fluid. The Reynolds number relates the importance of fluid inertia to its viscosity, for high Reynolds number the flow can be considered inviscid.
To reduce as much as possible the number of free Π-groups, only $\Pi_x = \Pi_3$ and $\Pi_z = \Pi_4$ will be varied, all the other parameters will be kept constant.

1.5 Literature review

Now, a brief review of the literature on the topic is presented, many aspects of the design of the experimental setup are reasonably explained through information from the literature.

1.5.1 Dynamics of the 2D inverted flag

The first study on the inverted flag was done by Kim et Al. [20], they highlighted its fundamental instabilities and the effect of different parameters on its dynamics.
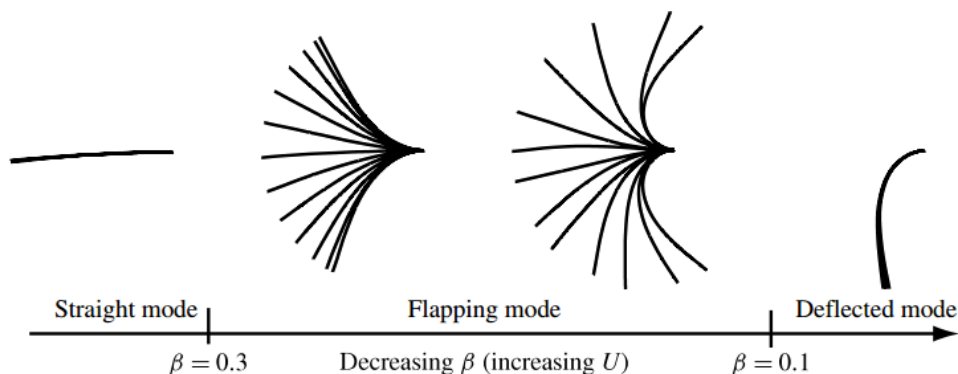

Figure 1.8: Fundamental modes of the inverted flag, by[20]

Figure 1.8 reports the overlap of multiple phases of the fundamental modes for a 2D inverted flag by varying the parameter $\beta = K_B = \frac{B}{\rho_f U_0^2 L^3} = \Pi_5$, defined in the dimensional analysis of section 1.4.
To obtain an experiment close to the 2D case it is necessary to increase the aspect ratio $AR = \frac{W}{L} = \Pi_1$ as much as possible, in this way the 3D effect induced by the side edge vortexes will be much less relevant.
It is important to notice the existence of three fundamental modes of the inverted flag in figure 1.8:

1. the straight mode;

2. the flapping mode;

3. the deflected mode.

In the straight mode the flag presents a quasi-steady state and has very low amplitude oscillations around the straight position. The flapping mode has different combinations of oscillation's frequency and amplitude depending on the value of β

when the other parameters are kept constant. The amplitude of the flapping motion is defined as in figure 1.9 and it is addressed with the letter A, basically it is the tip to tip displacement during the flapping and it is perpendicular to the incoming flow velocity. The red area in figure 1.9 is the total swept area by the flag for that particular flapping motion and it is equal to
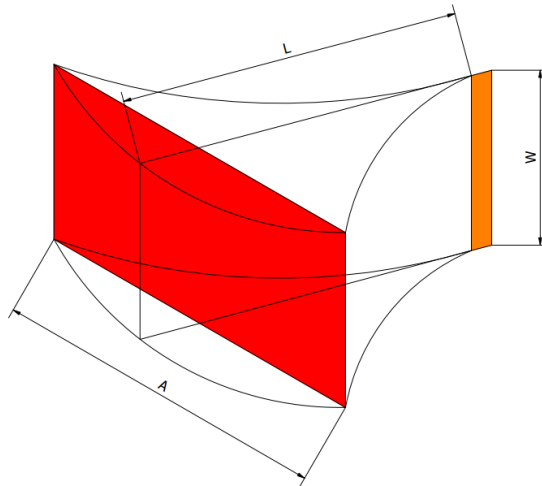
$$area = A \cdot W.$$

Figure 1.9: Swept area of a flapping flag

The deflected mode is another quasi steady regime in which the flag oscillates with very low amplitude around the deflected position.
The parameter K_B is the ratio of the bending stiffness of the flag over the inertia of the fluid, for this reason it makes sense that when it is too low the flag restoring forces cannot stand the inertia of the incoming fluid and the flag remains deflected.
In comparison to the inverted flag, the dynamics of a standard flag is quite different and it will be presented in the next section 1.5.2.

1.5.2   Stability map for the 2D case

Typically the highest energy conversion is obtained in the flapping mode. Figure 1.10 is taken from [42], it is the stability map which characterizes three different flag configurations: the classic flag (Movement Induced Excitation, MIE), the inverted flag (Instability Induced Excitation, IIE) and the classic flag behind a bluff body (External Induced Excitation, EIE). The association of the configurations with the type of source of the instability has been also introduced in section 1.3, while the parameters used for the stability analysis are reported in section 1.4.

The stability map shows areas where the perturbations on the different flags' configurations amplify with time. Measurements taken from different studies are also indicated on the map, for further insights see [42]. The dynamics of the inverted flag was discussed in the previous section, here it is possible to observe for which combinations (M_s, K_B) the different modes occur, specifically (b) is the flapping mode and it verifies independently on M_s and in the range $0.1 < K_B < 0.3$, (c) is the deflected mode and it happens everytime $K_B < 0.1$, (a) is the biased mode and it was not mentioned in the previous section, the reason is that the cause behind this mode is not clear, in fact it does not always occur and it could be related to other parameters which are not involved in the 2D case such as the aspect ratio and the initial angle of attack of the inverted flag, see for example [21]. Whenever $k_B > 0.4$ the inverted flag presents the straight mode, finally for very low values of K_B the inverted flag behaves like a classic flag (d) because it flips backward.

The stability map 1.10 is important also because it compares the three different configurations (IIE, EIE and MIE) in terms of instabilities. This means that it makes
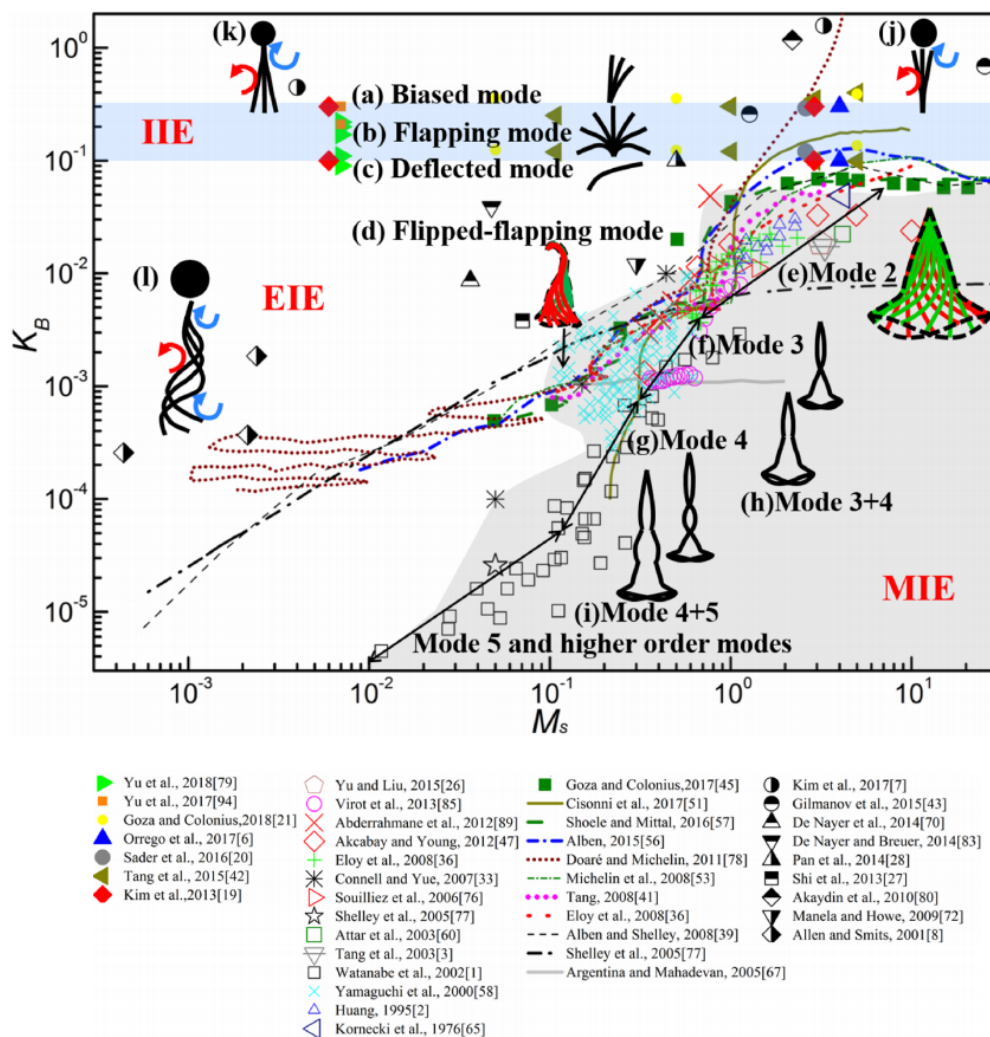
Figure 1.10: Stability map, by [42]

it easy to understand which arrangement is more unstable than the others, and this is an essential property to the purpose of energy harvesting. Before moving on with the comparison, it is useful to briefly describe the dynamics of the classic flag.

Similarly to the inverted flag, the classic flag has three fundamental modes:

1. the straight mode, the flag stays straight with very small oscillations;

2. the flapping mode, the flag flaps periodically and the oscillation mode changes depending on the non dimensional parameters;

3. the chaotic mode, the flag flutters with a wide spectrum of frequencies and the final vibration appears not to be periodic.

By looking at figure 1.10, the instability of the classic flag depends on both the mass ratio M_S and the non dimensional bending stiffness K_B, while the inverted flag's instability only depends on K_B. Moreover, the range of K_B in which the instabilities are triggered to grow up has much higher values for the inverted flag than the classic flag. This means that the inverted flag is unstable for lower fluid velocities than the standard flag in the 2D case if they are made of the same material and have the same thickness.

At the beginning of the section it was pointed out that for energy harvesting purposes the best operating condition is the flapping mode, then it turns out to be an advantage to have an highly unstable configuration.

These information is useful to plan the experiment, in fact it is possible to design the flag in such a way that K_B will fall in the desired range for the flapping mode to occur, this part will be presented in chapter 2. Figure 1.11 is also from [42], and it

plots the experimental data from literature and their fittings of the Strouhal number, defined in expression 1.10.

$$St_A = \frac{fA}{U} \tag{1.10}$$

The Strouhal number compares the timescale of the flapping mode to the timescale of the fluid flow, in this case it is defined with respect to the flapping amplitude, which is measured between the two extreme positions of the flapping (figure 1.9).
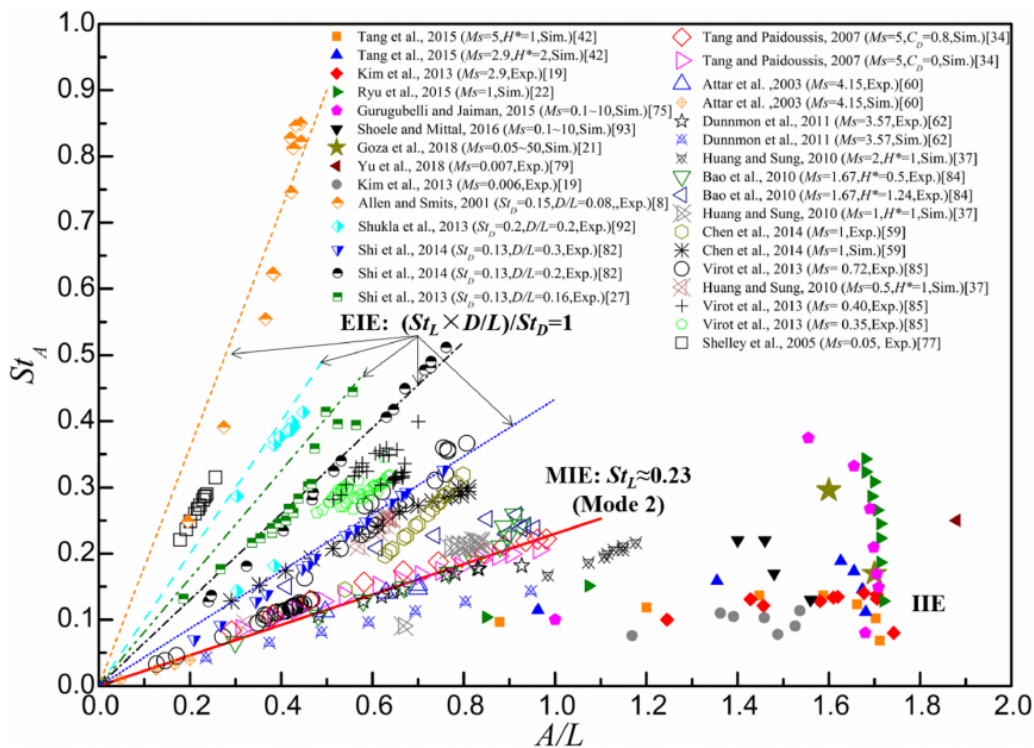

Figure 1.11: Strouhal number against flapping amplitude, by [42]

These two new parameters, which are the flapping frequency f and the flapping amplitude A, were not considered in the dimensional analysis in section 1.4 since they are a consequence of the dynamics and outputs of the problem. Anyway they are required to understand the frequency range of the phenomenon which will be studied, in order to avoid resonances between the flag and its support.

1.5.3 Hysteresis and 3D effects

Another interesting aspect about the flapping instability of the inverted flag is its hysteresis response, in other words by increasing the flow velocity the onset of the instability occurs later with respect to when it stops by reducing the flow velocity. To better observe this aspect the reduced flow velocity parameter is introduced:

$$U^* = \sqrt{\frac{1}{K_B}} = LU_0\sqrt{\frac{\rho_f L}{B}}.$$

Figure 1.12, which is taken from [24], summons well the hysteresis behaviour. Particularly, in figure 1.12a the sudden shifts of the amplitude represent the onset and dying of the flapping mode, it is interesting to point out that the gap between the upsweep speed and the downsweep speed increases as Reynolds number increases.
The upsweep velocity is the velocity value at which the flag mode changes from straight to flapping. Instead, the downsweep velocity is the velocity value at which the flag mode switches from flapping to straight.
A second important aspect to point out is that St_A increases as U^* decreases and that higher Strouhal numbers can be achieved during downsweep because of the hysteresis, as can be noticed from figure 1.12b. Figure 1.12c reports how the gap
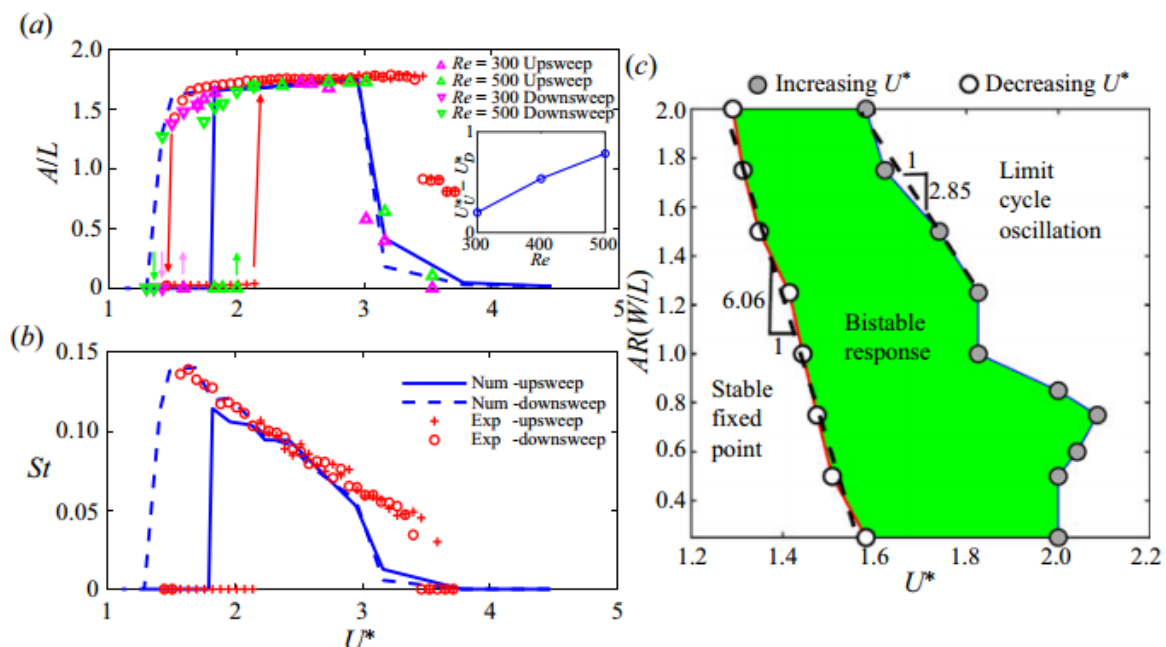
Figure 1.12: Inverted flag hysteresis response, by[24]

between the downsweep and upsweep velocities varies with the aspect ratio. The green region is defined as bistable response, in fact the coexistence of two states occurs within it, the straight and the flapping mode. This graph is extremely important when selecting the design aspect ratio of the flag, in fact the lower the aspect ratio the higher the upsweep velocity to obtain the flapping mode. More insights about this property are given by [35], from which figure 1.13 is taken. This last clearly depicts how dimnishing the aspect ratio causes first an inevitable reduction of the flapping regime range and then its complete absence when $AR < 0.2$. The stabilizing effect of the SEV is observable in the augmentation of the upsweep velocity when AR gets reduced, while it is not clear which phenomenon causes the transition from the flapping to the deflected mode to anticipate when AR shrinks.
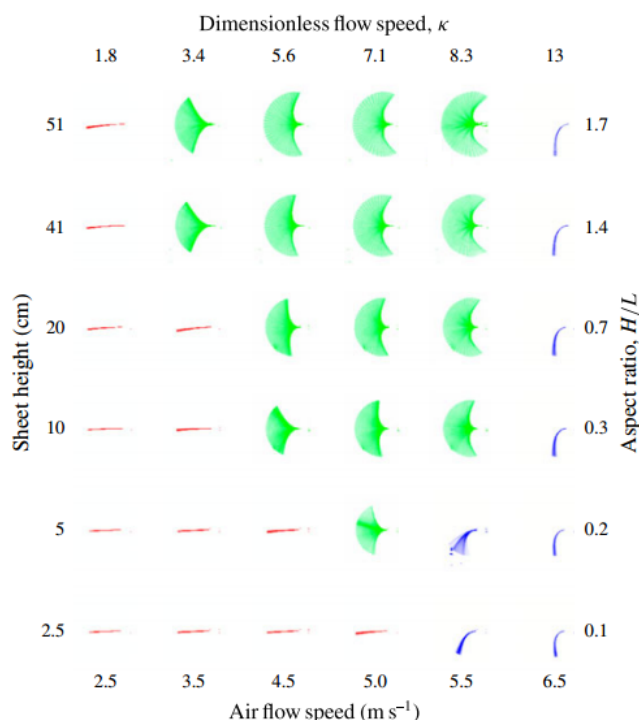

Figure 1.13: Effect of the aspect ratio on the instability of the inverted flag, by [35]

By using the vortex lattice method Sader et al. [35] were able to demonstrate that equation 1.11 is valid with low error for inverted flags of aspect ratio $\frac{W}{L} > 1$.

$$k_{lower} \simeq 1.85\left(1 + 2\frac{L}{W}\right) \tag{1.11}$$

In fact, the data collected and reported in figure 1.14 confirms that formula 1.11 is a good approximation of the upsweep condition when $AR > 1$. When the aspect ratio is lower than one, the formula is not precise because it does not take into account the 3D effects of SEV, which are not negligible anymore.
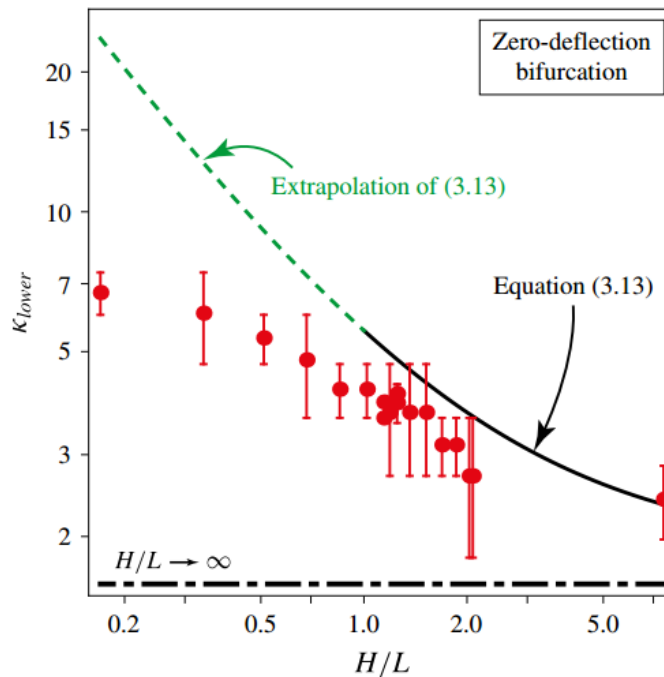

Figure 1.14: Data and theoretical formulation by [35]

The hysteresis has been observed to happen for the flapping to deflected mode transition as well, but the span of non dimensional velocities is much narrower with respect to the first transition. For this reason, when speaking of upsweep and downsweep velocities, the transition from straight mode to flapping mode is implicitly addressed.

As already mentioned side edge effects are stabilizing to the flapping dynamics since they are another means, other than the LEV (leading edge vortex) and TED (trailing edge vortex), to bring fluid mass from one side of the flag to the other. By placing the flag close to a wall with a gap between the flag and wall, which will be addressed as G, such that

$$\frac{G}{L} < O(10^{-4}) \tag{1.12}$$

then the wall will damp the side vortexes [8] and something very close to the 2D case is obtained. Side edge effects, gravity and manufacturing imperfections of the material are responsible for 3D deformations of the flag, these are much important for low K_B but they do vanish for high K_B. Then the best way to operate the experiment is to set K_B high enough in order to have mainly 2D modes, but also it must be $K_B < 0.3$ to trigger the flapping mode.

So far side edge vortexes have been visualized through numerical simulations only, the numerical models have been proved to be valid by comparing their results with experimental observations in term of forces and displacements.

Figures 1.15 and 1.16 depicts the result of a numerical simulation for two values of the aspect ratio, respectively 0.5 and 1. It can be noticed how in the first case the interaction between the SEV and the LEV is higher with respect to the second case. The exploitation of SEV seems to be controversial since their overall intensity increases when AR gets lower, but at the same time the K_B range for the flapping mode gets smaller. This means that the higher the contribute of the SEV, the lower
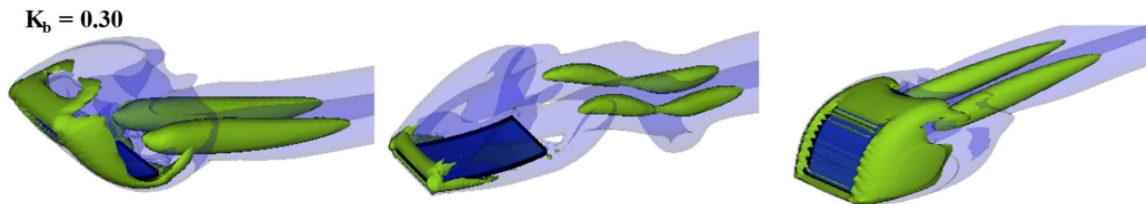
Figure 1.15: Side edge vortexes from simulation by [23], $AR = 0.5$
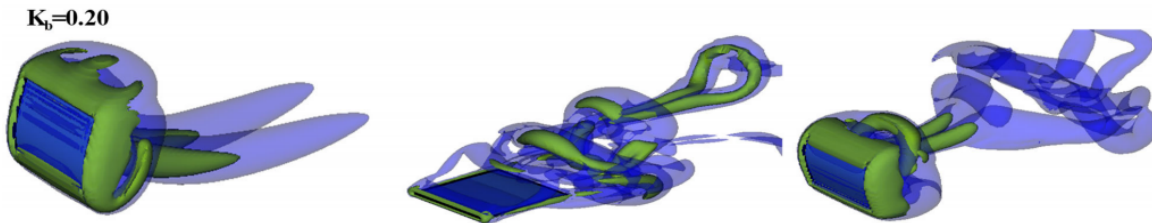
Figure 1.16: Side edge vortexes from simulation by [23], $AR = 1$

the operability of the device in the flapping regime. Nonetheless, this does not exclude that the harvesting ability of the flag can still benefit from the SEV, even for high AR. A 3D visualization of the FSI of the inverted flag can also confirm or deny the vortex lift for this arrangement, which is the phenomenon for which in [35] they justify the difference between the experiments and the prediction of equation 1.11 in figure 1.14.

1.5.4 Formation flight

Formation flight can help to better understand the dynamics of multiple oscillating bodies. Specifically, in the case of multiple flapping sheets it is possible to refer to birds' formation flight. One of the main topics in this field was to look for which reason formation flight emerged in large birds' migrations. [2] reports a summary of the main hypotheses why birds fly in formation lines or clusters depending on their species, and it is pointed out that to completely understand this phenomenon a multidisciplinary study should be carried out, this means that the reasons behind this behaviour can be related to different aspects, from drag reduction to awareness of the whole fleet to possible dangers.

During the latest years more precise simulations were performed, [11] simulated a V-formation flight of flapping wings with an unsteady vortex lattice method an found out that the line formation was actually a benefit to drag reduction and efficiency enhancement, and it also points out how increasing the number of elements in the formation optimizes the efficiency.

Along with numerical simulations, also experiments became smarter and more precise, [28] used a trained flock of migrating ibises to track their respective positions and vertical acceleration during a formation flight and they found out an effective exploitation of upwash with downwash avoidance by phasing flapping.

A similar pattern arises in [30] where the autors try to prove the Lighthill conjecture, which posits that arrangements may emerge passively from hydro or aerodynamic interactions, drawing an analogy to the formation of crystals by intermolecular forces. The experiment shows that stable states exists in the distancing of two tandem iso-frequency flapping wings, this allows the rear wing to follow the leading wing with minimal energy consumption, similarly birds adjust wing flapping phase difference with respect to the preceding bird depending on their relative distance to reduce the total drag.

All of the preceding works asses that that large birds formation flight has not the only purpose of making each birds of the flock aware of the other elements of the fleet or having clearance in front of them or improving communication among them but also it gives them aerodynamics benefits. To draw an analogy with flapping flags, a rear actively flapping wing gets induced drag reduction and improved performance from the

wake of a frontal actively flapping wing in the same way as a rear passively flapping flag gets pressure drag augmentation and higher elastic energy conversion from the wake of a frontal passively flapping flag. Obviously this thesis needs to be acknowledged, this is the final task of the experiment of this project.

Chapter 2

Preliminary analysis

In this chapter the preliminary study of feasibility of the experiment is presented along with the description of the facility which will be hosting it. The information presented in the previous chapters is essential for this first part.

2.1 Facilities

Based on what emerged from chapter 1 the most efficient dynamic mode of the inverted flag to the purpose of energy harvesting is the flapping mode. Therefore, the first task is to guarantee that an isolated inverted flag[1] can flap with a stable limit cycle in the prescribed experimental conditions. In section 3.3.3 it will be pointed out the difference in terms of dynamic flapping for geometrically identical samples, with the only difference that they are cut from different sheets of the same material. This is meant to anticipate that the actual dynamic of the flag will likely be different from what expected and prescribed in here.

In Auburn University there are two facilities where the experiment can be performed, the wind tunnel and the water tunnel, the facility is required to produce a uniform and steady fluid flow and to be equipped with a moving traverse system for the experiment to be successful.

Figure 2.1: The wind tunnel

Figure 2.1 depicts the wind tunnel, it is an open loop facility whose velocity in the test section can be varied between 0 and 193 km/h = 120 mph = 53.61 m/s. The cross section area of the test section is 61cmx61cm (2ftx2ft). The main fan can be controlled manually or through computer by modifying the voltage on the interface panel. The relation between the control voltage and the frequency of the fan is linear. The architecture is typical of an open loop wind tunnel: an inlet with a net is placed right before the tranquillization chamber, a convergent accelerates the air to the beginning of the test section and a series of grids make sure the final velocity is aligned with the axis of the test section, this last is provided with different lids for probes or sensors mounting plus a traverse system at its top. The test section ends up in a divergent

---

[1]Isolated means there is no other body immersed in the flow which can cause any interactions

where the fan is placed, therefore this is a suction open loop wind tunnel.

Figure 2.2: The water tunnel

The interface is similar to the wind tunnel for controlling the water speed in the water tunnel, but the control parameter is the spin frequency of the engine in this case. The water tunnel is a closed loop facility, its architecture presents a main engine which drives a pump placed below the tranquilization chamber. The tranquilization chamber leads to a convergent which ends in the test section. This last has a 45cmx45cm wide test section and the water can reach the maximum speed of 1.2 m/s in this spot, furthermore the turbulence intensity is 1% at 3 ft/s. The test sections of both the wind tunnel and the water tunnel are divergent to account for boundary layer expansion. At the end of the test section a recirculation chamber drives the water back to the lower part of the tunnel and back to the pump. The pipe at the bottom is connected to the drain line and to the water supply line through a three arms valve. Observing figure 2.2 the water flow direction in the upper part of the facility is from the tranquilization chamber, in the deepest part of the image, to the recirculating chamber in the very foreground of the picture.

2.2 Feasibility analysis and flag design

In section 1.5.2 the stability map of the inverted flag in the space of parameters K_B and M_s has been described and analysed. Since it is essential for the flag to flap to achieve the highest efficiency, the first step in the design is to guarantee the following condition, see again figure 1.10:

$$0.1 < K_B < 0.3 \tag{2.1}$$

and by looking at the definition of the parameter in section 1.4, it is clear that there are different variables which need to be set, they are:

1. flag material;

2. flag geometry;

3. fluid density (air or water);

4. flow speed.

First the flag dimensions are chosen by taking into account the cross section area of the facilities. It is essential to have negligible blockage effect during the experiment not to pollute the measurements. For this to happen the blockage ratio needs to be less than 10% as found in [6], where the blockage ratio is defined as in expression 2.2.

$$BR = \frac{A_{blocked}}{A_{available}} \tag{2.2}$$

19

$A_{available}$ is the cross section area of the test section while $A_{blocked}$ is the area obtained by projecting the body on the cross section plane of the test section. Since the experiment investigates the fluid structure interaction of two inverted flags, the worst case scenario for the blockage effect is considered, that is when the projected areas of the two flags do not overlap, moreover the ideally maximum swept area is considered for each flag, as a reminder consider figure 1.9 and set the amplitude $A = 2L$. It follows that

$$A_{blocked} = 2(2LW) \tag{2.3}$$

this form (eq. 2.3) is used to be more conservative in the design.

	Water tunnel	Wind tunnel
10% Cross section limit (m^2)	0.02025	0.03716

Table 2.1: Maximum values of $A_{blocked}$ in the two facilities

Table 2.1 shows the limits on the flag dimensions in terms of blockage area. The next step is to choose the flag aspect ratio, or the non dimensional group Π_1, see definitions 1.9. In chapter 1 the effect of the aspect ratio on the inverted flag instability was highlighted, the main aspects which emerge are the influence of the side edge vortexes on the K_B range in which the flapping mode occurs and the presence of vortex lift for slender flags (low aspect ratio), see [35] and [34]. Since in the experiment the rear flag will be displaced both in the streamwise direction and in the vertical direction with respect to the front flag and since there is an interest to study the effect of SEVs interactions, a slender flag is chosen, in terms of aspect ratio this turns into condition 2.4.

$$0 < AR \leq 0.5 \tag{2.4}$$

In the available range of values for the aspect ratio it was chosen to take the highest value since it is a good trade off between the SEVs' intensity, overall dimensions of the flag for eventual flow visualization and volume occupied in the vertical direction. When setting an experiment, the effect of the walls must always be considered, it is good practice to keep the phenomena which will be observed as far as possible from the walls to avoid interference.

$$\Pi_1 = AR = 0.5 \tag{2.5}$$

Therefore the value in expression 2.5 was chosen for the AR.

In graph of figure 2.3 the red and green limits are the ones listed in table 2.1, while the blue line is obtained from equation 2.3 by changing $W = AR \cdot L$ to obtain $A_{blocked} = 4 \cdot AR \cdot L^2$. The length was chosen in such a way that both the limits were respected (table 2.2).

L	W
7.62 cm = 3 in	3.81 cm = 1.5 in

Table 2.2: Design dimensions

The next phase is to choose the thickness of the flag and its material along with the fluid nature and its velocity. To this purpose it is possible to build a feasibility table, that is a table which collects the available materials and the resulting velocity limits depending on the type of fluid and flag material once the thickness is set.

The thickness was chosen based on the standard dimensions of the plastic sheets produced by the manufacturers. Two values of the thickness were selected, see expression 2.6.

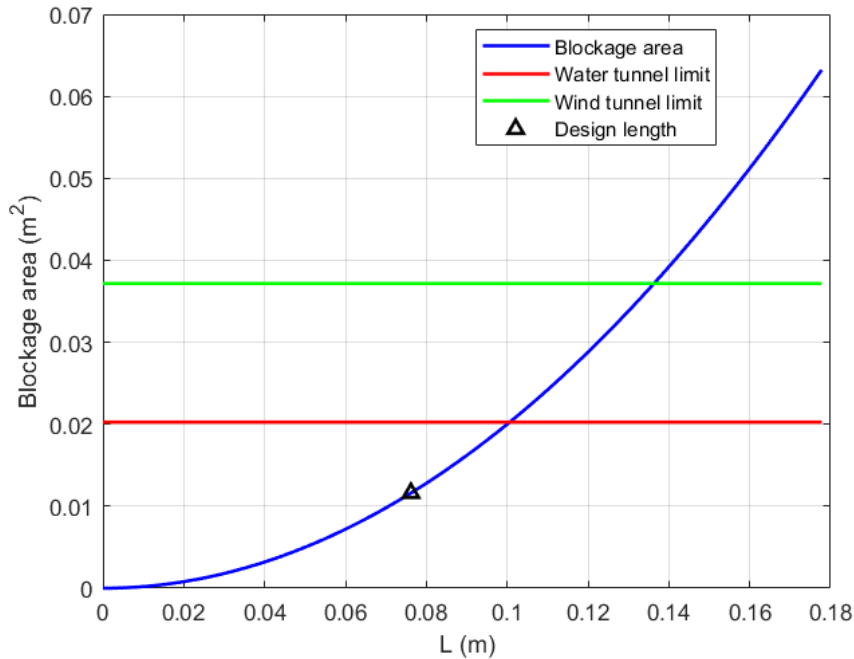$$\begin{aligned} h_1 &= 254\,\mu m = 0.01\,in \\ h_2 &= 274\,\mu m = 0.011\,in \end{aligned} \tag{2.6}$$

Figure 2.3: Flag design length

Material	E [Pa]	ρ [kg/m^3]	Poisson ratio	B [Nm]
steel	2.07E+11	7800	0.28	0.307
aluminum	6.90E+10	2700	0.32	0.105
mylar (PET)	5.00E+09	1380	0.35	0.0078
brass	1.10E+11	8730	0.331	0.169
PVDF	1.20E+09	1780	0.32	0.00183
silver	7.60E+10	10490	0.384	0.122

Table 2.3: Materials' properties

Material	U_{crit}^{min} [m/s]	U_{crit}^{max} [m/s]	Ms
steel	1.75	3.04	0.0286
aluminum	1.03	1.78	0.00990
mylar (PET)	0.279	0.484	0.0051
brass	1.30	2.25	0.0320
PVDF	0.135	0.234	0.00650
silver	1.10	1.91	0.0385

Table 2.4: Flapping mode velocity span in water

Material	U_{crit}^{min} [m/s]	U_{crit}^{max} [m/s]	Ms
steel	50.1	86.8	23.3
aluminum	29.3	50.8	8.08
mylar (PET)	7.98	13.8	4.13
brass	37.2	64.4	26.1
PVDF	3.87	6.70	5.33
silver	31.6	54.7	31.4

Table 2.5: Flapping mode velocity span in air

Tables 2.4 and 2.5 report the value of the transition velocities U_1 and U_2 respectively from the straight to the flapping mode and from the flapping mode to the deflected mode for inverted flags of thickness h_1. Thickness h_2 was selected because some plastic sheets of that thickness were available and used in the preliminary experiment, see also section 3.2.
Table 2.3 contains the main properties of the different materials along with the bending stiffness, which is calculated as in 1.3. The velocities U_1 and U_2 are computed through

the definition of $\Pi_5 = K_B$ in the array of expressions 1.9, by inverting the formula equation 2.7 is obtained.

$$U_i = \sqrt{\frac{B}{\rho_f K_{Bi} L^3}} \tag{2.7}$$

The values $K_{B1} = 0.3$ and $K_{B2} = 0.1$ can be set by reference to section 1.5.2. The final step in the preliminary design is to decide which fluid to use for the experiments and the final undisturbed velocity. A comparison of the two cases is briefly reported to highlight why it was decided to do the experiments in water. First it is possible to notice a substantial difference for M_S in the two cases, but as it has been stated in section 1.5.2 the mass ratio does not affect the growth of the instabilities for the inverted flags, therefore the dynamics will be the same within the interval $U_1 < U < U_2$ in both the cases, that is a flapping mode will be observed. The second aspect to consider is the order of magnitude of the velocities, in air everything happens faster with respect to water, this means that it will be much more difficult to observe clearly how the structure and the fluid flow interact.

It is possible to get an estimation of the flapping frequency for a mylar inverted flag with the dimensions previously specified. Consider the conditions in table 2.6.

A/L	1.6
St_A	0.36
M_S	4.13
U m/s	10.8

Table 2.6: Data for flapping frequency estimation in air

The parameters A/L and St_A were obtained from the results by [14] which are presented in figure 1.11, while M_S and U were chosen from table 2.5. From the definition of the Strouhal number (see expression 1.10) the following can be written:

$$f = \frac{St_A U}{A} = 31.9 \, Hz. \tag{2.8}$$

By doing the same for the case of an identical inverted flag immersed in a uniform water flow, the following quantities can be used to get an estimation of the flapping frequency.

A/L	1.4
St_A	0.11
M_S	0.005
U m/s	0.38

Table 2.7: Data for flapping frequency estimation in water

The parameters A/L and St_A were obtained from the results by [20] reported in figure 1.11. Again M_S and U were taken by table 2.4.

$$f = \frac{St_A U}{A} = 0.391 \, Hz. \tag{2.9}$$

By comparing the two values of the flapping frequencies in 2.8 and 2.9 for the same flag, it is easy to understand why it is preferable to do the experiment in water. In this way the fluid structure interaction will be the same with respect to air but the phenomenon will occur slowly and will be easier to observe.

Once the facility to host the experiment has been chosen, which is the water tunnel, the last parameter to set for the preliminary design is the upstream flow velocity. It will be pointed out later in this document how the choice of this parameter is not such an easy task. For now it is possible to take the mean value of the flapping interval extrema in table 2.4 for the mylar sheet, but the possibility to use piezoelectric materials like PVDF is not excluded yet. In any cases, the velocities for mylar and PVDF are both

achievable in the water tunnel (remember the maximum velocity is about 1.2 m/s in the test section).

In the next section it will be discussed how to compare the different inverted flags' arrangements in terms of efficiency or potential of energy extraction. Two main approaches can be used for this purpose, the feasibility and technical challenges for both of the approaches will be discussed to compare them and finally choose which method would be more convenient. In this perspective the adjective convenient means which way can be pursued and completed with the available time. First the magnitudes of interest will be highlighted for each one of the two methods, then the method for measuring them and realizing the experiment will be exposed, finally there will be the comparison of the two methods.

2.3 Methods

The first method consists in using a piezoelectric device, in fact if the flag is made of piezoelectric material, it will produce an oscillating electric power when it is in the flapping state. The output power can be measured by means of an ad hoc external circuit to the device. The incoming power to the inverted flag can be estimated as the flow kinetic power over the ideally maximum area swept by the flapping flag which is equivalent to half of the area in expression 2.3, in other words it is the ideally maximum blockage area of a single flag. The ratio of the output power from the piezoelectric device over the input power from the fluid flow is the efficiency of the single flag by definition.

The second option consists in measuring the potential of the flag with respect to energy capturing instead of the actual efficiency of the process. This approach is justified by the energy conversion chain (diagram 2.4).
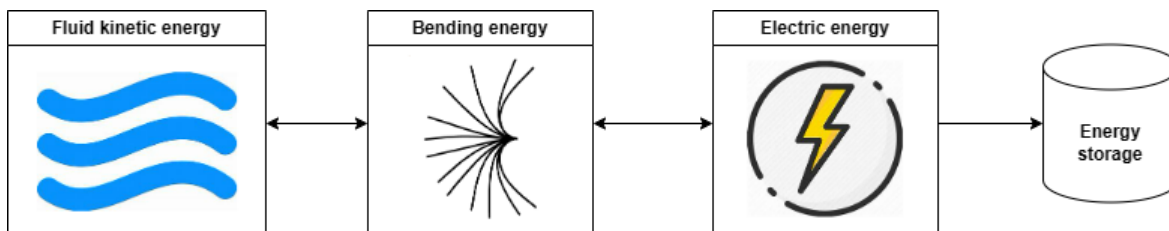

Figure 2.4: Energy conversion chain

The double arrows in the diagram of figure 2.4 mean that there is a bidirectional and dynamic energy exchange, in fact the inverted flags give back all the energy to the fluid flow in the form of vortexes if there is not any technologies to assist the conversion of the bending energy, moreover the first conversion (from fluid kinetic energy to bending energy) can be considered conservative because the effect of viscosity is very low since the Reynolds numbers in the flapping mode are high usually. The conversion between the bending energy and the electric one is bidirectional because of the direct and converse effect of the piezoelectric device but it is not conservative because of the eventuality of parasite currents and other dissipative effects.

Anyway the main purpose of this diagram is to assess that the higher the bending energy stored in the flag the higher will be the possibility to obtain higher electric energy, and by consequence higher efficiency. Therefore in this second method possibility of efficiency improvement will be used as comparison parameter among the different arrangements instead of efficiency itself.

2.3.1 Method 1

Piezoelectricity

Piezoelectricity is the capability of the material to produce an electric potential when it undergoes deformation, this is called direct effect. At the same time, applying an electric field to the material generates stresses and consequently strains, this last is called the converse effect.

Piezoelectricity can only be observed in dielectric materials, moreover the material is required to be anisotropic, which means that its physical properties do depend on the direction along which they are measured. This is due to the crystal molecular structure of piezoelectric materials, the organized arrangements of molecules make it possible the formation of small and uniformly oriented dipoles when the material goes under deformation. By consequence also the electrical properties of the material will be a function of the direction along which they are measured. In fact both the elastic compliance and dielectric permittivity of a piezoelectric material are described by two tensors. One more and last condition for piezoelectricity to occur is that the molecular structure of the material must not possess a center of symmetry.

When the material works in the elastic domain, the structural condition can be defined by two second order tensor quantities, the elastic stress and strain which are related together by the elastic stiffness, a fourth order tensor, the relation is commonly known as the Hooke's law, equation 2.10.

$$\bar{T} = \bar{\bar{c}}\bar{S}^2 \tag{2.10}$$

In equation 2.10 $\bar{T}$ is the elastic stress which is measured in N/m^2, $\bar{S}$ is the elastic strain which is non dimensional and $\bar{\bar{c}}$ is the elastic stiffness, whose unit of measurement is N/m^2, while its reciprocal is the elastic compliance and it is addressed as $\bar{\bar{s}}$. The notation used to describe the different quantities is the same as in [4].

The electric state of a dielectric can be defined by the vector electric field and by the vector electric displacement, they are related together through the permittivity of the material, which is represented as a second order tensor.

$$\vec{D} = \bar{\epsilon}\vec{E} = \epsilon_0\vec{E} + \vec{P} \tag{2.11}$$

In equation 2.11 the dependence of the electric displacement $\vec{D}$, which is measured in C/m^2, on the electric field $\vec{E}$, whose unit is V/m, by means of the permittivity $\bar{\epsilon}$, which is measured in F/m, is highlighted. The reciprocal of the permittivity is the dielectric impermeability, which is addressed as β in [4]. In the equivalent form ϵ_0 is the permittivity of free space, and $\vec{P}$ is the electric polarization vector.

For both equations 2.10 and 2.11, the material is said to be linear when $\bar{\bar{c}}$ and $\bar{\epsilon}$ are not a function of $\bar{S}$ and $\vec{E}$ respectively. Furthermore the material is homogeneous when the same two tensors are not a function of the spatial coordinates. Finally if all of their elements are equal, the material is defined to be isotropic and its properties do not depend on the direction in this last case.

The piezoelectric effect introduces an additional term in the strain tensor that is proportional to the applied electric field $\vec{E}$. This term is known as the piezoelectric strain tensor $\bar{\sigma}^e = \tilde{e}^T\vec{E}$, and the relationship 2.10 becomes:

$$\bar{T} = \bar{\bar{c}}\bar{S} + \tilde{e}^T\vec{E} \tag{2.12}$$

equation 2.12 expresses the converse effect for an adiabatic process. The electric polarization $\vec{P}$ in piezoelectric materials is related to the applied stress and the piezoelectric effect, which creates polarization proportional to the strain. This relationship can be expressed as:

$$\vec{P} = \tilde{e}\bar{S} + \tilde{d}^T\bar{T} \tag{2.13}$$

---

[2]The following convention will be used to address the tensors' order: $\vec{\cdot}$ first order tensor, $\bar{\cdot}$ second order tensor, $\tilde{\cdot}$ third order tensor, $\bar{\bar{\cdot}}$ fourth order tensor

where the superscript ^{T} stands for transpose. Equation 2.13 represents the direct effect of the stress on the electric polarization of the material.

The piezoelectric constants, that is the 3rd order tensors $\tilde{d}$, $\tilde{e}$, $\tilde{g}$ and $\tilde{h}$ are defined in table 2.8 along with their physical dimensions. These tensors are defined for the direct and converse effects (see table 2.9) and as can be observed from equations 2.13 and 2.12, they are used to formally express the induced stress $\bar{\sigma}^e = \tilde{e}^T \vec{E}$ and strain $\bar{\epsilon}^e = \tilde{d}\vec{E}$. At zero stress condition, the induced stress and strain define the elastic state of the material produced by the external electric field $\vec{E}$.

Property	Symbol	Units
Piezoelectric strain constant	d	C/N
Piezoelectric stress constant	e	C/m^2
Piezoelectric strain constant	g	Vm/N
Piezoelectric stress constant	h	V/m

Table 2.8: Piezoelectric constant tensors

Table 2.9 summons the equations describing the state of the system, in this case state means both electric and structural states. The equations are defined both for the direct and converse effects for an adiabatic process.

Piezoelectric constant	Direct effect	Converse effect
d	$D = \epsilon^T E + dT$	$S = s^E T + d_t E$
e	$D = \epsilon^S E + eS$	$T = c^E S - e_t E$
g	$E = \beta^T D - gT$	$S = s^D T + g_t D$
h	$E = \beta^S D - hS$	$T = c^D S - h_t D$

Table 2.9: Adiabatic piezoelectric equations of state (matrix notation) by [4], the superscripts relate to quantities held constant during measurement, and the subscript t implies that the matrix is transposed

Now that the main parameters and equations which define the physics of piezoelectricity were presented, it is easier to understand the definition of the parameter which is used as the main metrics to compare the performances of the different materials, the coupling coefficient k. This coefficient is defined within the cartesian reference system which in turn depends on the crystal structure of the material as described in [4]. It is possible to write a scalar definition for the parameter once the type of effect (direct or converse), the direction of the electric field or electric displacement and the direction of the stress or strain have been set, in the IRE standard [17] the one-dimensional coupling factor is defined as in expression 2.14.

$$k = k_{31} = \sqrt{\frac{d_{31}^2}{\epsilon_{33}^T s_{11}^E}} \qquad (2.14)$$

The subscripts 3 and 1 indicate the directions of the electric field and the mechanical displacement, respectively. Physically this form of the coupling factor represents a ratio of the conversed energy over the input energy, where the input energy is due to an external electric field while the conversed energy is mechanical. Therefore this parameter is usually associated with conversion efficiency, the higher the coupling factor, the stronger is the electro-mechanical interaction and by consequence the energy conversion.

Now it is even more clear why the inverted flag configuration suits perfectly piezoelectric materials. By observing the flapping mode of the standard flag with respect to the one of the inverted flag, it is possible to notice that the concavity of the inverted flag has one direction, while the standard flag's concavity changes direction along the flag's edge, see figure 1.5. When the piezoelectric material is applied to the flag the sign of the charge which is collected on the electrodes will depend on the direction of the curvature, therefore a standard flag will produce charge annihilation on its surfaces, but an inverted flag will generate charge collection of the same sign on the whole surface of the electrodes.
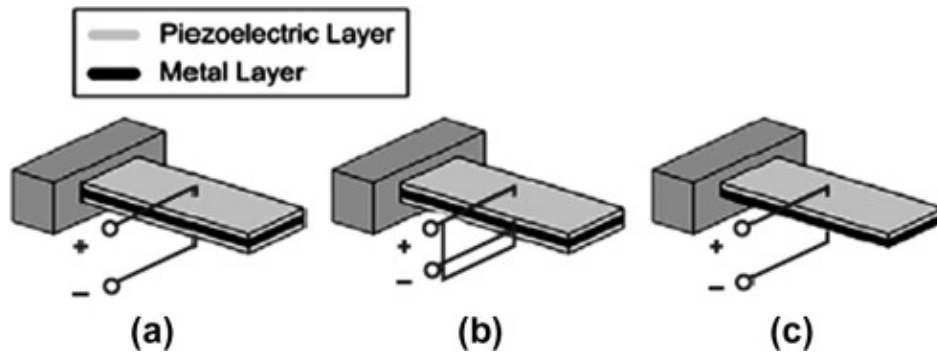
Piezoelectric devices

Figure 2.5: (a) Bimorph cantilever with series connection (b) Bimorph cantilever with parallel connection (c) Unimorph cantilever, by [33]

Generally a piezoelectric harvester consists in different elements, figure 2.5 depicts three typical configurations of the device, two bimorphs (a and b) which have two layers of active material and one unimorph whit one single active layer (c). The designs of figure 2.5 are the most common and they consist in the following elements:

1. stiff substrate, it is the part which sustains the loads and usually has high mechanical properties, in the case of figure 2.5 it consists in a metal sheet but the material can change depending on the application;

2. active substrate, its responsibility is to convert the elastic bending energy into electric energy, the mechanical properties of the piezoelectric materials are relatively poor, for this reason they are coupled with a stiffer substrate;

3. electrodes, usually they consist in sprayed layers of metal such as silver or gold whose task is to collect and convey free charges displaced by the potential difference produced by the active layers;

4. protective film, it is a polymeric coating of the device to prevent it from degradation.

The different substrates can be repeated many times with different thicknesses and connected in different fashions to improve the harvesting performances. This process is not that easy because optimizing the harvester performances does not always mean to optimize efficiency or power transfer, in fact the optimization criteria are different depending on the relative strength of the electro-mechanical coupling [37]. This aspect will be described in a more detailed way in the next section.

In the previous chapter the reasons behind the choice of using the water tunnel to host the experiment were presented. Conventional piezoelectric harvesters are not meant to work underwater. Therefore it is necessary to isolate the device, and this process can be quite expensive, even for small devices. A conventional PVDF harvester generates high voltage but very low current due to the low amount of free charges. Underwater this can result in local parasite currents when there is no proper isolation.

To test the working principle and evaluating the performances and unforeseen issues, a cheap harvester called the firefly and manufactured by PolyK (PolyK firefly harvester) was used.

A picture of the harvester and a table containing its main parameters is reported in figure 2.6. The voltage measured with few tap tests could reach peaks higher than 100 [V] but no current flow could be observed with the oscilloscope[3].

To get an estimation of the current flowing out of the harvester, a low resistance (100 Ω) and a transistor for current amplification were used.

---

[3]An oscilloscope is a device which makes it possible to observe the waveform of the voltage and/or the current flow between two points in an electric circuit. It perfectly suits tasks as the observation of quick events, like the effect of a tap test on a piezo-harvester

Cp	730 pF
Active area	57mmx15mm
Thickness	0.12 mm

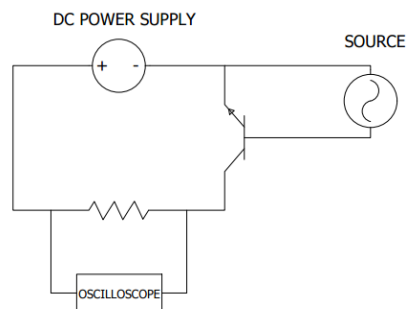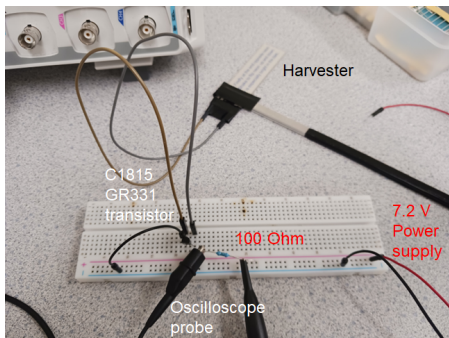Figure 2.6: The firefly and its features

Figure 2.7: Current amplification

The circuit and its scheme are depicted in figure 2.7. The voltage measured with the oscilloscope on the resistor is of the order of 1 V at the peaks, while the power supply was set at 7.2 V. A C1815 transistor has a typical gain value of $h_{FE} = 100$ at 6 V DC excitation. In this case the current source is AC type but $h_{FE} = 100$ is a valid approximation since it will be used to get a raw estimation of the current. Therefore the order of magnitude of the current through the base of the transistor can be calculated as in equation 2.15.

$$I_{be} \simeq \frac{V_{measured}}{Rh_{FE}} = \frac{1}{10000} = 0.1 \, mA \tag{2.15}$$

The harvester was tested in water, no voltage was measured and no flapping mode was observed. As said previously, without a proper isolation the device cannot work underwater, while the reason behind the absence of flapping can be related to the low aspect ratio of the flag mainly. By considering the active area in figure 2.6 the aspect ratio can be evaluated as in equation 2.16.

$$AR = \frac{15mm}{57mm} = 0.26 \tag{2.16}$$

What was observed is very similar to what was found by J. E. Sader, C. Huertas-Cerdeira and M. Gharib in their work [34], that is the existence of different stable states in function of the non dimensional velocity of the fluid flow. Essentially their work is a stability analysis about slender inverted flags. Figure 2.8, by [34], reports the stability map for slender inverted flags on the right, while on the left a scheme of the inverted flag to understand the graph on the right. In this last the magnitudes on the x and y axes are, respectively:

$$k' = \frac{\rho U^2 L^3}{B} = \frac{1}{K_B}; \\ \theta_{end} = \theta(s = 1). \tag{2.17}$$

The angle θ is expressed in radians. When k' reaches a certain $k_{critical}$ a saddle node appears, for $k' > k_{critical}$ there exist three equilibria, the unstable equilibria separates the attraction basins for the remaining two stable states.
By observing the behaviour of the dynamics of the firefly, the straight mode occurred at low k', by increasing the velocity the deflected mode interceded. Basically a infinitesimally slender inverted flag is never globally unstable as a high aspect

ratio inverted flag, but it presents different stable equilibria depending on the non dimensional velocity.
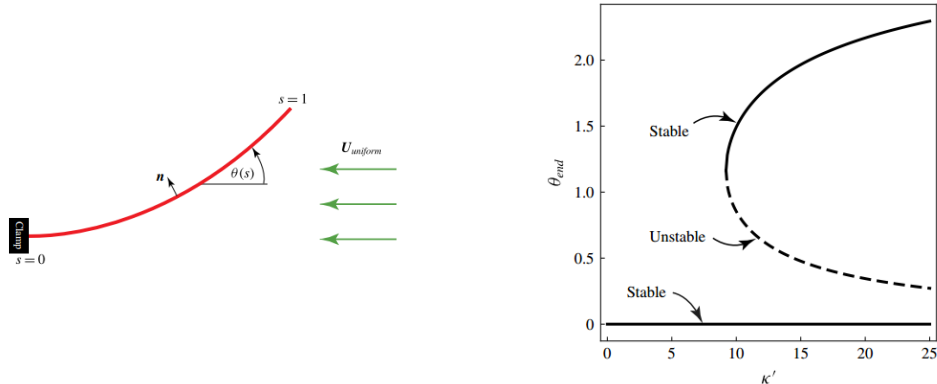

Figure 2.8: Stable states for the slender flag, by [34]

The straight position is always stable but perturbations arising from the turbulence of the fluid flow and imperfections of the material can cause the deflection of the flag to surpass the limit of the basin of attraction of the straight position, in this way the inverted flag ends in the deflected mode.

To solve the issues related to the electric isolation and to the absence of the flapping mode, which is essential for achieving the highest performance for any piezoelectric harvesters, a new design was proposed to the manufacturer and presented in figure 2.9.
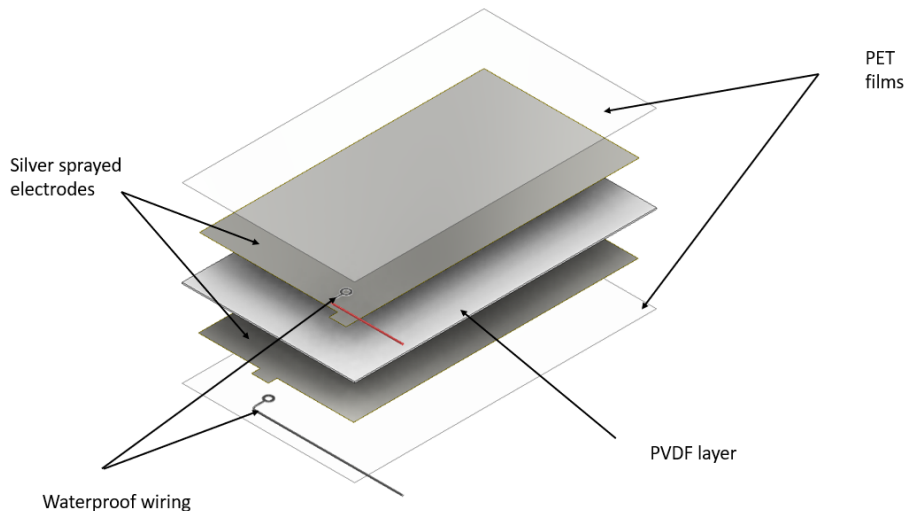
Figure 2.9: Flag design

The elements of the new flag are the same mentioned in the list of piezoelectric harvesters components, apart from the absence of a metal sheet whose duty is to increase the stiffness of the device. This is a unimorph harvester whose active substrate is made of PVDF, the polymeric coating and the connection of the wires to the electrodes have to be assembled in a such a way that the final product is totally waterproof, the manufacturer will be responsible for this technical challenge.

This will solve one of the problems, while to deal with the absence of flapping it was decided to act on the design. First, the aspect ratio was increased to $AR = 0.667$ (active dimensions 3in x 2in), instead the thickness was chosen by taking a PET inverted flag which successfully flapped as reference. The thickness of the reference flag is 11 mil, that is $0.011\,in = 0.28\,mm$, the design thickness is chosen such that $B_{design} \geq B_{ref}$, this condition becomes inequality 2.18 and it is described also in figure 2.10, where the design point is a black circle on the PVDF line.
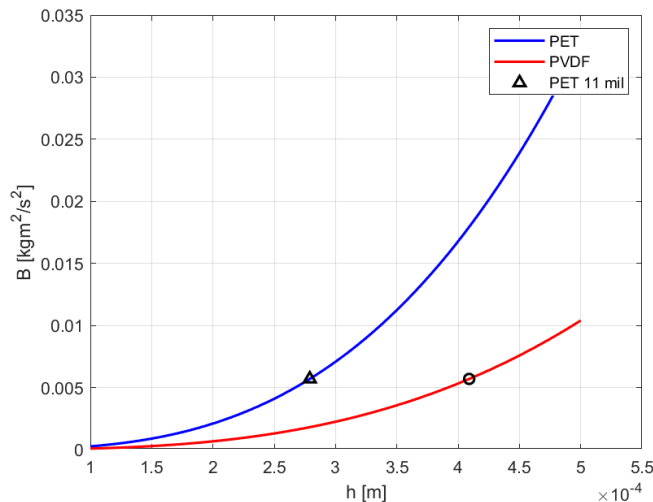
$$h \geq 0.41\,mm \tag{2.18}$$

Figure 2.10: Thickness selection

The manufacturer proposed two solutions to obtain the requested specifics. The first solution consists in assembling four or more Piezo sensors by connecting them in parallel, see figure 2.11 and the table with its specifics. Since the unit elements are connected in parallel, the overall capacitance will be the unit capacitance multiplied by the number of units.

Unit thickness [mm]	0.13
Unit capacitance [nF]	5
Min number of units per flag	4
Connection	Parallel
Final capacitance [nF]	20
Final cost: 2 flags [$]	700

Figure 2.11: Solution 1

Figure 2.16 is the graph which plots the optimal resistance value for power extraction against the flapping frequency on the top (blue line), and its slope on the bottom (red line). This graph is necessary to build a simple circuit which can effectively optimize the power extraction of the device and its slope shows when it is possible to use a constant resistor. Basically, if the flag flaps in the same conditions always, it means that its frequency will vary very few, and if the frequency itself is high enough, as for example close to 1.5 Hz in figure 2.16, a constant resistor of 5 $M\Omega$ could be used, in fact the value of the slope at that point is very low with respect to the optimal resistance.
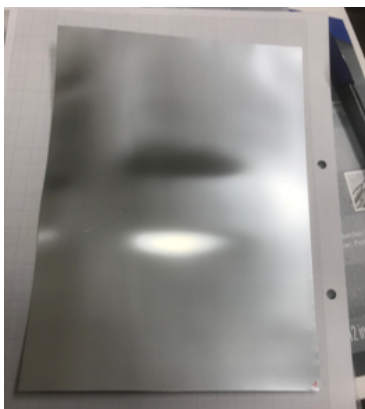
Thickness [mm]	0.5
Capacitance [nF]	0.852
Final cost: 2 flags [$]	1500

Figure 2.12: Solution 2

The second solution proposed by the manufacturer is to use the following product: poled piezoelectric film, see figure 2.12. Basically this option is a single layer solution

and it turns out to be advantageous in terms of manufacturing, but to be unfavorable in terms of capacitance. The details of the second option are listed in table 2.12. The device is a single 0.5 mm thick PVDF layer, by consequence the capacitance will be much lower since its value is inversely proportional to the electrodes' distance which is equal to the layer thickness in this case. The optimal resistance values in this case are much higher, as it can be seen in figure 2.17. The main cons is the elevated cost of this device, because of its golden electrodes.

The external circuit

The difference between the two solutions presented in the previous section 2.3 is highlighted in the graphs of figures 2.16 and 2.17. To explain the meaning of these graphs, first it is necessary to go back to some optimization concepts for the external circuit. First of all, the optimization process depends on the relative magnitude of the coupling coefficient (expression 2.14) with respect to the mechanical damping of the harvester as described in [37]
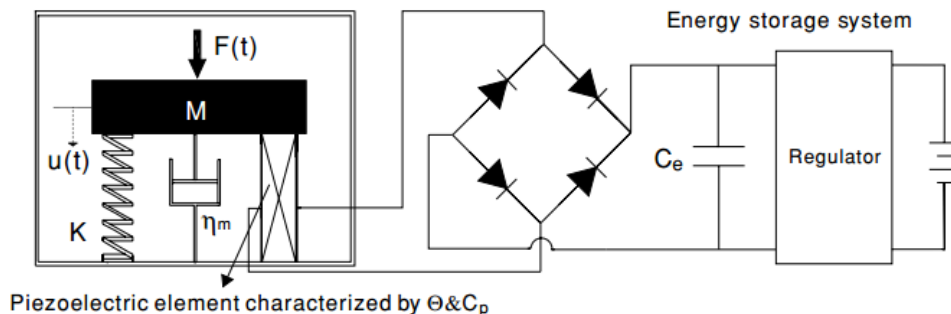

Figure 2.13: Model for a piezoelectric harvester, by [37]

The system made of the piezoelectric harvester and the external forcing term is modelled with a single degree of freedom scheme in most of the literature (see [37], [41], [25]) because of its simplicity and of its fidelty with the real case if the modal density of the system is widely separated and the working point is close to the resonance condition, moreover the harvester in turn is represented by a current source in parallel with its internal capacitance C_p for describing its circuital function. Figure 2.13 is a depiction of the SDOF model for the piezoelectric harvester taken from [37]. The energy produced by the device is meant to be collected in a battery or in any other energy storage device, to this purpose it is necessary to rectify the AC signal and the most common solution is to use four diodes in a Wheatstone bridge configuration. An high capacitor C_e is used to remove the ripple from the rectified signal to obtain a quasi-steady output. Finally the regulator is an adaptive element to obtain a desired output voltage, it can consist in a variable resistor for example.

$$\begin{cases} M\ddot{u}(t) + \eta_m \dot{u}(t) + Ku(t) + \Theta V_p(t) = F(t) \\ -\Theta\dot{u}(t) + C_p\dot{V}_p(t) = -I(t) \end{cases} \tag{2.19}$$

Equations 2.19 represent the SDOF system of the harvester as a mass-spring-damper-piezo model whose parameters for the different elements are M, K, η_m respectively. The electro-mechanical coupling occurs through the parameter Θ which defines the coupling coefficient as in equation 2.20, look at the similarity with the former definition 2.14 given in the standard [17].

$$k^2 = \frac{\Theta^2}{KC_p} \tag{2.20}$$

The scheme of figure 2.13 can be further modelled as in figure 2.13, where the DC regulator and the battery are changed with an equivalent resistor R. Finally if the forcing term can be approximated by an armonic function of angular frequency ω as in equation 2.21,
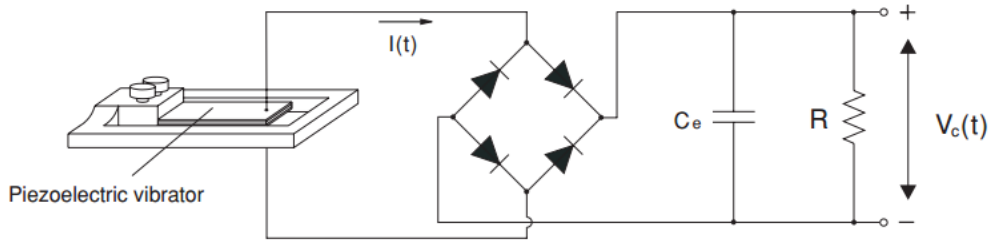
Figure 2.14: Model for a piezoelectric harvester, by [37]

$$F(t) = F_0 sin(\omega t) \tag{2.21}$$

then efficiency can be defined in function of the non dimensional parameters in expression 2.22, where ω_{sc} is the short circuit resonance frequency, and in function of the coupling factor 2.20.

$$
\begin{aligned}
\xi_m &= \frac{\eta_m}{2\sqrt{KM}} & \omega_{sc} &= \sqrt{\frac{K}{M}} \\
\Omega &= \frac{\omega}{\omega_{sc}} & r &= C_p \omega_{sc} R
\end{aligned}
\tag{2.22}
$$

The essential information from [37] is that the final form of the efficiency can be written as equation 2.23.

$$\epsilon = \frac{r \frac{k_e^2}{\xi_m}}{(r\Omega + \pi/2)^2 + r \frac{k_e^2}{\xi_m}} \tag{2.23}$$

For low electro-mechanical coupled systems, that is for low values of the ratio $\frac{k_e^2}{\xi_m}$, the efficiency and the power transfer on the external load R are optimized at the same time. Finally it is possible to assess that for a PVDF harvester, which has low coupling, maximum power transfer on an external load means maximum efficiency.

Since the purpose of this study is not to build an harvesting circuit, but instead to measure the efficiency of the different configurations, it is possible to use a way more simple circuit than the one depicted in figure 2.13 as for example the one in figure 2.15, where the source is directly connected to a variable resistor in parallel to an oscilloscope to measure the voltage. This is a test circuit since acquiring the data with the oscilloscope does not have any solutions for rapidly saving it, in place of the oscilloscope it is possible to connect an analog input to a DAQ system.
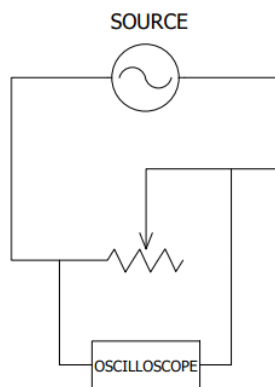

Figure 2.15: External circuit for power extraction measurement

The main problem of this configuration is that the variable resistor should be adjusted manually according to the impedance matching condition stated in [41] and specified in equation 2.24. This expression is valid only in case of the simple circuit of figure 2.15, adding a rectifier and a voltage converter would change the condition for power transfer optimization. To avoid reflections of the signal, since the measurement

31

is performed for the AC case, it is important for the resistor and the measuring device to have similar impedance.

$$r\Omega = 1 \rightarrow C_p\omega R = 1 \rightarrow R_{opt}(\omega) = \frac{1}{C_p\omega} \tag{2.24}$$

For now it is assumed that the effect of the measuring device is negligible, by plotting the value of R_{opt}, equation 2.24, for the solutions of figures 2.11 and 2.12, the graphs in the pictures 2.16 and 2.17 are obtained, where the blue line represents the value of R_{opt} and the red line is its slope.
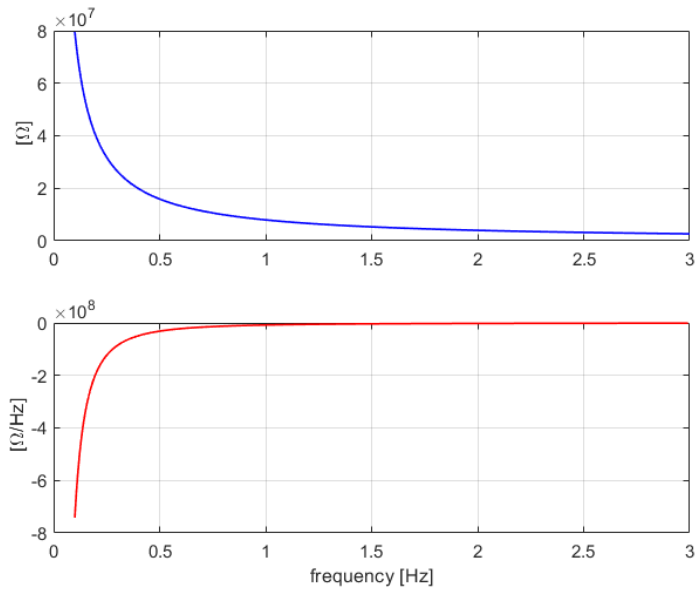
Figure 2.16: R_{opt} to improve power extraction on a resistive load, solution 1

Because of the small value of the internal capacitance of the second solution, the value of the optimal resistance in this case is much higher than the first solution, there is an overall difference of two orders of magnitudes. This aspect is important because potentiometers available in the market cannot reach high resistance, while low resistance potentiometers are much more common and affordable. Instead, the slope of the optimal resistance with respect to the signal frequency is important to understand when it is possible to use a constant value of the resistance to obtain something close to the maximum power transfer.
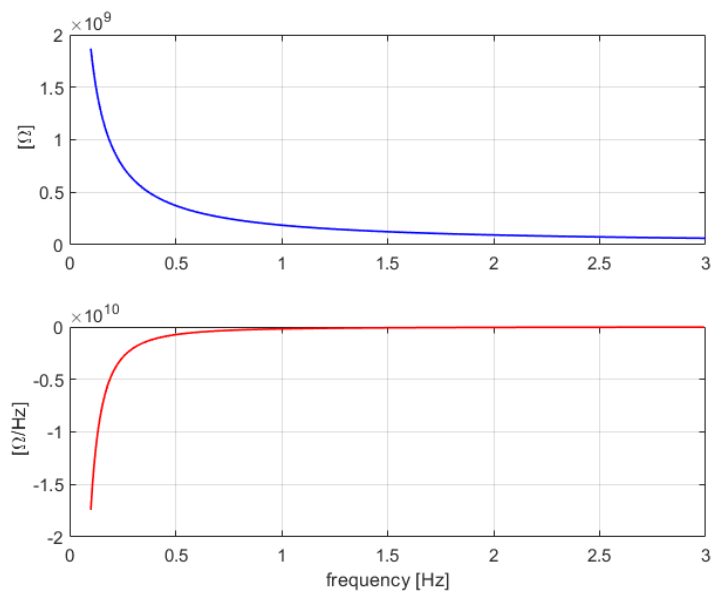

Figure 2.17: R_{opt} to improve power extraction on a resistive load, solution 2

When the slope is low relative to the value of R_{opt} then it is valid to use a constant value of the resistor close to R_{opt}, in fact in the case of the inverted flag the frequency is

not expected to change that much among the several arrangements. In chapter 2 the estimation of the flag flapping frequency produced the result of expression 2.9, so the frequency of the signal can be considered to be lower than 0.5 Hz. From the preceding graphs it is possible to see that the value of the slope is important with respect to the value of the optimal resistance, this means that a small deviation of frequency produces a big change in R_{opt} moving the whole system far from the maximum power extraction point. For this reason it is not possible to use a constant load to measure the output power.

2.3.2 Method 2

In this second approach to efficiency the magnitudes of interest are the aerodynamic drag on the flag and the elastic bending energy. The non dimensional parameters which are used to evaluate them are: the drag coefficient (equation 2.25) and the non dimensional bending energy (equation 2.26).

$$C_D(t) = \frac{D(t)}{\frac{1}{2}\rho U^2 LW} \tag{2.25}$$

$$E_S(t) = \int_0^1 \frac{1}{2}\beta k^2(s,t)d\left(\frac{s}{L}\right) \tag{2.26}$$

$$K(s,t) = \left|\left|\frac{d\hat{T}(s,t)}{ds}\right|\right| \tag{2.27}$$

Both the parameters are function of the time so they are instantaneous values. The drag coefficient is written as the ratio of the instantaneous drag on the flag over the dynamic pressure of the flow on the area of the flag, while the non dimensional bending energy is written in the same form defined in [20]: s is the curvilinear coordinate along the flag, the origin lies in the trailing edge of the flag and the leading edge corresponds to the coordinate s=L, see figure 2.18 which represents an inverted flag during deflection along with the cartesian reference frame (in white) which is constant in time and the instantaneous curvilinear reference frame (in red), whose origin is fixed in the trailing edge; β is the non dimensional bending stiffness, which in this investigation is addressed as $\Pi_5 = K_B$; $k(s,t) = K(s,t)L$ is a non dimensional curvature and it is both function of the time and of the curvilinear coordinate, while $K(s,t)$ is the dimensional curvature and it is defined as the quadratic norm of the derivative along s of the versor tangent to the curve $\hat{T}(s,t)$, see equation 2.27.
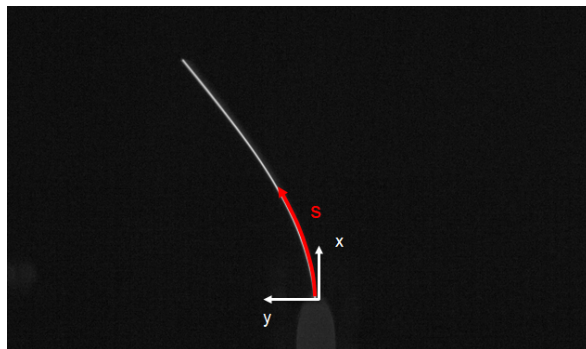

Figure 2.18: Reference frame

In [16] it is pointed out how the two parameters C_D and E_S are linearly correlated, this signifies that collecting both of them synchronously can prove consistency and validity of data collection if they match in time.

The reason why it is not possible to estimate the actual efficiency of the harvesting technique is that there is no evidence so far of a correlation between the amount of elastic energy converted to electric potential and the two parameters which are measured with this method.

In equations 2.25, 2.26 and 2.27 the only quantities which are output of the dynamics of the flags are the instantaneous drag $D(t)$ and the instantaneous and local curvature $K(s,t)$. Therefore two independent measurement chains are required, one for each magnitude.

The drag is defined as the force experienced by a body immersed in a uniform flow in the direction of the undisturbed flow, then a single point load cell can be used if placed with the proper orientation. About the dimensional curvature[4], first of all slender flags will be used, and despite the higher relevance of the SEVs for these flags the motion can still be accurately described in two dimensions, see [3] and section 6 in [42]. Basically, the dynamics cannot be well described by a 2D model when K_B is too low because of the occurrence of chaotic behaviour and when the effect of gravity is not negligible with respect to fluid inertia. In this case study K_B will be limited between the extrema of the flapping mode, while the effect of gravity in water is negligible, moreover the clamp direction can be set parallel to the local gravitational field, in order to remove any possible effects due to this last.

Therefore, to observe the flapping of the flag it is sufficient to record the motion of its edge, a single camera is sufficient for one single flag and from the tracking of the body within the frames it is possible to extract the value of the dimensional curvature along the curvilinear coordinate for each frame. To collect both the force data and the flag position at the same time, it is necessary to synchronize the the two acquisition techniques.

Since a single parameter is needed to compare the harvesting potential of the different arrangements, the time sequence of both the drag $D(t)$ and the non dimensional elastic potential energy $E_s(t)$ need to be post-processed to some parameters which represent the whole time sequence. As an example it is possible to consider the time mean integral of the two quantities, see [16].

$$
\begin{aligned}
\bar{C}_D &= \frac{1}{T} \int_{t_0}^{t_0+T} C_D(t)dt \\
\bar{E}_s &= \frac{1}{T} \int_{t_0}^{t_0+T} E_s(t)dt
\end{aligned}
\tag{2.28}
$$

In equation 2.28 T is the flapping period of the flag and t_0 is any instant in time. Therefore the parameters $\bar{C}_D$ and $\bar{E}_s$ will be the discriminant to assess if one configuration is potentially more efficient than another in this second method. At this point of the discussion, based on what was discussed in section 2.2, the features of both the load cell and the camera can be set. Obviously, with this second method for efficiency estimation PET flags can be used, this polymer is very cheap, especially in the low amounts needed for this experiment. By observing table 2.4 the limits for the flapping mode are known for the selected design and this information is sufficient to do a conservative estimation on the load cell maximum capacity.

$$
F_{max} = \frac{1}{2} \rho U_{crit}^{max\,2} A_{blocked} = 1.36\,N = 138.6\,gF
\tag{2.29}
$$

In equation 2.29 F_{max} is the maximum force that the load cell can possibly experience, it is calculated as the fluid momentum over the ideally highest swept area $A_{blocked}$ (see equation 2.3) at the maximum velocity in the flapping regime U_{crit}^{max}. Therefore a standard 500 grams maximum capacity load cell can be used. The estimation of the frequency of the flapping as described in equation 2.9 is useful for having an idea of what will be the Nyquist frequency of the phenomenon, see equation 2.30.

$$
f_{Nyquist} = 2 \cdot 0.391 = 0.782\,Hz
\tag{2.30}
$$

The acquisition of both the force data and the images of the flags must be higher than $f_{Nyquist}$, and its low value does not represent a problem to the instrumentation available in the lab.

---

[4]Beside the formal definition 2.27 another way to intend the curvature is the inverse of the radius of the circle tangent to the curve in a specific point: $K(s) = \frac{1}{R_t}$.

2.3.3 Comparison of the two methods

The first method can measure efficiency very quickly and reliably, and it is remarked that the actual efficiency of the harvesting technique is obtained. The main drawbacks are the elevated cost of the waterproof piezoelectric harvesters and the time demand which the realization of the external circuit takes. This last is not a trivial task and it cannot be neglected, in fact without the flexible adaptive load the real optimum efficiency would not be measured, instead some efficiencies will be measured.

On the other hand the second method is technically easier and faster to realize, but its main drawback is the large post-process it requires and the great amount of time necessary to collect the data. So far an estimation of the flapping frequency is available, $f = 0.391\,Hz$, to understand the behaviour of the system it is necessary to acquire the data for a long enough time span, as for example 50 periods, this turns into acquisitions which last more than 2 minutes, see equation 2.31.

$$t_{acquisition} = \frac{50}{0.391} = 127.9\,sec \qquad (2.31)$$

Despite these cons, the second method was finally chosen. The decision was dictated by the available time to complete the project, since the second approach offers a faster way to build and assemble the setup than the first method, there is more time to test the setup assembly and to solve the unforeseen problems which will emerge.

It was not discussed about flow visualization in this chapter. To this case study flow visualization is essential to understand any couplings which can occur between the two flags but its practical realization is far from easy. There are different ways to cope with this task (see [7]), like using particle image velocimetry (PIV) or other flow tracers (dye, hydrogen bubbles or soap films) but the most important challenge is to perform it in a 3D fashion. The purpose of the flow visualization is to assess the effect of the interaction between the 3D vortexes[5] produced by the two flags, see for example image 1.15, for this reason it is necessary to perform a three dimensional visualization. It is anticipated that no flow visualization was performed in this experiment because of the time limit, but some speculations and solutions are described in the final chapter 5.

---

[5]A 3D vortexes is obtained thanks to the mixing of the leading edge and side edges vortexes of the inverted flag, the trailing edge vortex is important only for tandem arrangements where the two flags are very close one another, but generally it is not much relevant in the inverted flag configuration

Chapter 3

The experiment

3.1 The experimental setup

In this section the design and assembly of the experimental setup will be described. The design process starts with the model (3D computer aided design reconstruction) of the facility test section in which the experiment will be performed, the water tunnel, and a report of the available equipment. The second part describes the design of all the parts which are needed to assemble the setup, these parts include both the pieces which need to be machined and the parts available on the market and which can be bought. The third section will describe the assembly procedures and since different unforeseen issues came up in the first assembly a final section will describe their resolution through a new design.

3.1.1 Available equipment

The CAD of the facility test section is the starting point for the experimental setup to be designed, in fact it is possible to check that the different parts moving one with respect to the other do not interfere and that the mechanical couplings are correctly designed. Since many parts are simple, they can be machined through subtracting manufacturing, in this case it is essential that the drawings are correct because once the part is completed it is not possible to bring the material back on the piece.
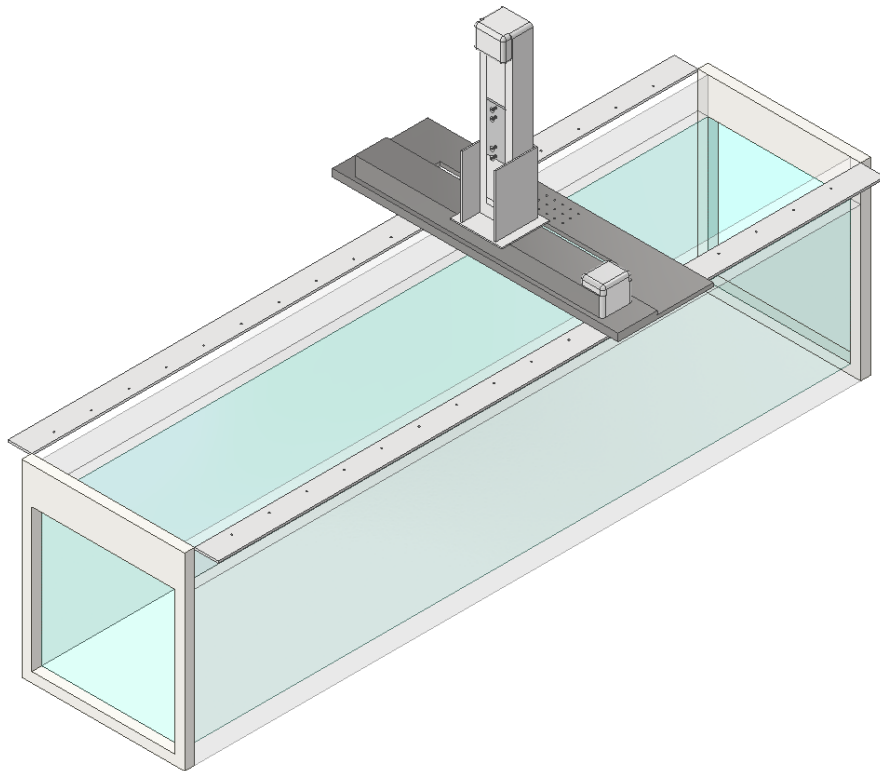

Figure 3.1: Test section and traverse system CAD

Figure 3.1 depicts the CAD of the water tunnel test section along with the available supporting structures which can be used to mount the setup. The dimensions of the test section were reported in section 2.2, but they are listed here in table 3.1 as well.

Dimension	[m]
Width	0.45
Height	0.45
Length	2.13

Table 3.1: Test section dimensions

Obviously the test section width is not constant, it needs to diverge to account for the boundary layer growth, in this way the velocity profile in the central part of the test section remains uniform. The slope of the divergence of the test section is small compared to its dimensions, for this reason it was neglected in the CAD. Now some more details about the test section are pointed out.

The walls of the section are made of acrylic plates welded together by means of solvents[1], the acrylic structure is mounted to the water tunnel loop through a metal frame. At the top of the frame, two drilled metal stripes run along the length of the chamber, see figure 3.1. It is important to keep in mind that these two stripes are curved to follow the divergence of the chamber, and the holes are not placed in a straight line because of this. An outer metal frame, which is not present in the model of figure 3.1, holds two rails parallel to the length of the test section on which the traverse system can run, which is depicted at the top of the chamber in figure 3.1. The traverse system is made up of two Unislides by Velmex,Inc., it is a device like the one in figure 3.2.

Figure 3.2: Linear motorized Unislide MB90 Series by Velmex,Inc.

The Unislide simply consists in a screw ball mechanism led by a stepper motor, the screw ball is connected to a plate on which customized supports can be linked by four screws. In the traverse system in figure 3.1, a Unislide is connected vertically to a second Unislide placed horizontally to the ground and crosswise with respect to the length of the test section. In this way the traverse system can move three orthogonal directions.

The stepper motors which drive the screw nuts can be commanded through a controller, which is also available in the flow visualization lab at Auburn University. The controller is a VP9000 model by Velmex,Inc. and figure 3.3 portraits its hardware, it can control up to four different stepper motors and it can receive input signals in three different ways:

---

[1]First the acrylic is melted with the solvent, when the solvent dries out a resistant waterproof welding is obtained
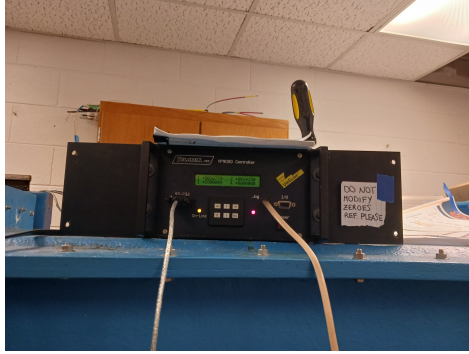
Figure 3.3: VP9000 stepper motor controller by Velmex,Inc

1. the first method is by using a jogger;

2. the second possibility is to write a program from the interface of the controller, with respect to the jogger this last method makes it possible a precise control by setting the number of steps the motors have to move but it is tedious to input even a single command line;

3. the last controlling mode is through serial port RS-232 interface, the controller can be connected to a computer through the serial port and the commands can be send through a command string, this is the best way to obtain precise positioning with very few time because it offers different possibilities to automate the process, this aspect will be described later on in this chapter.

The method number three of the preceding list is the best, the software for interfacing the controller through the serial port was written in LabVIEW and it is detailed in appendix D.
The remaining available equipment from the AFRG lab which is not directly related to the design and assembly of the setup but that will be used for data collection is described in appendix B.

3.1.2 Design of the structural elements

Here the design process of the structural supports is described along with the mechanical process for their manufacturing, in fact the technical drawing themselves need to take into account how the different parts will be produced.
Thanks to the estimations made in the previous chapter it is possible to perform a static analysis to predict if the rigidity constraints on the parts will be satisfied. There is no need to check for robustness constraint since the load cell, which is the most sensible part of the supports, was chosen based on its maximum load capacity in a conservative manner.

Figure 3.4 depicts the support which will be used for the frontal flag, this design is actually the second version of a previous one which was used to test the firefly, see figure 2.6. The previous model was meant to produce the least amount of pollution by the mast in the wake of the flag, and its design took into account only the dynamics to avoid resonance between the mast itself and the flag, but the rigidity constraint was not satisfied. The first support design will not be described, because it is not relevant. The design in figure 3.4 aims at solving the problems of the first design, at this purpose a static analysis was performed to check for rigidity, while the method for predicting the normal frequency will be described later.

As mentioned in section 2.3.2, a 500 grams maximum capacity load cell can be used to satisfy the condition in equation 2.29. The choice fell on the 500g load cell by Uxcell which is represented in figure 3.5, it is a single point, single direction load cell which is commonly used in kitchen balances. This device uses four strain gauges, which are arranged in a Wheatstone bridge configuration, to measure the shear in the measurement direction. Thanks to an external power supply, which is recommended not to be higher than 5 Volts, the resistance on the strain gauges gets modified when
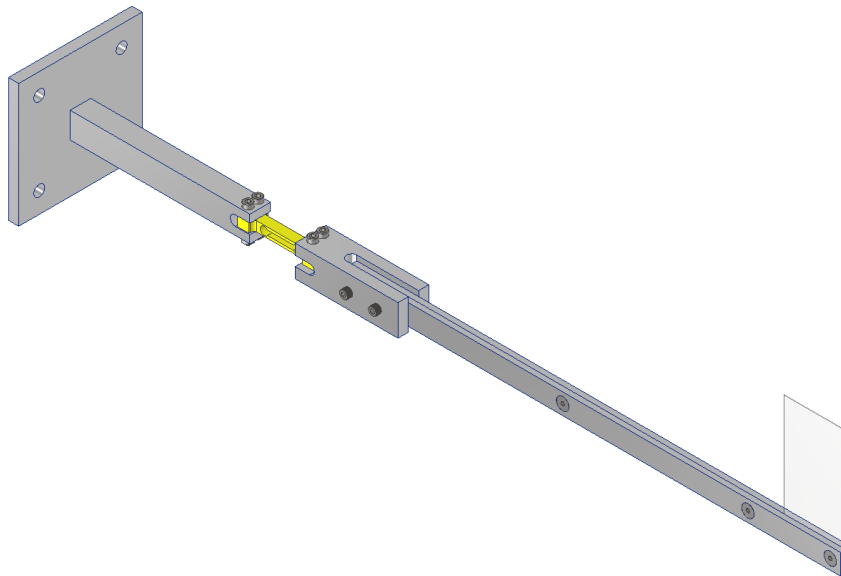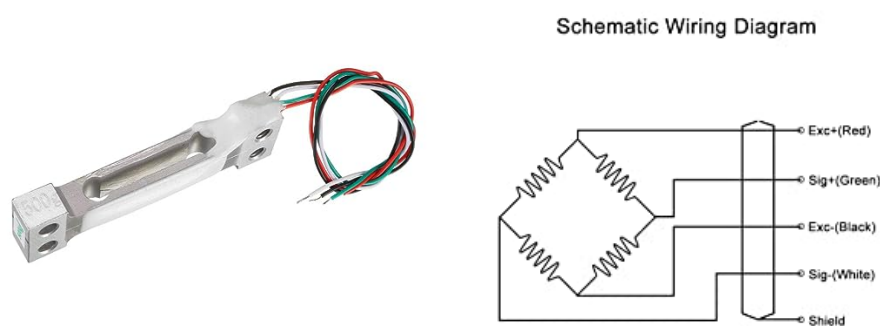
Figure 3.4: Support of the frontal flag

Figure 3.5: Load cell by Uxcell and its wiring diagram

the metal element gets deformed. The output voltage signal is proportional to the shear deformation on the load cell, in fact the Wheatstone bridge configuration along with the strain gauges placed on the thinnest parts of the aluminum support makes it possible the annihilation of the voltages produced by the bending deflection of the symmetrically placed gauges. In the wiring scheme the plus and minus signal pins are used to collect the signal, the remaining two pins are used for the power supply. The yellow component in figure 3.4 is the load cell itself, and it links the part on which the flag will be mounted to the upper portion which will be fixed on an external structure. The analyses were performed on the frontal support only, since the rear one has the same design, only the upper portion is different, because it will need to be mounted on the Unislide (see figure 3.2).

Static analysis of the frontal support

Two analyses were performed with two different loads but same constraints. These last consist in four pins in the top plate's holes and a clamp over its whole upper surface, the plate will be screwed on an external supporting plate, the pins represent the screws' axes while the clamp mimics the effect of the static friction. Two different loads were applied for the two analyses, the first in the streamwise direction, which is parallel to the length of the flag, and the second one in the transverse direction. The magnitude of the forces is the same and equal to the maximum estimation of equation 2.29. Figure 3.6 reports the result in terms of displacement for the configuration with load applied in the streamwise direction, the load was applied at the tip of the mast to make the analysis as much conservative as possible. There are two main aspects to

notice: the first is the value of the maximum displacement which is 0.0043 inches, so the rigidity constraint for the first configuration is satisfied, in fact by considering the ratio $\frac{max\,displacement}{L} = \frac{0.0043}{3} = 0.143\%L$ the maximum displacement is very low with respect to the flag length; the second aspect is the deflection of the load cell, now it is easy to understand why only the shear stress is measured with this device.
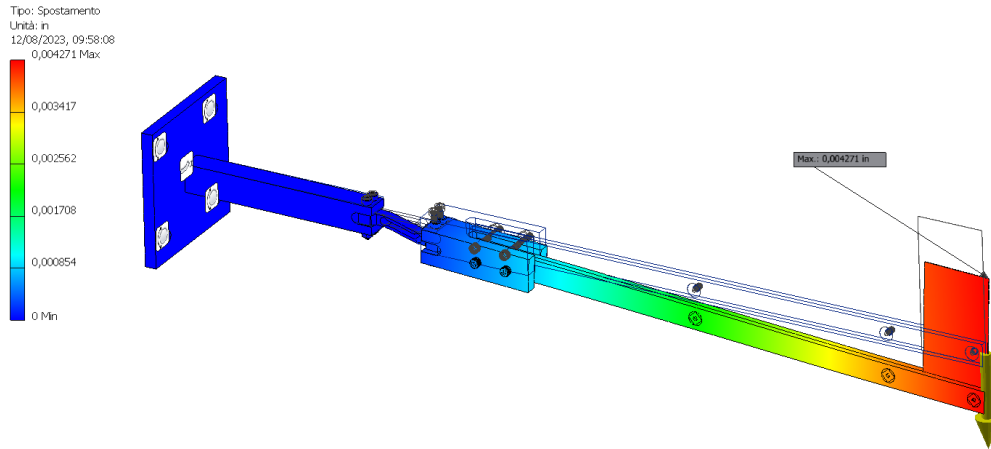

Figure 3.6: Displacement result of the static analysis: load in the streamwise direction

In figure 3.7 the safety factor[2] distribution from the same simulation of figure 3.6 is reported. It is evident that the structure should be safe under the theoretically highest load condition, but the minimum safety factor is 0.27 in correspondence of one of the screws which keeps the mast connected to the load cell. Since the most sensible part of the structure is the load cell, the lowest value of this factor has to be due to some conflicts or problems in the numerical analysis, and it will be ignored.
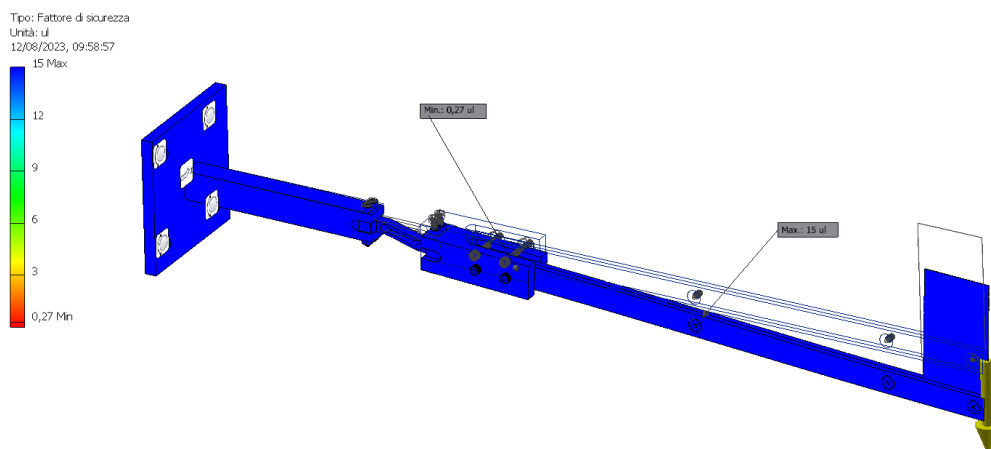
Figure 3.7: Safety factor result of the static analysis: load in the streamwise direction

The flag is designed to achieve the flapping mode in the water tunnel, so it is necessary to check that that the rigidity constraint is satisfied also in the transverse direction to the stream. Figure 3.8 is the displacement distribution for the second load configuration while figure 3.9 reports the safety factor distribution for the same configuration. Also in this case the highest displacement is only 0.007 in, which is equal to $0.233\%L$, a very small percentage of the flag length. Reminder: the magnitude of the simulated load is much higher than the actual force which the structure will experience because of the flag's drag, therefore the displacements will be even lower.

---

[2]The safety factor is defined as the ratio of the rupture stress of the material over the local stress, which can be evaluated in two ways mainly: with Tresca or Von Mises criterions.
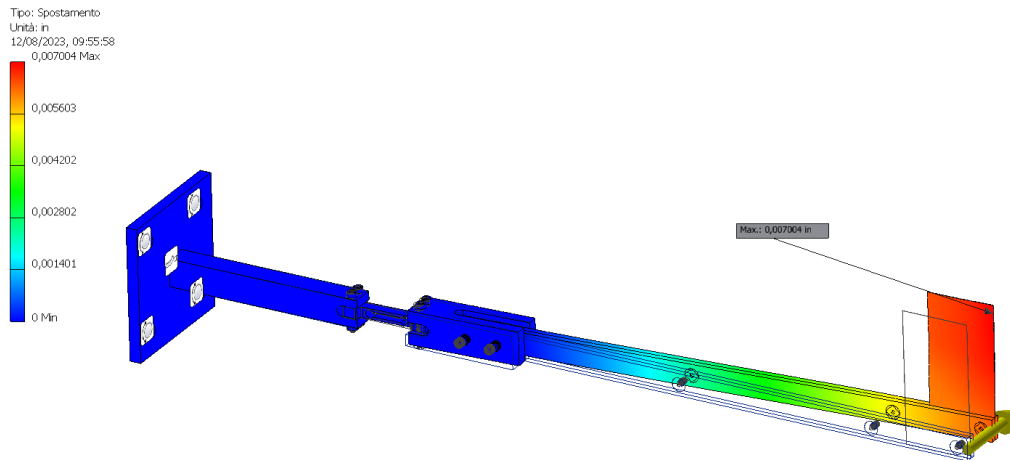
Figure 3.8: Displacement result of the static analysis: load in the transverse direction

The safety factor is high on the overall structure, so there should not be any issues, again a very low value is registered on one of the screws but most of the stress should be on the load cell instead, so it is assumed that those values are due to some issues in the generation of the contacts within the support.
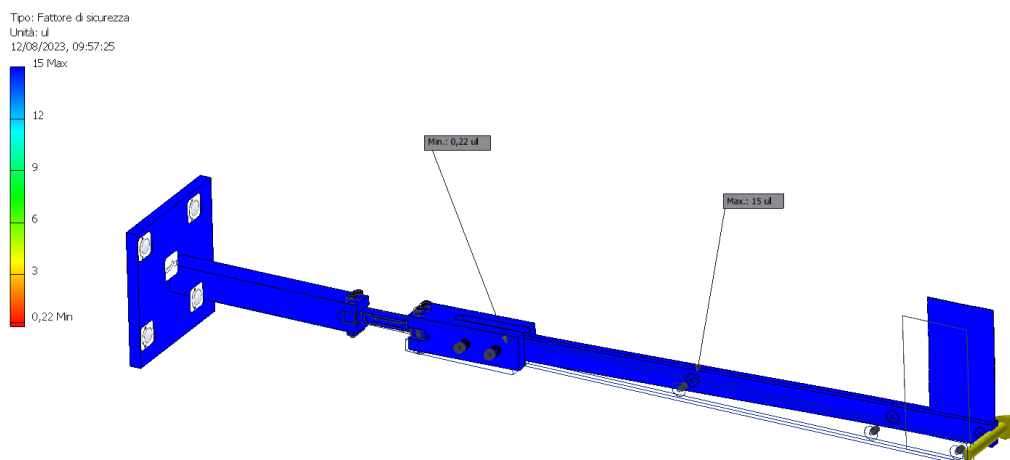

Figure 3.9: Safety factor result of the static analysis: load in the transverse direction

Dynamic analysis of the frontal support

The next step is to get an estimation of the first natural frequency of the support, if it is much higher than the flapping frequency of the flag (see equation 2.9), there will be no risk for resonance to happen.
The main problem relative to this evaluation is that the support will be immersed in the water, so the classic linear stability analysis will not work and neither the numerical analysis will be accurate. Since the configuration is that of a cantilever beam, it is possible to use the same expression for the first natural frequency by just modifying the linear mass distribution parameter by taking into account the added mass of the water.

$$f_1 = \frac{3.516}{L^2}\sqrt{\frac{EI}{\mu}} \tag{3.1}$$

The expression for the first natural frequency of a cantilevered beam is reported in equation 3.1, where I is the lowest second moment area and μ is the linear density, which is assumed to be homogeneous. Figure 3.10 shows the relevant added volume of water to take into account for calculating the natural frequency of the mast.

Water is added only on the part which is supposed to be immersed, and the natural frequency will be calculated for this part as well, but the actual clamp of the whole support is at the top plate, therefore the actual natural frequency of vibration will be lower than the one which will be estimated in the following because of the overall higher length of the mast.

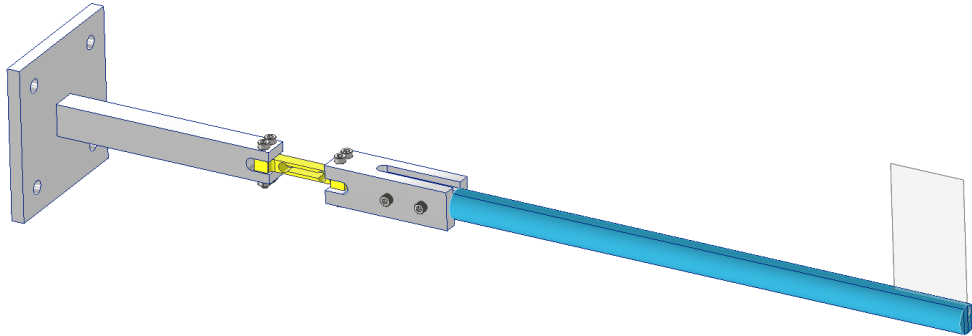The method used to distribute the added water around the cylinder is described in [19] in chapter 13.

Figure 3.10: Added mass of water

$\rho_{aluminum}$ $[kg/m^3]$	2700
ρ_{water} $[kg/m^3]$	1000
E $[GPa]$	69.0
c $[m]$	0.0127
t $[m]$	0.00635
L $[m]$	0.267
I $[m^4]$	2.71E-10
μ $[kg/m]$	0.344
f_1 $[Hz]$	58.0

Table 3.2: 1st natural frequency

Table 3.2 reports all the required parameters for equation 3.1 along with the final result. Compared to what was obtained in equation 2.9, 58 Hz is high enough to avoid resonance with the flapping flag, but there is no clue about flutter instability on the support by now. The flutter is a dynamic instability and it occurs at a certain velocity of the fluid flow which depends on the material and the design of the structure and on its boundary conditions. Because of the lack of means to get an estimation of the water velocity for the onset of the flutter, it will be verified experimentally. The support of the rear flag is the same as the frontal one, but it is connected to a different external structure which can be assumed to be very stiff, so the analyses performed for the frontal support are valid for the rear support as well.

3.1.3 Manufacturing processes and assembling procedures

The manufacturing process of the different parts starts with the technical drawings and the material selection at the vendor. All the parts are fabricated in aluminum, in the analyses presented in the previous section the material was already selected for all the pieces. Aluminum is a convenient choice because it is a good trade off between weight and stiffness, in fact the supports have to be as firm as possible but at the same time they are required to be lightweight to produce a high natural frequency. Furthermore

aluminum is a cheap metal and it is ductile to be processed by classic subtractive methods. Section A of the appendix contains the drawings of the pieces of the final setup, the drawings of the older parts have not been included to avoid confusion among the different parts. The drawings contain details about the parts' dimensions and tolerances, along with material and quantity for each component, the views follow the third dihedral standard.
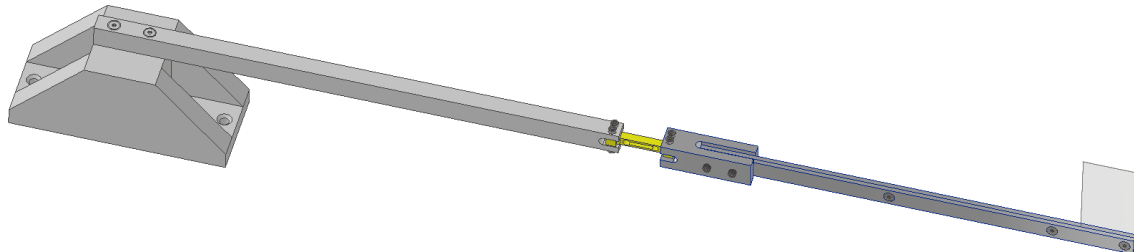

Figure 3.11: Rear support

The rear support is depicted in figure 3.11, as previously mentioned the assembly which consists in the load cell and the connecting structure to the flag is the same as the frontal assembly, the upper part is different because it has to be linked to the Unislide (figure 3.2).
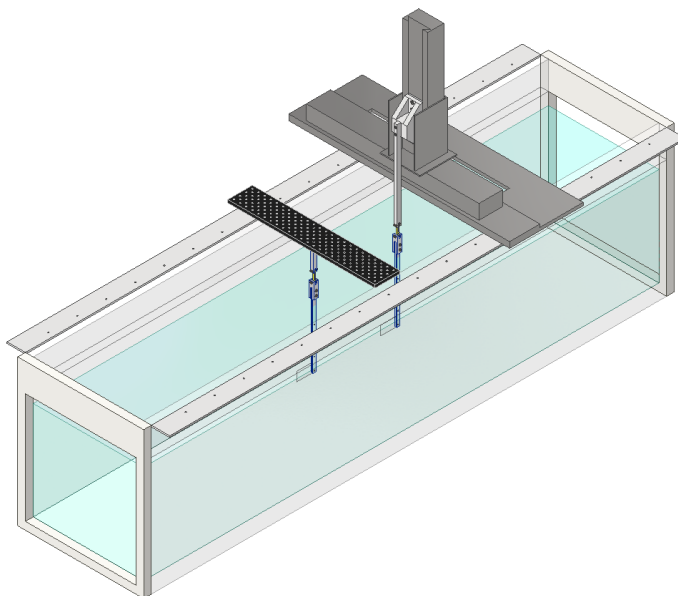
Figure 3.12: First setup

The main piece which will be screwed on the slider is cumbersome and expensive but its design satisfies the minimum dimensions to avoid elements' contact during the motion of the slider. The piece has been manufactured by subtraction at the computer numerical control (CNC) mill, the process consists in preparing a STEP file for the machining path, selecting the proper tool, its spin and displacement velocities depending on the material and performing post processing on the coupling features, like holes in this case (for more details see the technical drawing in appendix A). Usually the milling process is made up of multiple phases and for each of them a different clamp is used for the tool to reach all the surfaces of the part. The other parts are more simple

and can be obtained by using the manual mill, the longest elements' were designed according to the available material from the vendor, in this case McMaster, so that no manufacturing was necessary on the beams' cross dimensions. The boxed quotes in the drawings refer to those dimensions which are assumed to be datum features for the pieces. It has to be pointed out that only the technical drawings of the parts of the final assembly are reported in the appendix, nonetheless the design is very similar to the preceding one but adapted to a different load cell.

The final assembly looks like the one in figure 3.12, some supporting elements are still missing in this design, therefore some provisional wooden equipment was used to fix the black front plate to the frame of the water tunnel.

Standard assembling procedure (SAP)

To reduce as much as possible the uncertainty in the data collection, the parts which are connected one to the other are aligned with a self leveling laser which is shown in figure 3.13.

Figure 3.13: SKIL self leveling laser

First the two load cells are connected to the top supports, whose drawings are reported at the third and fourth page of the appendix A. As shown in figure 3.14, the support is placed on a flat surface and the load cell position is adjusted until the desired alignment is obtained. The load cell in figure 3.14 is different from the load cell in figure 3.5, in fact it is part of the final assembly.
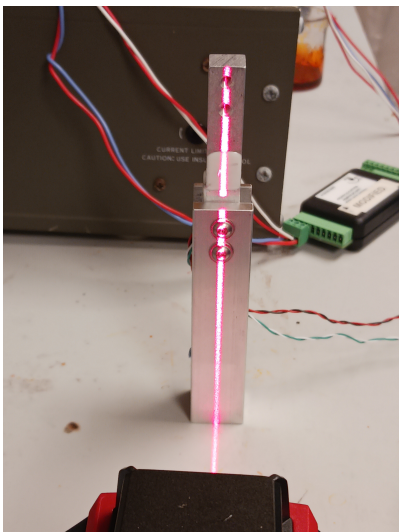

Figure 3.14: Load cell alignment

Figure 3.15: Mast alignment

The second step of the procedure is to align the flags at the center of the test section, in fact the further they are from the walls, the less will be the wall effect on their dynamics. At the same time the elements are positioned vertically in the correct orientation, the schematics of figure 3.16 describes well this phase. In the figure the laser is positioned by setting some marked traverse over the test section, at least two are required and the further away they are one another, the more precise the sheet position will be. These alignments are necessary despite the fact that the assembly parts are super constrained, in fact there is always some play in the couplings.
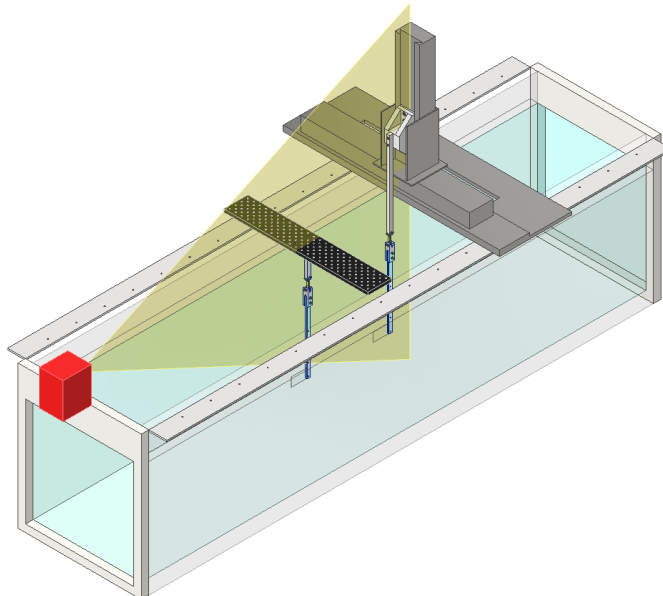
Figure 3.16: General alignment

The correct alignment with the flow stream is assumed to be obtained thanks to the geometry of the system. The last step is to align the ending parts of the two flags' support perpendicularly to the water surface, the same laser is used in this case and the process is performed as shown in figure 3.15, in which the light was turned off to make the laser sheet to appear brighter. Finally the right position of the elements is checked by using a leveling device as shown in figure 3.17.
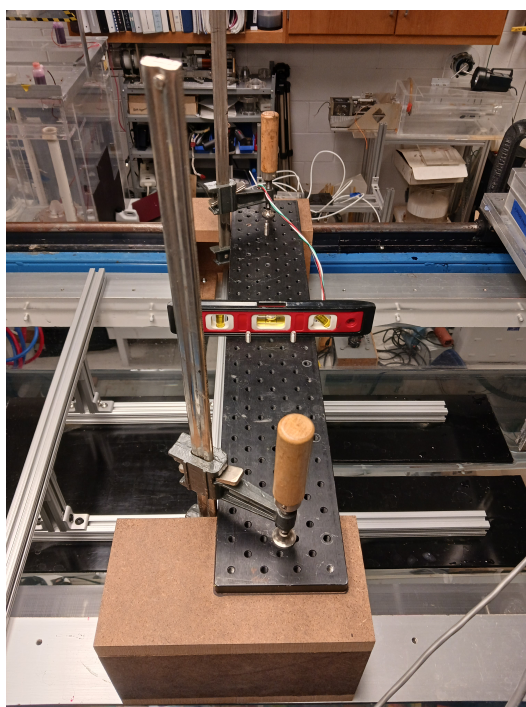

Figure 3.17: Leveling

3.2 Preliminary experiment

In this first experiment only load cells' data was collected because the main purpose was to verify the integrity of the setup, to look for unforeseen problems and to have some first insights on the overall behaviour of the coupled flags.

3.2.1 Acquisition chain

The acquisition chain consists in the elements which make up the whole measurement process. In the preliminary experiment it is quite simple and its scheme is reported in figure 3.18.
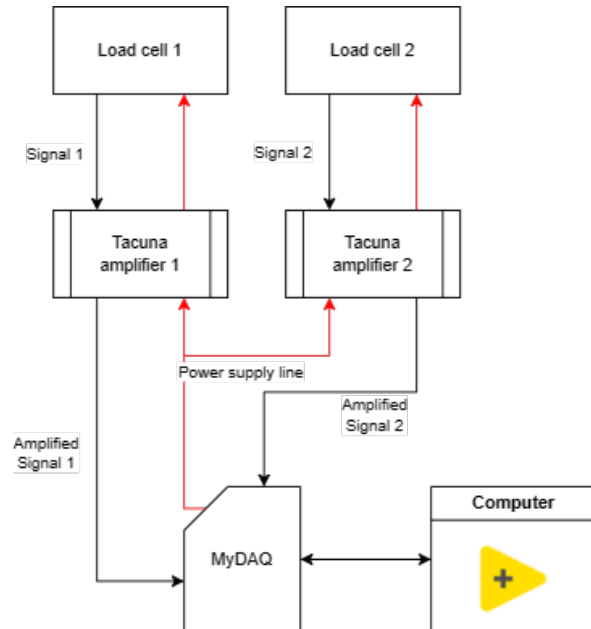

Figure 3.18: Acquisition chain

A computer controls the process by means of a LabVIEW program, the computer only interfaces with the digital acquisition system (in this case the myDAQ[3]), which is responsible for converting the analog signal from the load cell to a digital signal which can be saved easily on the computer. All the chain takes power from the laptop, the DAQ system is provided with different input and output ports but also with a 5V supply port which is optimal for the load cells (figure 3.5).

Figure 3.19: Tacuna amplifier

The load cells are connected to the DAQ system through a couple of tacuna amplifiers, whose model is depicted in figure 3.19. In appendix B some technical specifications about this amplifier and about most of the equipment which was used are reported. One of the most common parameters characterizing the load cells is the sensitivity. The sensitivity is the output signal intensity increment for unit Volt power supply increment, this means that supplying a voltage of 5V will generate a signal of mean intensity equal to 3.5 mV which is too low to be measured. For this reason load cells are always connected to an amplifier which simply multiplies the signal intensity by a constant called gain, usually this constant can be selected among some available values. Obviously increasing the gain constant will increase noise as well so that the signal to noise ratio will be kept constant.

---

[3]DAQ stands for Digital AcQuisition

3.2.2 Load cell calibration

The load cells need to be calibrated to convert the voltage signal into a force, for doing that it is necessary to build a calibration chart which consists in a plot of applied force against measured voltage. The applied force and its direction are well known, in fact a pulley system is used to hang different weights, see figure 3.20, the pulley is designed to have the lowest static friction possible not to pollute the calibration.
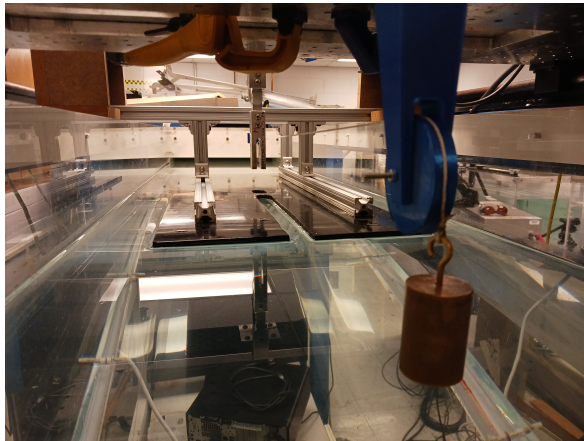

Figure 3.20: Load cell calibration

A sample result of the calibration is shown in figure 3.21, where both the calibration chart (left) and the calibration table (right) are reported. The parameter of interest to extract from this graph is the slope of the line, the offset removal is performed by registering the output value at zero load condition before each acquisition for each load cell and by subtracting it to the corresponding data sets at the end of the acquisition.
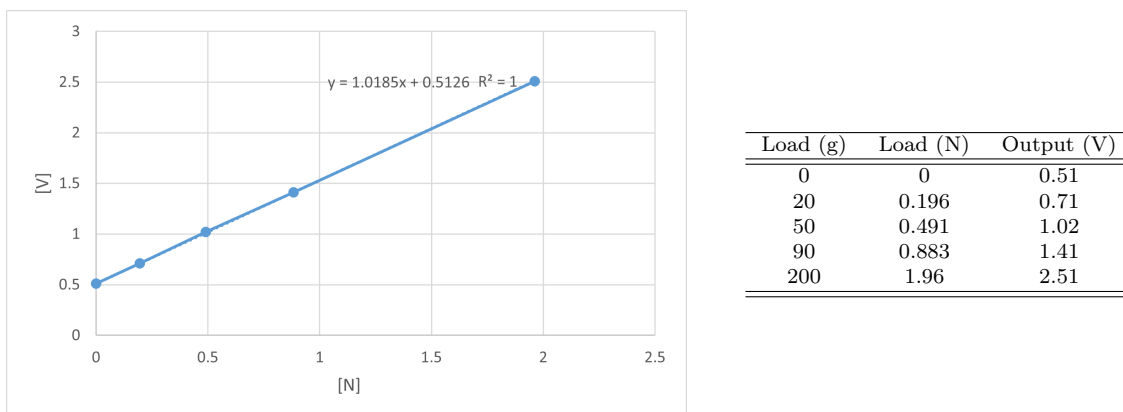

Load (g)	Load (N)	Output (V)
0	0	0.51
20	0.196	0.71
50	0.491	1.02
90	0.883	1.41
200	1.96	2.51

Figure 3.21: Calibration chart

3.2.3 Preliminary results

The data from the load cells are saved in a txt file as in table 3.4, where the first two rows indicate the relative position of the two flags according to the non dimensional parameters Π_x and Π_z, see definition 1.9, the remaining rows contain the time sequence of the load cell's signal for each load cell.

$\Pi_x \downarrow / \Pi_z \rightarrow$	0	0.5	0.75	1	1.5
1.5	1	6	11	16	21
1.75	2	7	12	17	22
2	3	8	13	18	23
2.5	4	9	14	19	24
3.5	5	10	15	20	25

Table 3.3: Preliminary test matrix

The test matrix of the preliminary experiment has 25 different combinations of (Π_x, Π_z) and to each of these combinations is assigned an identifier, i.e. a number, see table 3.3. In this way it is possible to organized the data in an ordered way and to simplify the upload of the data to any post processing programs. The choice of the test matrix was based on previous studies on formation flight like [22], the aim of the project is to find out if the side edge vortex of the front flag can somehow enhance the lift on the rear flag for certain configurations in order to promote higher flapping amplitude, in the same way planes and birds flying in formation experience an overall benefit of the stock in terms of efficiency thanks to induced drag reduction see [26] and [28]. In [26] formation flight for large commercial aircraft has been studied experimentally, planes get more benefits from close formation flight but for large airplanes some minimum spacing has to be guaranteed for sake of safety, therefore it becomes meaningful the study of wake development on long distances behind the plane.

Xd/L	Zd/(L*AR)	
1.5	0	
Time (Sec)	Voltage 1 (V)	Voltage 2 (V)
0	0.906	0.347
0.002	0.949	0.377
0.004	1.003	0.392
0.006	1.022	0.398
0.008	1.018	0.43
0.01	1.025	0.47
0.012	1.018	0.443
0.014	0.977	0.332
0.016	0.936	0.355
0.018	0.889	0.402
⋮	⋮	⋮

Table 3.4: Load cell data format

The results from the preliminary experiment showed a issue in the setup. Figure 3.22 is a plot of the collected data from a test and which was post processed to obtain the force values. The number of collected samples is 62500 for each load cell at the sampling frequency of 500 Hz, for a total acquisition time of 125 s, the acquisition time is required to be this long to get a complete signal since there is no clue at this point of the investigation about the phenomenon of interaction. The respective power spectral densities of the signals are plotted up to the Nyquist frequency, which is 250 Hz. The PSD is computed by performing the fast fourier transform (fft) of the equally time spaced samples, the complex coefficients obtained with the fft are addressed as X_k in equation 3.2, where S_k is the PSD coefficient, f_s is the sampling frequency and N is the number of samples.

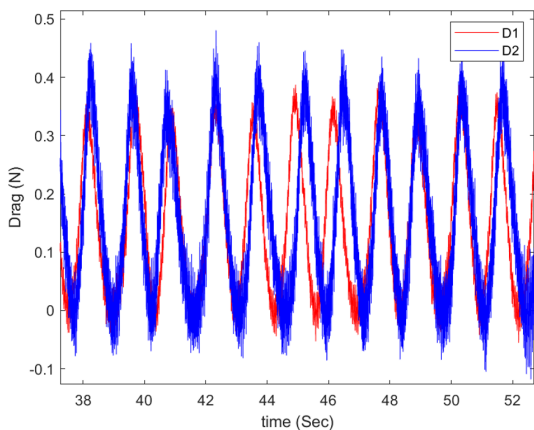$$S(f_k) = \frac{|X_k|^2}{f_s N}, \quad k = 0, 1, 2...N-1 \tag{3.2}$$
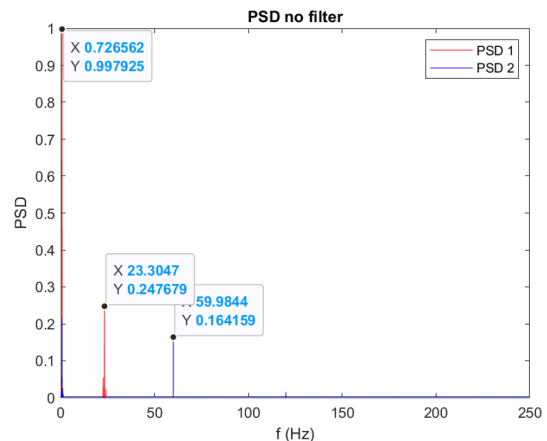

Figure 3.22: Plot of force against time

Figure 3.23: Power spectral density

In figures 3.22 and 3.23 the subscripts 1 and 2 refer to the frontal and rear flag respectively. Focusing on the plot of figure 3.23, three peaks are highlighted:

1. the peak at 0.73 Hz is around the double of what estimated in equation 2.9, in fact the load cell is not able to recognize if the tip of the flag is at the left or right outmost position during the flapping, it only registers a peak on the drag due to the higher dynamic pressure intercepting the flag. Therefore the first and highest peak in the PSD plot corresponds to what is the target of the observation, that is the flapping of the inverted flags;

2. the peak at 60 Hz corresponds to electromagnetic interference of the electric system power supply of the lab, which works at 60 Hz;

3. the peak at 23.3 Hz is due to the vibration of the frontal support, which turns out not to be stiff enough to avoid the flutter instability.

The flutter of the support is visible by naked eye on the frontal support, while the rear support does not experience it because it is immersed in the wake of the frontal one. Different hypotheses were taken into account to identify the cause of the vibration, from vortex induced vibrations (VIVs) to tip effects, but the Strouhal number of the vibration does not match the VIVs' interval in the first case and the tip effects have been excluded because of the symmetry of the support with respect to the flow direction. The only possible explanation is that the support undergoes flutter. By performing a tap test on partial assemblies of the support it was found that the load cell is not stiff enough to avoid flutter, therefore a new design is required to adapt to a new and stiffer load cell.
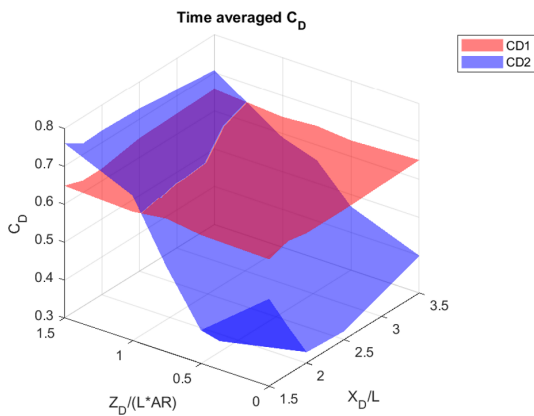

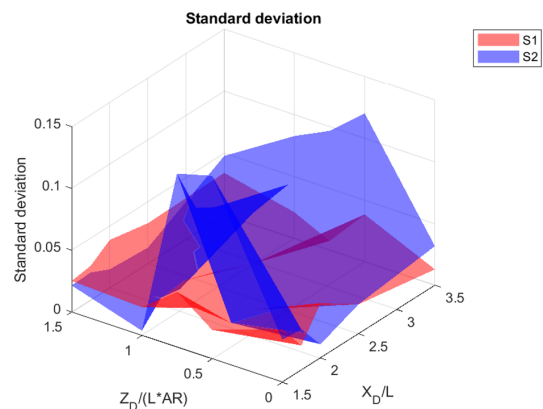Figure 3.24: Time averaged C_d according to 2.28

Figure 3.25: Standard deviation

Figure 3.24 plots the results on all the test matrix in terms of time averaged C_d calculated as described in section 2.3.2. Four different test matrices were collected with the same flags' samples in the same position, the mean over the four test matrices was taken and plotted in figure 3.24 along with the standard deviation of the data, which is plotted in figure 3.25. Thanks to the load cell specifics in appendix B it is possible to calculate the error propagation to the force plotted in figure 3.22.

$$\delta f = \sqrt{\Sigma_i \left(\frac{\partial f}{\partial x_i} \delta x_i \right)^2} \tag{3.3}$$

If a magnitude f depends on different independent variables x_i, it is possible to calculate the error on f by using equation 3.3, where δx_i is the error on the independent variable x_i. By using this method it is possible to estimate that $\delta D = 0.002$ N, which is negligible with respect to the mean value of the signals in figure 3.22, which is about 0.2 N. Therefore it is possible to assess that the drag measurement does not add uncertainty to the final plot of figure 3.24 but that this last result cannot be assumed to be corret because of the flutter of the frontal support.

3.3 Final experiment

This introductory paragraph briefly summarizes the issues which emerged from the preliminary experiment, the new design of the setup aims at solving them.
The new design needs to be adapted to a new and stiffer load cell. Usually using a stiffer element to support the strain gauges means to adopt an higher maximum capacity load cell which results in lower sensibility. Therefore better amplifiers will be used to increase as much as possible the signal to noise ratio. In chapter 2 the magnitudes of interest were highlighted, one of this is the bending energy, to capture it the edge of the flag has to be recorded with a camera. In the preliminary setup the surface waves which arise in the test section generate many reflections which pollute the images for the tracking, so there is the need to build a plate for surface waves' removal.

3.3.1 The final design

Figure 3.26 is a photo of the upper portion of the final setup, while figure 3.27 is the overall view of the CAD model. In the first picture it is possible to observe the frontal support, the surface plate and one of the two new DMD4059 Omega amplifiers. To make it possible to connect the load cells to the amplifiers, some longer wires have been tin welded to the original ones with matching colors, and to reduce electromagnetic interference they have been wrapped in a spiral fashion, as it is possible to see in figure 3.26.
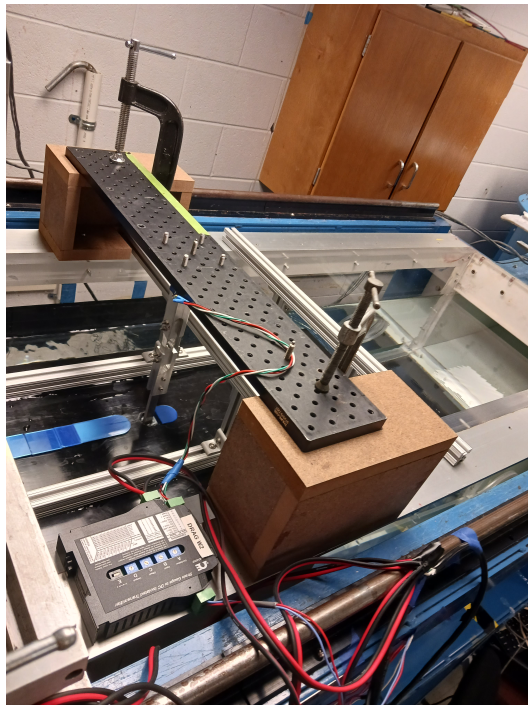

Figure 3.26: Final setup top view

Two new wooden boxes were built to mount both the surface plate and the frontal support plate, moreover two NACA0024 wings envelope the two masts at flags' proximity to reduce the wake pollution by the supports. The wings are made of 3D printed ABF, they have a hollow section within to host the aluminum mast and two holes on one side to screw the two aluminum bars together, moreover a slot is placed close to one end of the wing so that the flag can pass through it. The drawings of the main parts which make up the assembly are shown in appendix A, while the extra parts which are not directly linked with data acquisition, which are the surface plate, the pulley system for calibration and the wings, are briefly described in appendix C. Two light sources are placed at the sides of the test section to uniformly lighten the flags' edges, moreover the wings were painted with a black acrylic paint to reduce light reflections on their surface. Some black sheets were used to avoid the light from spreading in all directions within the test section as in figure 3.28, this trick helps to reduce light reflection and consequent image pollution. At each experiment's execution
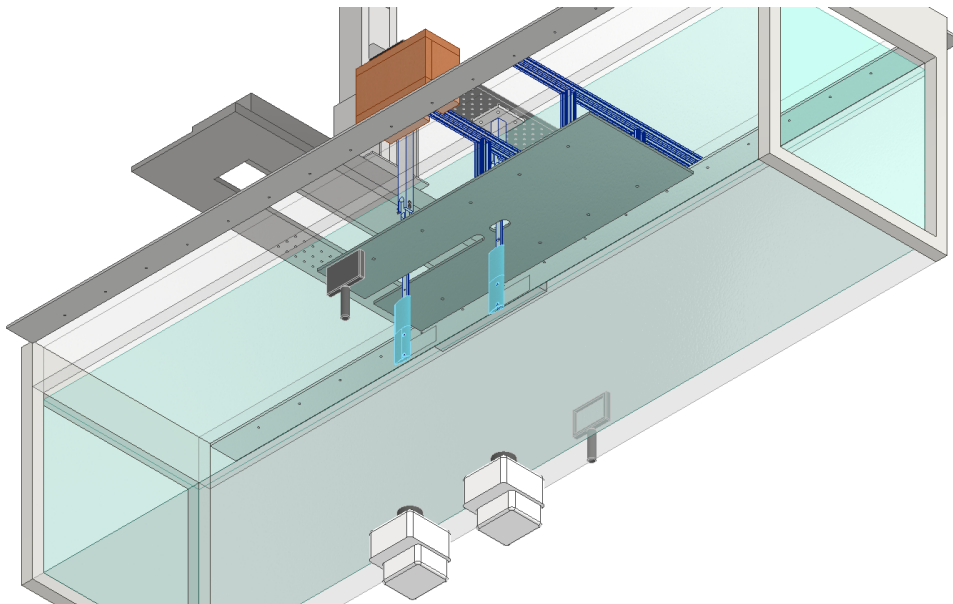
Figure 3.27: Final setup bottom view

the lights of the lab are turned off, and the two lateral LEDs in figure 3.27 are the only sources of light.
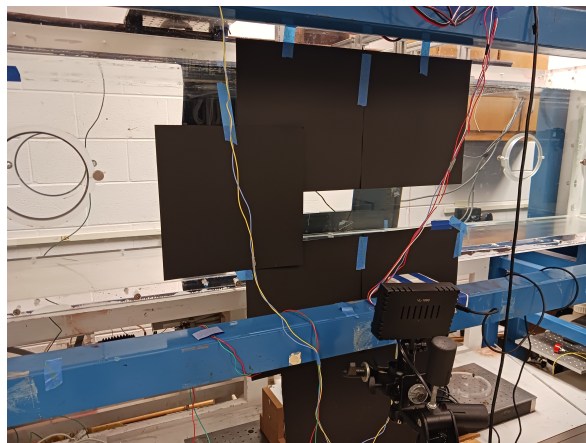

Figure 3.28: Light reflections reduction technique

One factor of uncertainty in the preliminary setup was the relative positioning of the rear flag with respect to the frontal one. The alignment of the flags with the central plane of the test section is guaranteed thanks to the standard assembling procedure, see figure 3.16, while the displacements in the remaining two directions were set with a couple of rulers in the preliminary setup.
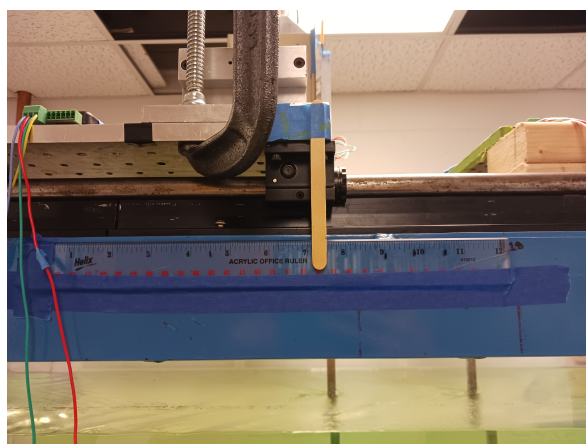

Figure 3.29: Stream wise displacement ruler control

The distance control in the flow direction can be obtained by means of a ruler, as in figure 3.29, since the traverse can be moved manually only. To control the vertical

position of the rear flag, the stepper motor controller (figure 3.3) was used. The LabVIEW code to control the stepper motor through the serial port is described in appendix D, the code makes it possible to move the motor manually but also to switch to a customized auto mode where the acquisition and motor control are performed in sequence, see the appendix for more details.

3.3.2 Acquisition chain

The acquisition chain scheme is depicted in figure 3.30. The load cells' system is not different from the preliminary acquisition chain, apart from the omega amplifiers in place of the tacuna. The omega amplifiers require higher power supply, for this reason they are connected to an external power source. The specifications of these new amplifiers are better described in appendix B. The digital acquisition system which is used in the final acquisition chain is a National Instrument USB-6218 DAQ, in fact the routing system of the myDAQ used in the preliminary acquisition did not allow the synchronized acquisition of the load cell data and the camera images. With the USB-6218 it is possible to turn the DAQ counter output channel on when the analog ports receive a signal. The cameras are two Phantom VEO 640 and they can be configured by using the Phantom Camera Control (PCC) software to receive an external trigger, more information about the specifics of the camera can be found in appendix B. The computer can communicate with the cameras by means of an ethernet cable and a switch, in this way it is possible to control up to four different cameras at the same time with the PCC software. In the experiment the two cameras are placed below the test section, as shown in figure 3.27 in order to record the edge of the two flags. Furthermore the cameras are both equipped with a nikon nikkor lens 50mm f/1.8D, see figure B.5. The last part of the acquisition system consists in the stepper motors control, which is mediated by the VP9000, figure 3.3, through the serial interface RS-232.
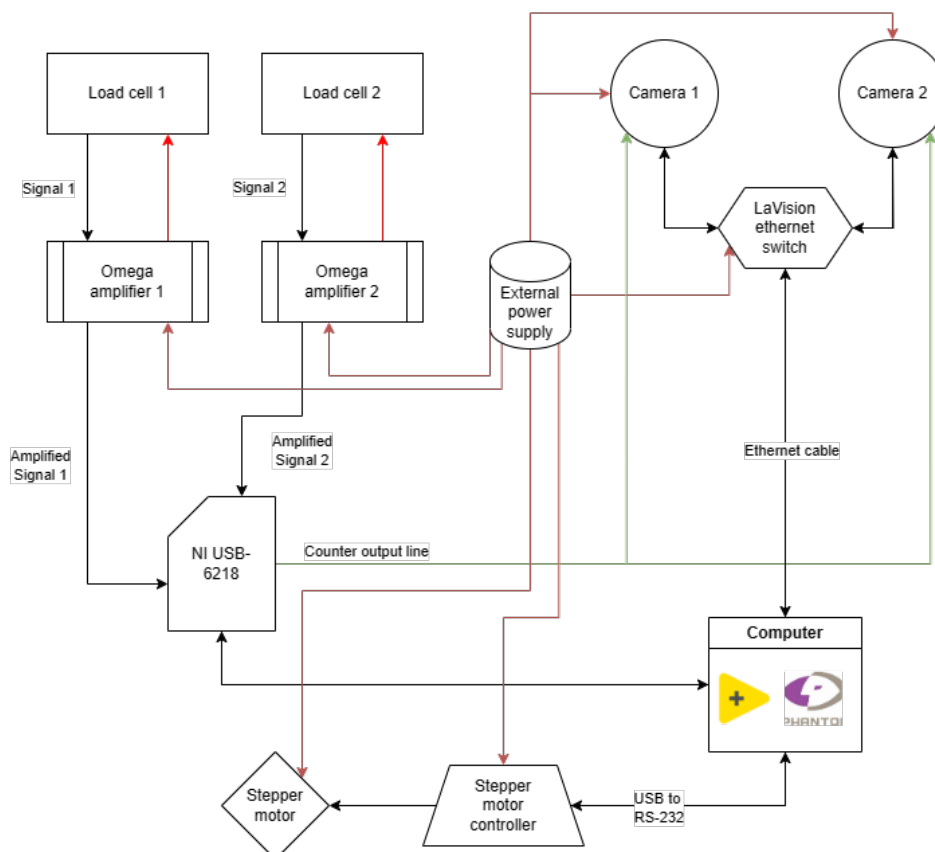

Figure 3.30: Acquisition chain

3.3.3 Experimental conditions

To be sure of the repeatability of the results, the final experiment is conducted on 3 sample couples of flags which have been cut from different mylar sheets, all having the same thickness of 0.01". To be more specific, the first couple was cut from the sheet number 1, the second couple from the sheet number 2 and the third couple from the sheet number 3. Furthermore sample 'frontal' is the frontal flag, while sample 'rear' is the rear one. The flags were all cut in the natural bending direction of the sheets[4] not to have new degrees of freedom and to avoid motion constraints on the flags dynamics. The relative positioning of the residual curvatures was the same for all the three couples, that is the orientation of the residual curvature of the frontal flag with respect to the residual curvature of the rear one is the same among all the three couples.

All the samples were tested individually in the water tunnel to identify the upsweep critical velocities. It has been noticed that there were consistent differences in the stability of the different flags.

Sample	straight to flap upsweep (Hz)	flap to deflected upsweep (Hz)
1 frontal	185	250
1 rear	185	255
2 frontal	215	305
2 rear	200	275
3 frontal	200	275
3 rear	185	255

Table 3.5: Samples upsweep velocities

Table 3.5 reports the upsweep critical velocities for all the samples in terms of frequency command on the water tunnel engine. In chapter 2 the water tunnel facility has been described, it was pointed out that to control the water flow the adjustable parameter is the frequency of the fan which moves the water, since the devices for measuring the velocity directly were not set up at the moment of the experiment the frequency parameter was saved, by taking care that the water level at zero flow condition was the same for all the measurements and for all the experiments conducted. In all the tests, the water temperature was measured at zero flow conditions and it was found to fall in the range $23^oC < T < 24.5^oC$ always, so the density of the water was assumed to be constant among all the cases and all the experiments. By going back to table 3.5, it is clear that the test velocity cannot be chosen randomly, but it has to fall at the middle of the intersection of the flapping ranges of all the samples, in order to avoid other dynamic modes other than the flapping mode. It becomes obvious now that even by performing this choice on the velocity the flags will present different behaviours in terms of amplitude and flapping frequency, but a mean of the results on each sample will be considered for the final conclusions.

The final frequency at which the experiment will be performed for all the samples was selected to be 232 Hz, to calculate the corresponding water velocity a simple PIV is used.

In the next part the parameters which define the experiment are calculated. The flag design and its material properties are known, so only the flow conditions have to be defined. Velocity at experimental conditions and temperature at zero flow are measured, for the first magnitude PIV will be used, while a simple thermometer is used to measure the temperature.

PIV

Since the water velocity is measured in the empty test section, the flow can be assumed to be steady and uniform, so the observation direction does not matter. The water is full of hollow glass particles and a small laser is enough for making them visible to the

---

[4]Thin plastic sheets are produced my flattening the plastic between heated elements, the cooling process inevitably produces some residual curvature in the sheets.

Figure 3.31: PIV setup

camera. A laser sheet was created by using the laser optics and the camera was placed below the test section to record the images. A picture of the PIV setup is reported in figure 3.31, the laser is placed on a tripod on the right side of the image, the laser is mounted on a optics table together with two divergent lens placed in sequence to create the sheet. Furthermore the laser sheet was aligned with the frontal flag edge so to have a reference for the PIV calibration.
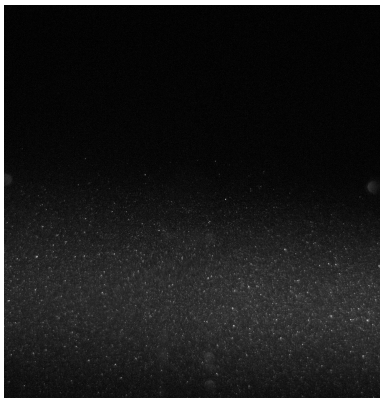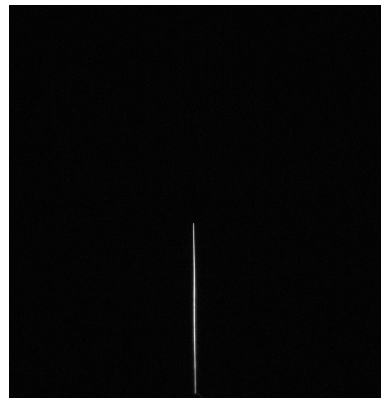

Figure 3.32: PIV sample image

Figure 3.33: PIV calibration image

Figure 3.32 is a PIV sample image, the laser sheet is not perfectly aligned with the focal plane of the camera, so the particles are visible only in the lower portion of the image. Figure 3.33 is taken at the exact same location of figure 3.32 but at zero flow condition and with the flag in place. Since the flag length is known, it is easy to calibrate in this way.
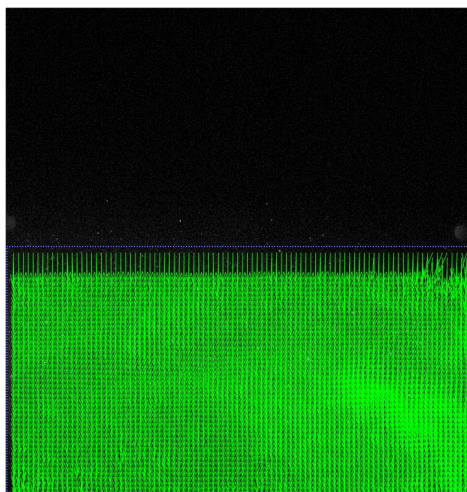

Figure 3.34: PIV result

Figure 3.34 reports the results of the PIV in the selected region of interest (ROI), the mean value of the velocity component in the vertical direction is 0.318 m/s after the calibration has been applied, while the horizontal component is about 0.006 m/s, so it is possible to assume that the camera is well aligned with the flow direction. For sake of simplicity the velocity will be rounded to 0.32 m/s. Because of the steady and uniform nature of the flow only two frames are sufficient to calculate the velocity by cross correlating them.

Main parameters

A long probe digital thermometer was used to reach the middle of the test section. As mentioned at the beginning of this section the temperature was always comprised in the range $23^oC < T < 24.5^oC$, therefore the water density has been assumed to be $997.4 \ kg/m^3$, which is the water density at 23.7^oC at ambient pressure. The change in pressure per unit Celsius degree is low with respect to the density value itself, so it is possible to assume equal density among all the cases of the experiment.

Magnitude	Definition	Value	Units
Velocity	U	0.32	m/s
Water density	ρ_f	997.4	kg/m^3
Water dynamic viscosity	ν	9.18E-4	m^2/s
Reynolds number	$Re = \frac{UL}{\nu}$	26562	-
Bending stiffness	$B = \frac{Eh^3}{12(1-\nu^2)}$	0.0104	Nm
Non-dimensional bending stiffness	$K_B = \frac{B}{\rho_f U^2 L^3}$	0.23	-
Mass ratio	$M_S = \frac{\rho_s h}{\rho_f L}$	4.61E-3	-
Reduced velocity	$U^* = \sqrt{\frac{1}{K_B}}$	4.35	-

Table 3.6: Main parameters defining the experiment

Finally table 3.6 summarizes the main parameters characterizing the experiment. Along with their values also their definition is written down, the absence of units of measurement signifies that the parameter is non dimensional. All of the elements appearing in table 3.6 are defined and explained in section 1.4. The value of the non dimensional bending stiffness is 0.23, and as expected is at the center of the range where the flapping mode occurs, that is $0.1 < K_B < 0.3$.

Chapter 4

Data processing and results

In this chapter the raw data from the final experiment and its post processing will be described. It is remarked that there are two types of data which was collected, the load cells' data and the cameras' images, therefore a part of this chapter will be dedicated to each type. A final section is reserved for the characterization of the samples and the presentation of the most important results.

4.1 Load cell data

In section 3.2, the load cell data format was described in table 3.4, basically the first two rows contain information about the relative positioning of the flags, and the remaining rows describe the time sequence of the two signals. Specifically the first column contains the time coordinate, while the second and the third ones contain the signal from the frontal load cell and from the rear one respectively. In the final experiment the format is the same and the data is saved in a txt file as well, but only in the fast acquisition mode.

Xd/L	Zd/(L*AR)	
1.667	0	
Voltage 1 (V)	Voltage 2 (V)	Trigger signal (V)
0.0551	0.0844	0.134
0.0486	0.0796	0.134
0.0474	0.0822	0.1342
0.0459	0.0909	0.1344
0.0456	0.0697	0.1344
0.0474	0.071	0.134
0.0464	0.0689	0.1344
0.0468	0.0654	0.1345
0.0417	0.0613	0.1339
0.042	0.0668	0.1342
0.041	0.0643	0.1344
0.0422	0.0704	0.1344
0.0451	0.0733	0.1344
0.0448	0.0775	0.1337
0.0418	0.0812	0.1344
0.0563	0.0845	0.1344
0.0459	0.0844	0.1345
0.0477	0.0845	0.1345
0.0474	0.0827	0.134
0.0468	0.0812	0.1342
0.0451	0.0758	0.1344
0.0415	0.0712	0.1339
0.0423	0.0648	0.1335
0.0426	0.0653	0.1344
0.0412	0.0658	0.134
0.04	0.0673	4.9376
0.0395	0.0656	4.9346
⋮	⋮	⋮

Table 4.1: Final load cell data format

The acquisition modes are two, they are described in appendix D, in the section dedicated to the software used to control the acquisition, in fact for each acquisition type a different code needs to be used. In the fast acquisition mode only load cells' data is saved, the cameras are not connected, this trick makes it easier to collect the data all over the test matrix in the shortest time span possible since the stepper motor

for the flags' relative positioning moves automatically during the experiment.

Instead the synchronized acquisition mode is a slow process because the flags are positioned manually with the help of the VP9000 controller, the cameras are configured and positioned by consequence in a trial and error process, moreover at the end of the acquisition the collected images have to be saved manually. In this last acquisition mode, another column is added to the txt file for saving the counter signal. Basically, the cameras have been configured to capture an image every time their trigger input sees a falling edge in the voltage signal, which in this case is given by the counter output of the DAQ. Saving the trigger signal is important to verify the consistency of the data. A sample of raw data is reported in table 4.1, the time coordinate is not saved anymore since it can be generated by knowing that the samples are equally spaced in time, by knowing the sampling frequency and by setting the first sample at the zero time coordinate. At the end of table 4.1 it is even possible to notice the first rising edge of the signal. In the fast acquisition mode the sampling frequency is set at 500 Hz and the number of samples to 75000, for a total acquisition time of 150 seconds. In the synchronized acquisition the sampling frequency is 1000 Hz, and the number of samples is set to 30000, for a total acquisition time of 30 seconds.

4.1.1 The test matrix

$\Pi_x \downarrow / \Pi_z \rightarrow$	0	0.25	0.5	0.75	1	1.25	1.5	1.75	2	2.25	2.5
1.67	1	2	3	4	5	6	7	8	9	10	11
2	12	13	14	15	16	17	18	19	20	21	22
2.5	23	24	25	26	27	28	29	30	31	32	33
3	34	35	36	37	38	39	40	41	42	43	44
3.5	45	46	47	48	49	50	51	52	53	54	55

Table 4.2: Final test matrix

The final test matrix is reported in table 4.2, it is possible to notice two relevant aspects with respect to the preliminary matrix, the number of cases is more than doubled, and the Π_z range is consistently larger. The results from the preliminary experiment have not been discussed because of their high uncertainty, but the final test matrix was written starting from them. The reason behind the first aspect which has been mentioned is to have more resolution in the space domain with respect to the preliminary experiment, instead the second aspect is to explore what happens when $\Pi_z > 1.5$, because the trend of C_{D2} was still increasing in figure 3.24, but a plateau was expected.

4.1.2 Post processing

The post processing of both the load cell data and the camera frames are carried out in MATLAB. From the load cell data it is possible to extract several parameters which characterize the flag dynamics, but first it is necessary to remove the noise from the signal.

The amplifiers offset and span were set to get the highest signal to noise ratio possible. Here a brief description of the diagram in figure 4.1 follows, where the subscript 1 refers to the signal from the frontal load cell and subscript 2 to the signal from the rear load cell. The voltage peaks occur when the flag is at maximum deflection, in this position the flag will experience the highest drag and by consequence the highest strain on the load cell will happen. When the flag is aligned with the undisturbed velocity field a valley can be observed in the signal. As mentioned in appendix D in the fast acquisition section, the offset from the load cells is registered at zero flow conditions and subtracted from the experienced signal at the end of the acquisition, therefore the voltage signal is expected to be 0 V at the valleys, instead something different is observed. To explain this difference remember that the flags are clamped each on a support, which has its own drag in the water flow, the load cells measure this added resistance and sum it to the final signal as a constant. The offset of
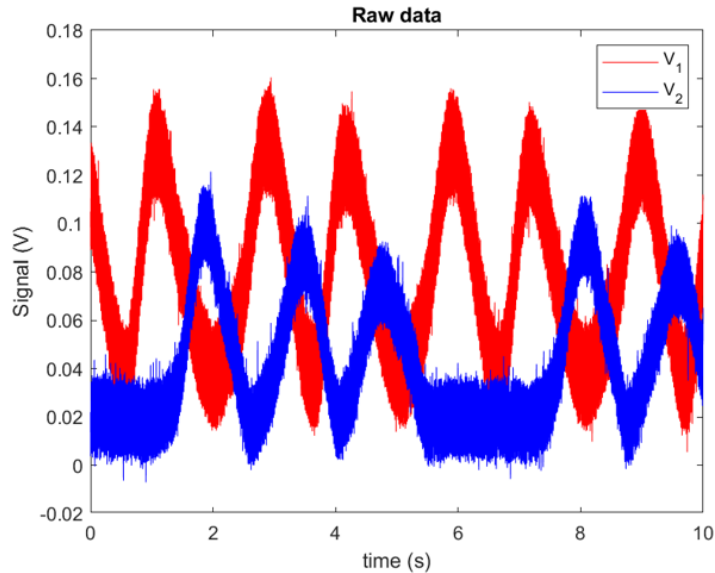
Figure 4.1: Load cells' raw data

the frontal flag, red signal in figure 4.1 is higher in this case because most of the rear support is immersed in the frontal support wake. For configurations with high Π_z the offset of the blue signal will be higher than the offset of the red signal. To remove the added drag from the supports, the data from the load cells were taken for all the cases on the test matrix in absence of flags, but this method resulted in high uncertainty in the offset removal. The only reason behind this uncertainty could be the load cell resolution, in fact its maximum capacity is 1 kg but in this case it would need to measure few grams. Therefore an artificial offset removal will be performed and then compared with the energy analysis from the cameras to be confirmed valid.
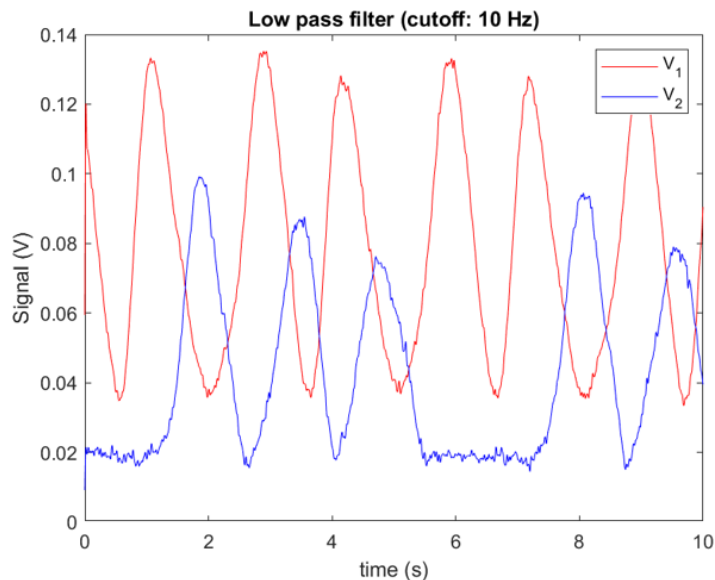
Figure 4.2: Low pass filter application

The result of the application of a lowpass filter through the MATLAB function 'lowpass' at 10 Hz cutoff frequency[1] is displayed in figure 4.2. The power spectral density of the raw data is similar to the one in figure 3.23, but there is no peak at 23 Hz because the supports are stable and flutter does not verify.

The next step is the application of a Savitzky Golay smoothing, in this case a 4th order polynomial was used to fit in the least square sense relatively long subsets of the filtered signals of figure 4.2, the result of the smoothing is shown in figure 4.3. This phase is essential to the next step of the post processing, that is the offset removal. As previously discussed, by considering the physics of the flapping flag and the method used for data acquisition, the voltage signal valleys should locate close to 0 V.

---

[1]For low-pass filters, the cutoff frequency is defined as the frequency at which the gain drops by -3dB
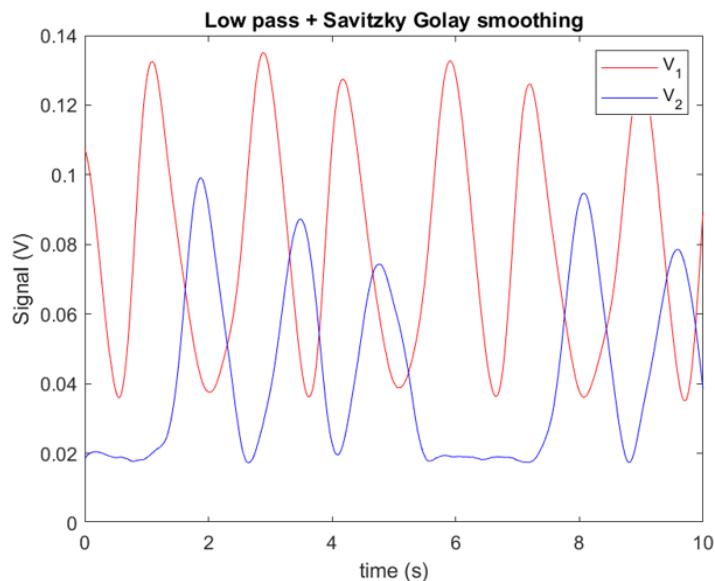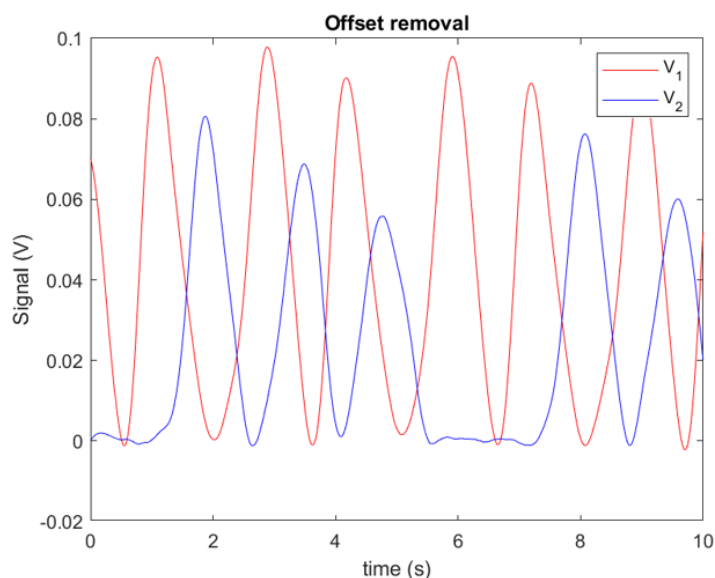
Figure 4.3: Savitzky Golay smoothing

Figure 4.4: Offset removal

By mirroring the signal along the horizontal axis and by using the MATLAB function 'findpeaks' with adaptable input parameters taken from the PSD of the specific signal being analyzed, all the valleys of the signals can be found. To the signals the mean of all the valleys is subtracted to obtain the final result of figure 4.4. At this point the load cells' calibration can be applied to change the voltage values to the corresponding newton values, the highest peaks register about 0.4 N, which is approximately equal to 40 gF[2], this aspect makes it clear how important getting the highest signal to noise ratio is when only 4% of the load cell capacity (1 kg) is used, that is why the Omega amplifier was chosen, see figure B.3. The random error on the load cells data is comparable to the one from the preliminary experiment and it is negligible with respect to the mean drag value.

Starting from the post-processed signals of figure 4.4, three final parameters are extracted for each case on the test matrix: the time averaged drag coefficient defined in equation 2.28, the flapping frequency of each flag, the phase delay between the frontal and the rear flag.

Time averaged drag coefficient

Since all the elements in the C_D definition of equation 2.25 are constant in time apart from the drag, it is possible to take them out of the integral of equation 2.28, and integrate the drag signal directly, then multiplying the result of the integration by the

---

[2]Grams force

constants. Instead of performing the integration on one single period, it was decided to calculate the mean integral over the whole acquisition period, because in some cases it is difficult to recognize a periodic pattern, even with the help of the power spectral density. The final results of the time averaged drag coefficient are plotted for the whole test matrix in the same manner of graph 3.24. For each flag couple of table 3.5 two independent tests were conducted to check for repeatability of the experiment on the single couples, then the results from the different couples are compared one another to highlight eventual differences among the samples. Finally the mean over all the test cases is calculated along with their standard deviation.

Flapping frequency

The second parameter which gives important details about the dynamics of the flapping flags is the flapping frequency, this magnitude is selected through a MATLAB algorithm, therefore even if for some specific cases it can seem hard to find a periodic tendency in the signal, the algorithm will do it in the same way for all the cases. The code calculates the power spectral density of the signals as in equation 3.2 and it takes half the frequency corresponding to the highest peak in the spectrum to be the flapping frequency.
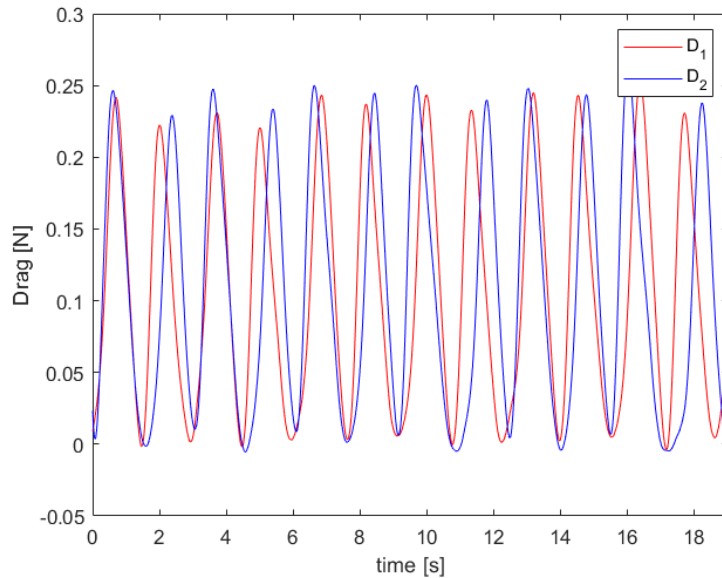

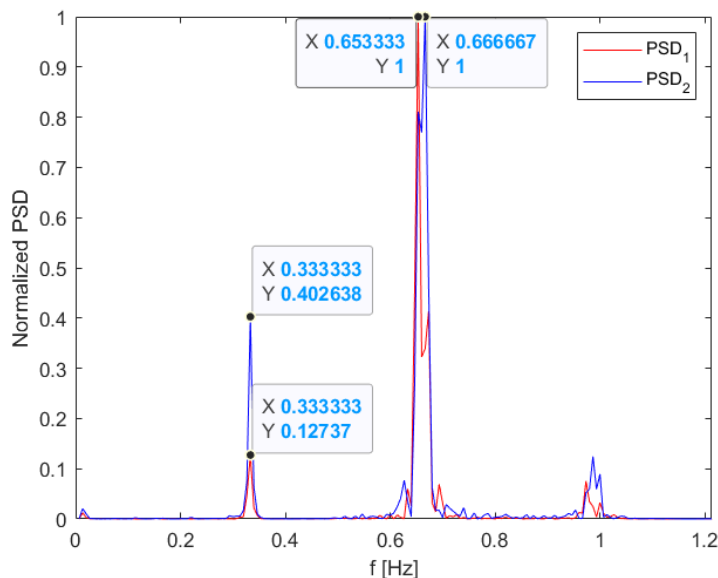Figure 4.5: Drag versus time

Figure 4.6: Power spectral density

Figure 4.5 is a plot of part of the signal registered during the first test on the third sample of flags in correspondence of case number 20 of the test matrix 4.2 after all the post processing mentioned previously in this section, instead figure 4.6 is the plot of the normalized power spectral density of the same signal for the frequency range that goes from $0\,Hz < f < 1.2\,Hz$, which is the range of interest. It is possible to observe two main peaks for each signal, and the highest occurs at double the frequency of the lowest, this is not a coincidence but simply a result of the imperfect alignment of the flag in the flow direction. The second and lowest peak between the two is the actual flapping frequency of the flags.

Phase shift

The last parameter which can be calculated from the load cell data is the phase shift between the frontal flag and the rear one. In this case the algorithm exploits the MATLAB function 'xcorr', it can return both the correlation coefficient between two data sets and the corresponding lag for each correlation coefficient. In this specific application the phase lag of the rear flag with respect to the frontal one has been evaluated for all the cases. An example of the result of the 'xcorr' function applied to the two signals of figure 4.5 is plotted in figure 4.7, where the y axis is the correlation coefficient value and the x axis is the phase shift in seconds, indicated as lag.
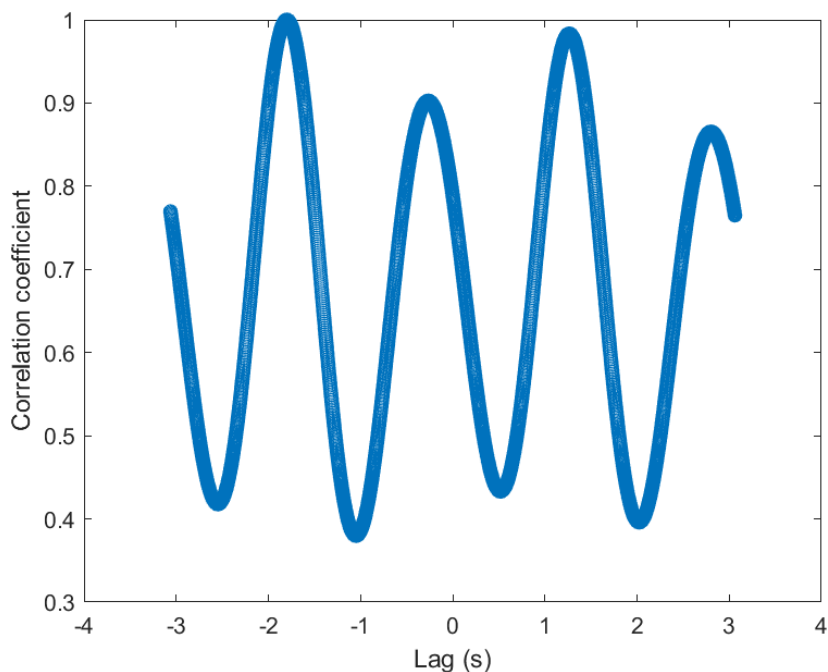

Figure 4.7: Correlation coefficient: sample 3, case 20 of table 4.2

The tendency of the correlation coefficient is to present peaks and valleys every half of the flags' flapping period, because of the periodicity of the drag signal in this specific case. It is not possible to understand which is the right lag without more data, but it is possible to select the closest peak to the zero phase lag as a selective criterion. Finally the time lag can be converted into a percentage of the flapping period of the frontal flag if divided by this last. In this way it is possible to compare the final results with [15]. This can be done only if the flapping periods of the two flags are very similar or identical.

4.2 Load cell and camera: synchronized data

This part of chapter 4 is dedicated to the description and the post processing of the data collected synchronously from the load cells and from the cameras. The algorithm for load cell data processing is the same described in the preceding section, the only difference is the data format, which has already been described previously as well, and the number of analysed cases on the test matrix, which was reduced to 17 on 55

because the acquisition procedure per single case takes much more time than the fast acquisition, for more details see appendix D.

4.2.1 The test matrix

$\Pi_x \downarrow / \Pi_z \rightarrow$	0	0.25	0.5	0.75	1	1.25	1.5	1.75	2	2.25	2.5
1.67	1	2	3	4	5						11
2		13							20		
2.5									31		
3			36	37	38				42		44
3.5	45								53		55

Table 4.3: Final test matrix

The 17 cases which were studied in the experiment are reported in table 4.3, they are the same for all of the three samples. The choice of the cases was not executed randomly, first all the corners were selected, then some of the cases which presented higher standard deviation of the fast acquisition data were picked, along with some cases at the center of the test matrix.

For each of the 17 cases of table 4.3 the images from the cameras were saved in two folders for the frontal and rear flag respectively, the acquisition is controlled through both the LabVIEW software described in appendix D and the phantom camera control 3.7 software, specifically on this last the frame rate, the number of images to be saved in the camera RAM, the image resolution and many more settings can be set for each camera. All the camera settings were kept constant during the different acquisitions, apart from the image resolution of the rear camera, which was modified in function of the varying distance of the flag's edge from the camera optics. After activating the external trigger, the acquisition can be led by means of the LabVIEW software.
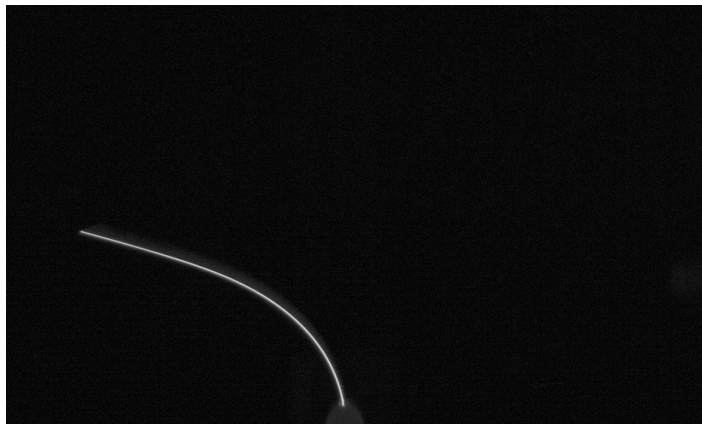

Figure 4.8: Sample image for flag tracking

A sample image from the camera is depicted in figure 4.8, the bottom edge of the flag has been painted with a white waterproof paint to increase the contrast with the background, which is the bottom of the surface plate of figure C.3. Some details which can be noticed in image 4.8 are the presence of the wing which encloses the aluminum support at the bottom of the image and the fact that there was no alignment procedure for the camera, in fact some parallax errors occur, but they can be neglected as long as the focal plane of the camera coincides with the flag's edge plane.

4.2.2 Post processing of the images

The whole scheme of images' post processing is represented in figure 4.9, it describes the sequence of MATLAB functions used to get the final result along with the parameters specified in each of them.

The raw images are in a 8 bit grey scale, since the white edge has an high contrast with the background and the aim of the post processing is to isolate its points, the first
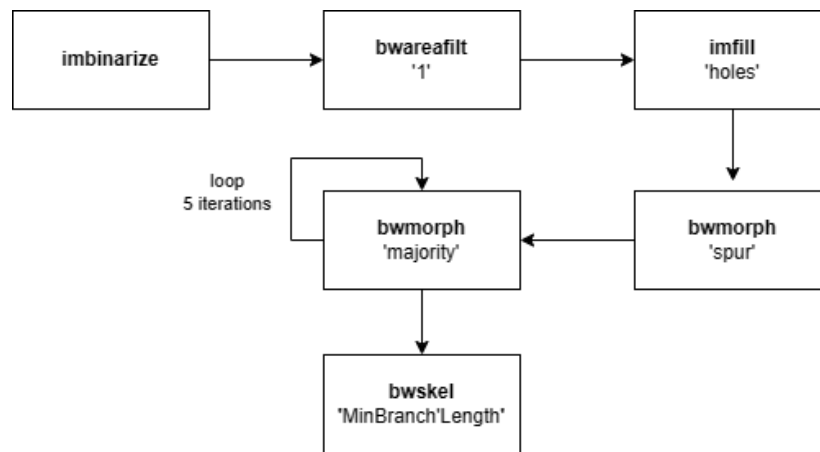
Figure 4.9: Processing scheme of the images on MATLAB

obvious step is to filter the image by intensity converting it to a binary image. In other words the pixels whose intensity is higher then a specified threshold will be converted into ones, while the remaining ones will be set to zeros, to this purpose the MATLAB function 'imbinarize' can be used.

Since there are reflections both from upper sections of the flag and from the environment, some points not belonging to the edge will be picked up by the imbinarize filter, therefore the next step is to take the object with the highest area in the picture, which is the flag's edge by using the 'bwareafilt' MATLAB function with input parameter 1, which specifies to consider only the object with the biggest area in the image.

The 'imfill' function with input parameter 'holes' will fill all the holes within the edge of the flag, they could occur if some particles dispersed in the water pass between the camera and the flag obscuring in this way the edge. Instead the function 'bwmorph' can execute different operations on binary images, in this case spurs' removal is selected by setting the parameter 'spur'. A 5 iterations loop of application of the same function 'bwmorph' but with a different parameter, which is 'majority', is used to produce smoother boundaries on the flag's edge. Basically this last function turns into 1 the zero pixels whose closest 8 neighbouring pixels have a majority of pixels equal to 1. The result of the application of the aforementioned functions in sequence to the raw image of figure 4.8 produces the result of figure 4.10.

Figure 4.10: Result of the application of the first 5 functions of scheme 4.9 to figure 4.8

The last function is called 'bwskel', it reduces all objects in the 2-D binary image to 1-pixel wide lines, without changing the essential structure of the image. The specified parameter 'MinBranchLength' helps to take into account only branches longer than a specified threshold, this trick improves the final result by removing eventual branches on the main one. The final result of the whole algorithm is shown in figure 4.11.

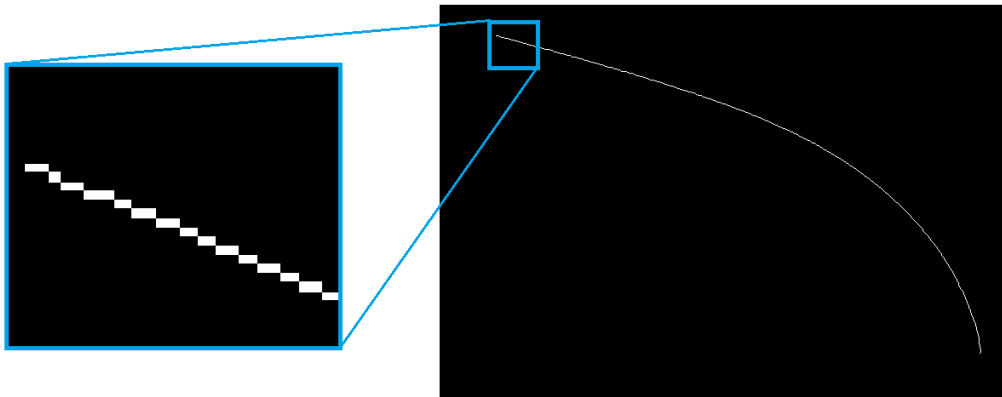The result of figure 4.11 is the start to get the flag's coordinate to finally evaluate

Figure 4.11: Final result of the image processing algorithm

the non-dimensional strain bending energy defined in equation 2.26.

This aspect is arbitrary, but all the frames are rotated in order to have the trailing clamped edge at the left side of the image and the free leading edge on the right side, the coordinate system used for flag's edge shape evaluation is the same defined in figure 2.18. The next task is to interpolate the points in figure 4.11 to obtain a smooth edge, in fact right now the points are placed in a stair fashion because the edge is identified by a 1-pixel or 2-pixels wide line. The interpolation will be performed over the curvilinear coordinate, this expedient produces an excellent result but has to be executed on both the x and y coordinates, remember the reference scheme of figure 2.18.
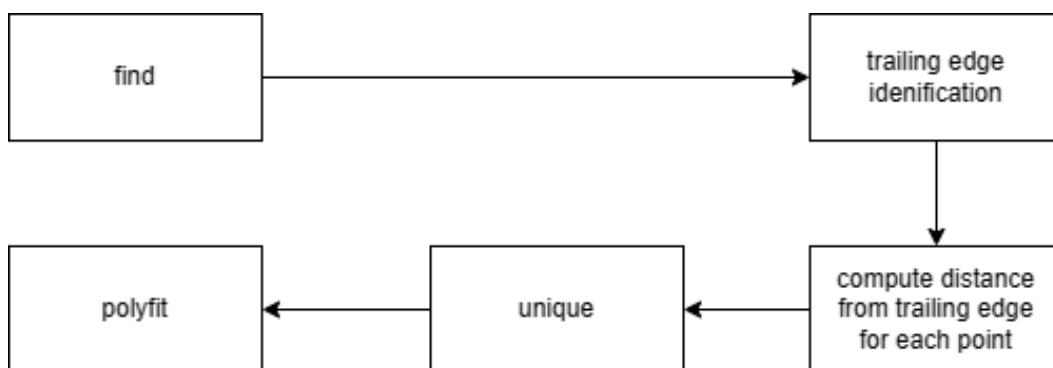
Figure 4.12: Flag coordinates interpolation scheme

First the coordinates of the points in figure 4.11 are found in the image reference frame thanks to the MATLAB function 'find'. Since the flag does not perform large amplitude flapping in water, the trailing edge can be identified by picking up the point with the lowest x coordinate in the image reference frame. The next step is ordering the points along the curvilinear coordinate, and for the same reason of the previous point, it is possible to order them by increasing distance from the trailing edge by using the 'unique' MATLAB function. This function can return the index of a vector's elements in ascending or descending order by removing elements which repeat more than one time. Next the indexing obtained with the 'unique' function is applied to the x and y coordinates vector to obtain the correct sequence of point to use in the interpolation procedure. At this point it is necessary to estimate the curvilinear coordinate of each point, this task can be easily completed by computing the distances between each neighbouring couples of points in the ordered x and y coordinates vector and summing them up to the location where the curvilinear coordinate wants to be evaluated.

At this point three vectors have been extracted from the image: the x coordinate vector, the y coordinate vector and the curvilinear coordinate s vector. They are
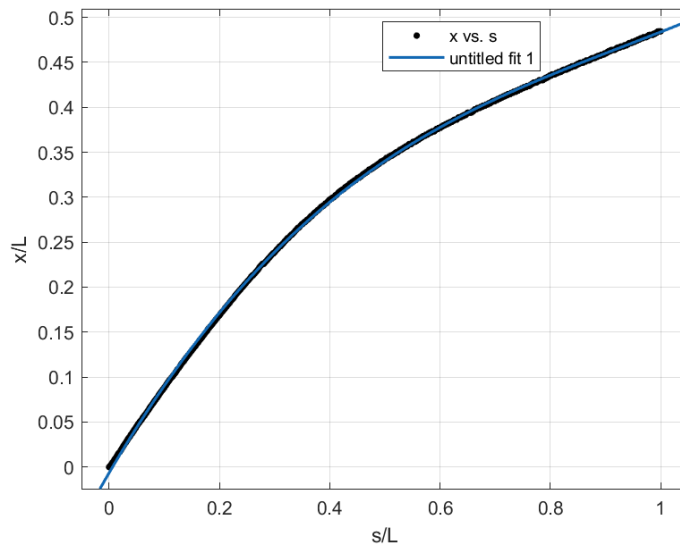
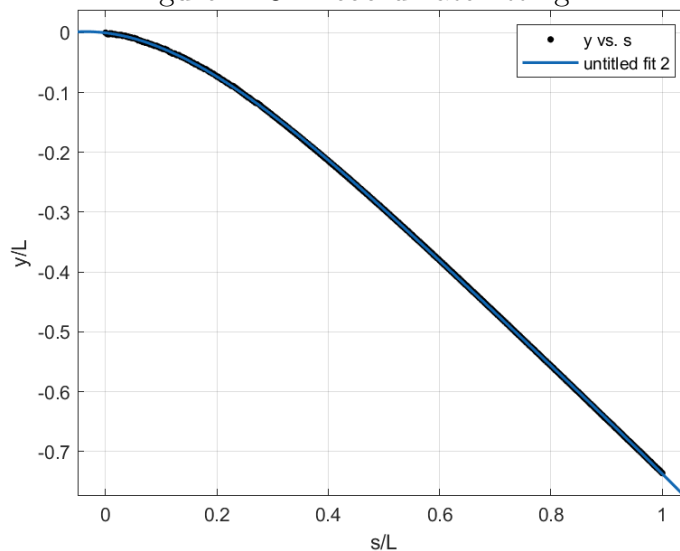Figure 4.13: x coordinate fitting

Figure 4.14: y coordinate fitting

ordered by increasing value of the s coordinate, they have the same number of points and each ordered triplet (x,y,s) represent the position of a tracked flag's edge point. Now it is possible to move on with the interpolation.

An example of the x and y coordinates fittings is presented in figures 4.13 and 4.14 respectively. Since the image resolution and consequently flag's dimensions can change from an acquisition to another, all the coordinates were normalized with respect to the flag length. In figures 4.13 and 4.14 the black dots represent the tracked points, while the blue line is the result of a polynomial function fitting in the least square sense. The x coordinate fitting is performed through a cubic polynomial, while the y coordinate uses a 4th order polynomial fitting, the choice of the fitting functions was a trial and error process by means of the MATLAB curve fitting tool.

The result of the interpolation is plotted in figure 4.15, this is the final reconstruction of the flag's edge of figure 4.8, the curve now is smooth and everything is known about it. It can be noticed that in the fitting result of figure 4.14 the values are negative, this is due to the image rotation and curve translation performed during the processing, the reference frame can be rotated to agree with the tracking result, in any case this is not relevant since the aim of this procedure is to calculate the local curvature of the flag and it can be done in any reference frames.

Curvature

To calculate the non dimensional bending energy, first it is necessary to get the local curvature along the curvilinear coordinate. The formal definition of the curvature along a line is defined as in equation 2.27 and its unit of measurement is $(1/m)$. In
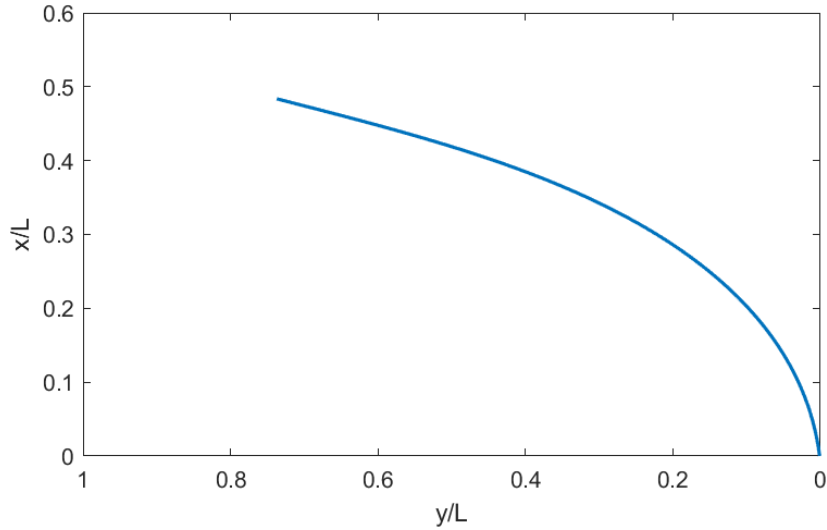
65

Figure 4.15: Fitting result

this case the curvilinear coordinate is normalized by the flag length $s = \frac{s}{L}$, therefore it is non dimensional and by consequence the local curvature will be non dimensional as well $k(s) = K(s)L$.

$$k(s) = \sqrt{\left(\frac{d(cos(atan(\frac{y'(s)}{x'(s)})))}{ds}\right)^2 + \left(\frac{d(sen(atan(\frac{y'(s)}{x'(s)})))}{ds}\right)^2} \qquad (4.1)$$

Equation 4.1 can be obtained in the reference frame of figure 2.18 starting from the definition 2.27, the formula was proven to be right by using the parametric definition of a circle of arbitrary radius and checking the final curvature to be the inverse of the radius at each position on the circumference.

Thanks to the interpolation it is possible to evaluate the expression analytically by placing the derivatives $x'(s)$ and $y'(s)$ in the expression and then evaluating $k(s)$ at some specific locations s.

The curvature distribution along the curvilinear coordinate of the reconstructed edge in graph 4.15 is plotted in figure 4.16. The curvature distribution is physically consistent, it is possible to compare this result to the boundary conditions of the inverted flag as defined in [32]. It is compact to write the conditions in vector notation, in equation 4.2, the first element of the list defines the coordinates' vector, the second and third elements describe the conditions at the clamped trailing edge where θ_i is the slope of the flag at the trailing edge in the x-y reference frame, while the last two equations define the conditions at the free leading edge.

$$\begin{aligned}
\mathbf{z} &= (x, y) \\
\mathbf{z}(s = 0) &= \mathbf{z}_0 \\
\tfrac{d\mathbf{z}}{ds}(s = 0) &= (-cos\theta_i, -sen\theta_i) \\
\tfrac{d^2\mathbf{z}}{ds^2}(s = 1) &= (0, 0) \\
\tfrac{d^3\mathbf{z}}{ds^3}(s = 1) &= (0, 0)
\end{aligned} \qquad (4.2)$$

In the curvature distribution plot of figure 4.16, the condition of zero second derivative at the leading edge coincides with the zero curvature value, not all the frames satisfy this condition probably due to some imperfections within the edge detection procedure, but the curvature value at the leading edge is always very close to zero. Instead on the other side the curvature has its highest value in correspondence of the clamp.

The final part of the non dimensional bending energy computation is a simple integration, it is not performed analytically because of the computational cost and time demand of the operation, instead a finite number of points is saved from the analytical result plotted in figure 4.16 and a numerical integration by means of trapezoids is executed. Despite a lower accuracy than the analytical integration, the result is
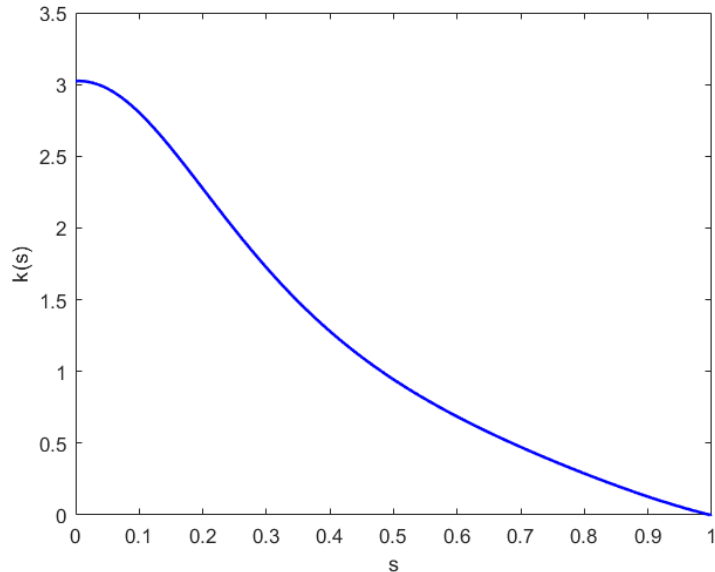
66

Figure 4.16: Curvature distribution

still accurate and the process is very fast. The equation which gives the final non dimensional bending energy is 2.26. Basically the result of the flag's edge detection algorithm is an output of four vectors, whose elements correspond to a point on the flag's edge in a ordered manner:

- s curvilinear coordinate vector;
- x/L coordinate vector;
- y/L coordinate vector;
- k curvature vector.
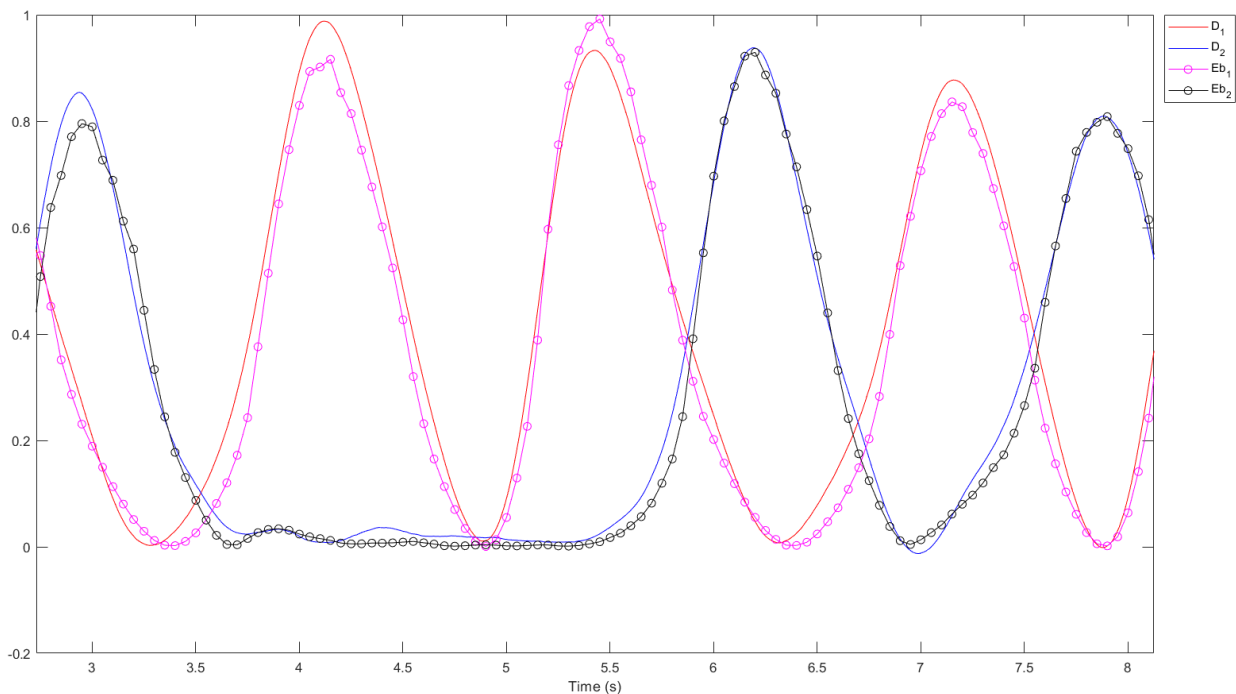
For simplicity the points are equally spaced along s.

Figure 4.17: Plot of the self-normalized synchronized drags and non dimensional bending energies in time

An example of the final result which is obtained from the synchronized data from the load cells and the cameras is presented in figure 4.17, where the magnitudes are normalized with respect to their own maximum value. The linear correlation between the drag and the non dimensional bending energy is evident, moreover this result justifies the offset removal operated on the load cell data. Not all the cases on the

test matrix have such a clean plot, in some cases the non dimensional bending energy presents some artifacts due to imperfections of the algorithm in processing the images with different light conditions, which are due to the motion of the rear flag with respect to the light source.

4.3 Characterization of the samples

The samples are characterized mechanically through a tensile test which was performed at the end of the experiment, and by evaluating their angle of attack at zero flow condition and their isolated performance through the aforementioned procedure.

Tensile test

The static tensile test is a destructive test that gives as a result the stress against strain curve of the material. Since all the samples are made of the same material, the curve is expected to be the same for all of them.
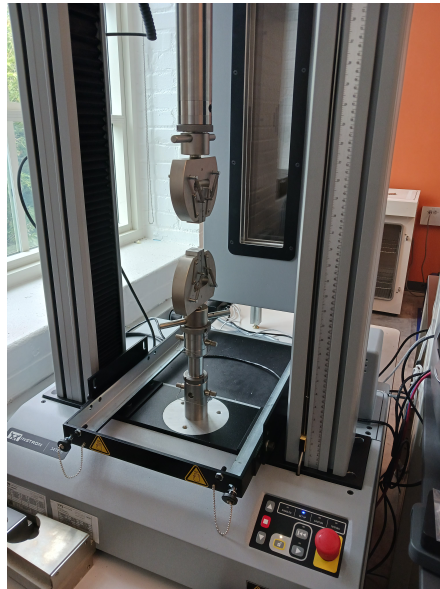
Figure 4.18: Tensile test apparatus

The apparatus for executing a tensile test is depicted in figure 4.18, the machine saves the time sequence of the displacement and of the force measured by an integrated load cell in a file. The displacement can be converted to a **engineering strain** by dividing it for the initial free length of the sample, which was set to be 3 cm, and the force can be turned into a **engineering stress** by dividing it for the cross section area of the sample, which was measured before the test with a pair of calipers (width measurement) and a micrometer (thickness measurement).
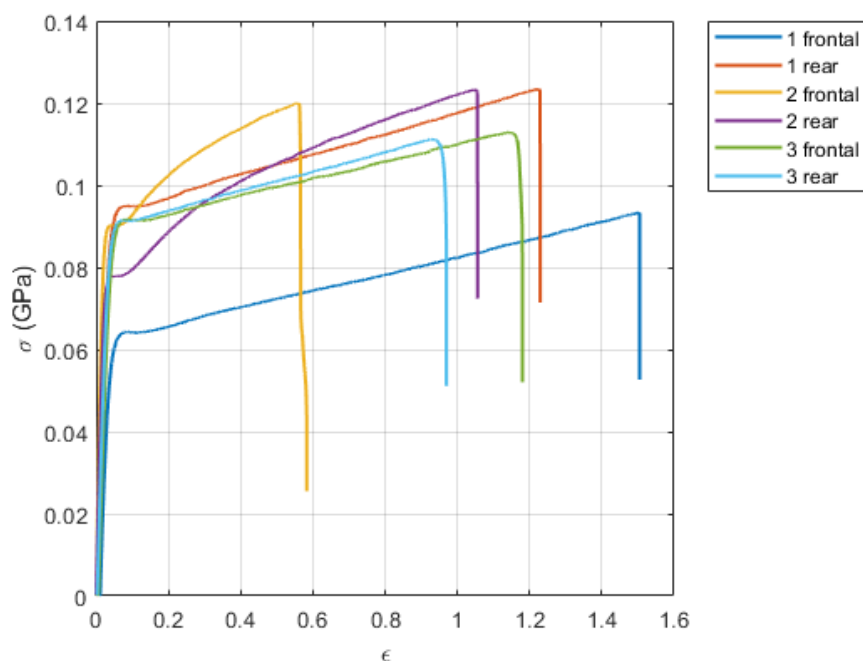

Figure 4.19: Engineering stress against engineering strain ($\sigma - \epsilon$)

The results of the test for all of the 6 flags is reported in figure 4.19. In all of them it is possible to observe the elastic region, the very first linear part of the curve, and the plastic region, which starts right after the yielding point, finally the rupture point is characterized by a sudden reduction of the stress. The curves are different in terms of yielding stress, maximum elongation and rupture stress. One possible source of inaccuracy is the specimens' geometry, which does not follow the standards by [18]. The reason is that the flag's dimensions are small, see table 2.2, by consequence it is technically difficult to cut the sample. This could provoke differences among the samples, nonetheless material's imperfections could also play a role in this sense.

1 frontal	1 rear	2 frontal	2 rear	3 frontal	3 rear
3.00	3.31	7.16	4.51	3.23	3.43

Table 4.4: Young Modulus [GPa]

Finally the Young modulus is calculated by fitting part of the elastic regime of the curve with a line, that is a first order polynomial, and by extracting its slope. The final result is shown in table 4.4, where the elastic modulus values are in GPa. Despite the fact that the uncertainty in the tensile test is unknown, it is clear that the dynamics of the flags will be different, because the actual non dimensional bending stiffness is different from the one calculated in the design phase. The elastic modulus of PET was considered to be 5 GPa from the literature, the mean of the values from table 4.4 is about 4.11 GPa, which is lower than the literature value. This is due to the use of engineering stress and strain in the modulus calculation, the valuea is higher by using true stress and strain.

Furthermore the flags cut from the same sheet have similar elastic moduli, a part from sample number two. Since it is unlikely that the Young modulus value is much higher than 5 GPa, it is possible to assume that some error occurred for test '2 frontal'. Therefore it will be supposed that its real value is close to 4.51 GPa, which is the result from test '2 rear'. In any cases the tensile test results look consistent with what was observed in the experiment, this aspect will be better discussed later in this document.

Isolated performance

Data about the isolated flags has been collected in order to compare their isolated performance to the one of the double flag arrangement. Both load cell's data and edge tracking images were used to study the flag's dynamics.

The main output parameters from the post processing for the isolated cases are listed in table 4.5. They are the time averaged drag coefficient, the flapping frequency and the time averaged non dimensional bending energy. More details about the flag dynamics can be extracted from the tracking, as for example the flapping amplitude, but they are not necessary to the purpose of the experiment.

Sample	$\bar{C_D}$	f [Hz]	$\bar{E_b}$
1 frontal	0.704	0.333	0.123
1 rear	0.694	0.35	0.109
2 frontal	0.561	0.367	0.0783
2 rear	0.606	0.367	0.0895
3 frontal	0.653	0.367	0.103
3 rear	0.656	0.35	0.106

Table 4.5: Isolated flags performance

From these results it is possible to assess that some flags flap more efficiently than others at the design flow velocity, see table 3.6. Particularly flag '1 frontal' shows the highest time averaged drag coefficient and non dimensional bending energy, while samples '2 frontal' and '2 rear' have the worst performance, remember from table 4.4 that they also have the highest elastic modulus, so this can be the reason behind their lower efficiency.

Angle of attack

To complete the characterization, the tracking of each sample at zero flow condition was executed to verify that the samples were straight enough to avoid influence from non-zero angle of attack [21].
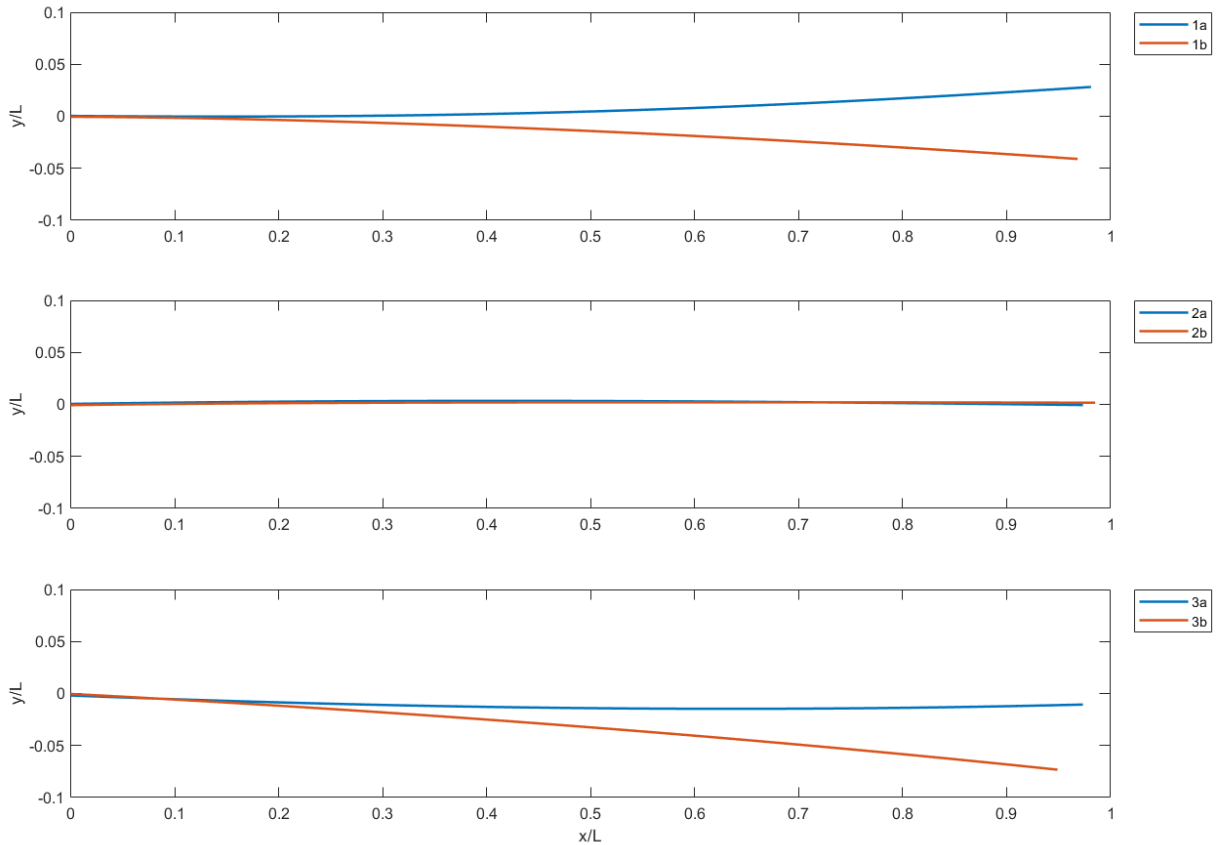
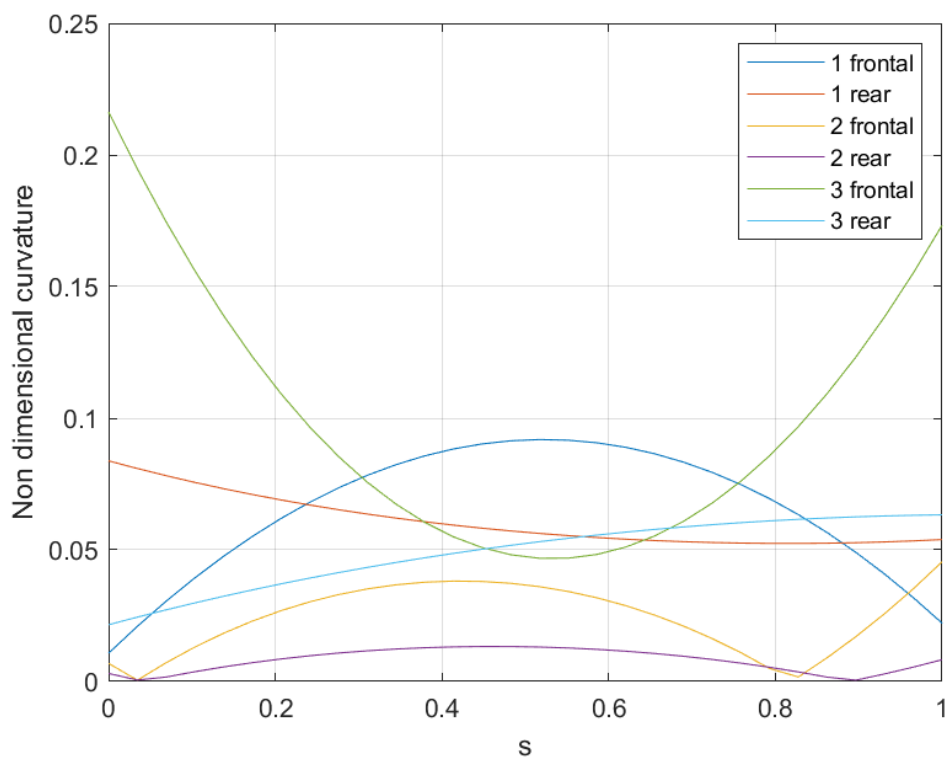Figure 4.20: Edge at zero flow condition

Figure 4.21: Residual curvature

Figure 4.20 plots the flags' edge at zero flow condition, the residual curvature is evident for all the samples, even though for samples '2 frontal' and '2 rear', central

plot, it is much less. From this data it is not possible to get an estimation of the angle of attack for each flag directly because the camera is not aligned with the water tunnel axis, therefore the x axis does not correspond necessarily to the flow direction. Nonetheless it is possible to calculate the angle in between the two flags for each couple, and it was found to be always less than 5° (sample 1: 4.07^o; sample 2: 0.13^o; sample 3: 3.79^o). The inverted flags were placed in such a way that the flow direction falls in between the flags, by consequence the angle of attack is lower than 5° in all the cases at zero flow condition. Since the angle of attack affects the inverted flag's dynamics substantially when it exceeds 15° [36], it does not add any new degrees of freedom to the analyzed system.

Furthermore from the tracking of figure 4.20 the curvature distribution along the curvilinear coordinate can be calculated as well, the result is plotted in figure 4.21.

As already anticipated, samples '2 frontal' and '2 rear' have the lowest residual curvature values, the other samples have slightly higher values but still they are not relevant to affect the flag's dynamics. As an example compare diagram 4.21 with graph 4.16 which plots the curvature distribution of the inverted flag during bending.

4.4 Results

Here the results of the single tests are reported and briefly commented, while at the end of the section the ensemble mean and standard deviation for the time averaged drag coefficient $\bar{C}_D$ and for the flapping frequency f are presented along with the results from the processing of the synchronized data.

Six independent tests were performed for the fast acquisition, two tests for each sample couple of flags. As for example for the sample couple of flags number 1 tests 1 and 2 were performed. For sample 2 other two independent experiments, namely 1 and 2 were executed. The same is valid for sample number 3.

Time averaged drag coefficient
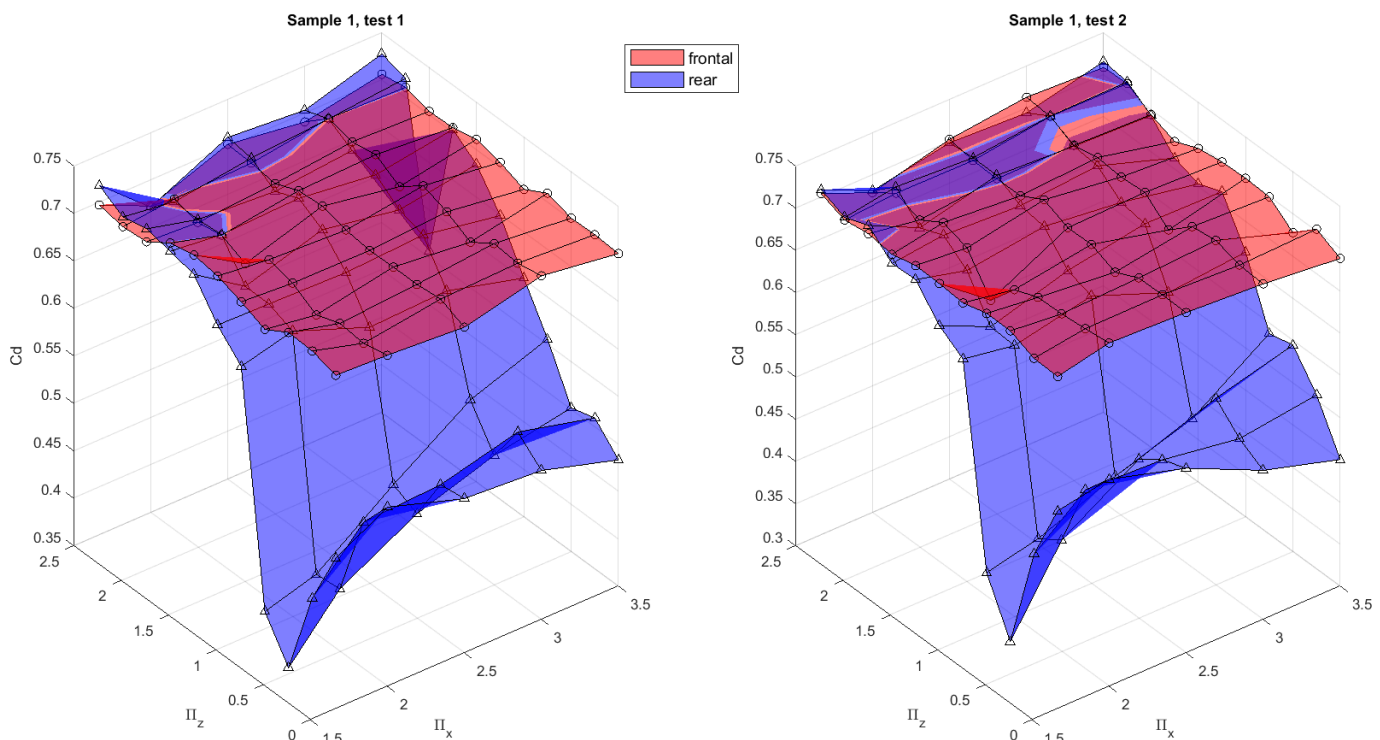
Figure 4.22: $\bar{C}_D$ plot sample 1

Figure 4.22 reports two independent tests on the first couple of flags '1 frontal' and '1 rear'. In all the following pictures the result for the frontal flag is represented by the red surface, while the colour blue is used for the rear flag. Since the time averaged drag is used as a parameter for performance comparison between the two flags, it is possible to assess that the frontal flag is not affected by the rear flag substantially, while this last presents sudden change in $\bar{C}_D$ in the z direction, remember the scheme in figure 1.7, and slighter change in the x direction. These variations will be better explained in chapter 5, now what is important to notice is that the two tests gave the same results on the whole test matrix, for both the trend and the values of the time averaged drag coefficients. This means that the experiment was repeatable and successful.

Figure 4.23 plots the results from test 1 and test 2 for the second sample of flags, respectively left and right. Also in this case the experiment is repeatable because the two independent tests produced the same result, but the performances of the two flags appear to be substantially different from those of sample 1 both in magnitude and overall trend. Figure 4.24 plots the results from test 1 and test 2 for the third sample of flags, again the experiment is repeatable because the two independent tests gave the same result for sample number three as well, but still the overall trend and values of the time averaged drag are different from the ones of the first two sample couples.

The results of the $\bar{C}_D$ in the tandem configuration ($\Pi_z = 0$) are compared with data from the literature, specifically by [16]. From a 2D simulation they show that
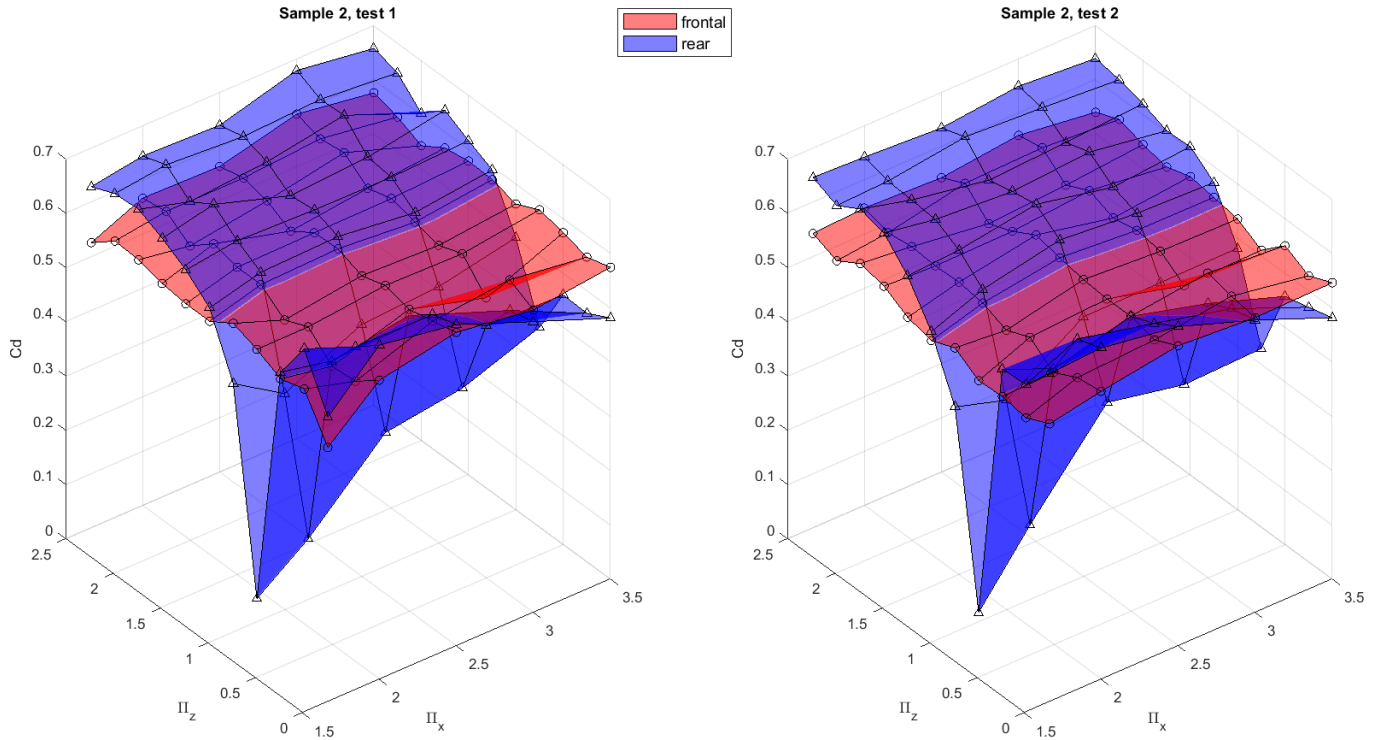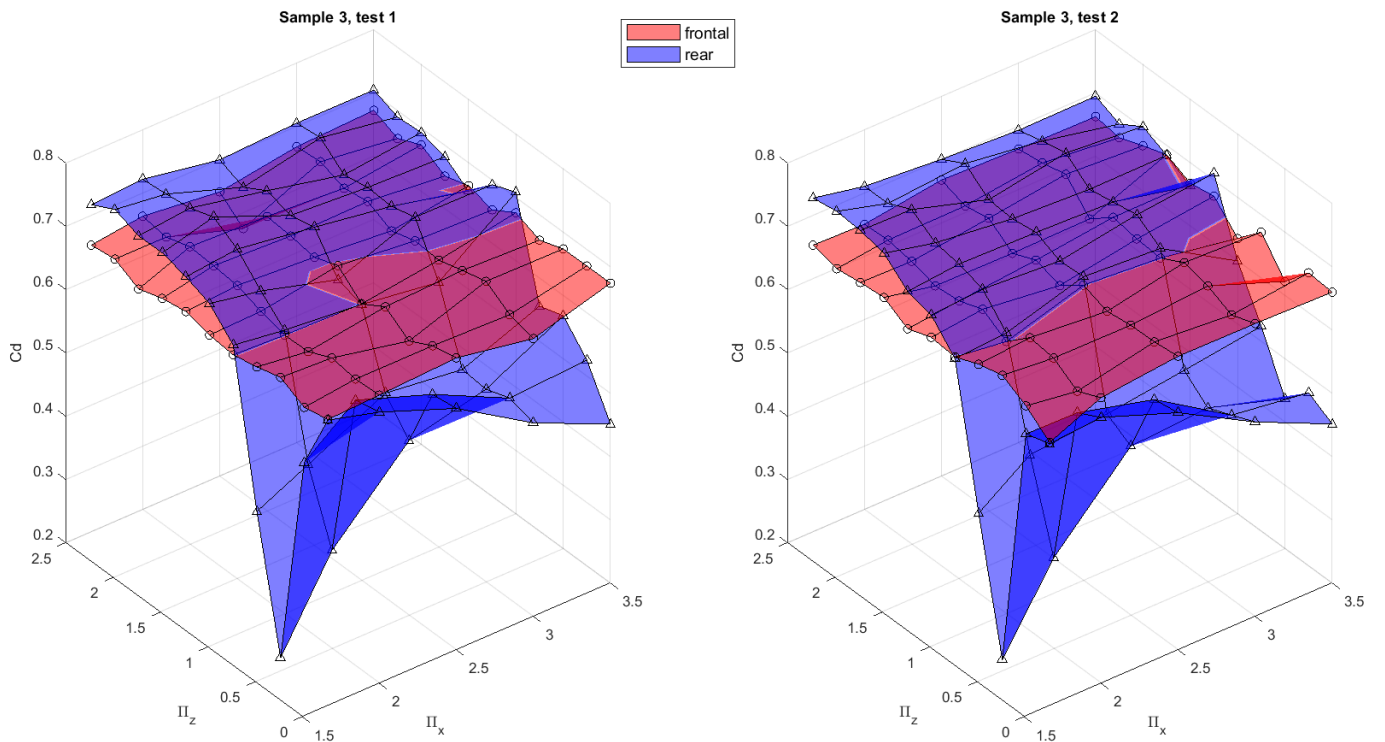
Figure 4.23: $\bar{C}_D$ plot sample 2

Figure 4.24: $\bar{C}_D$ plot sample 3

the rear flag time averaged drag coefficient is monotonically increasing along Π_x for the rear flag, while the frontal flag performance is almost the same. Instead the results previously plotted show a $\bar{C}_D$ reduction for increasing Π_x for the tandem configuration. Moreover the average values are lower with respect to the ones by the simulation which reach maxima of $\bar{C}_D = 1.5$. The differences can be due to the geometry of the flags used in the experiment, which are slender flags and do not behave like 2D flags, and to the computation of the drag coefficient, which is different between the 2D and the 3D cases.
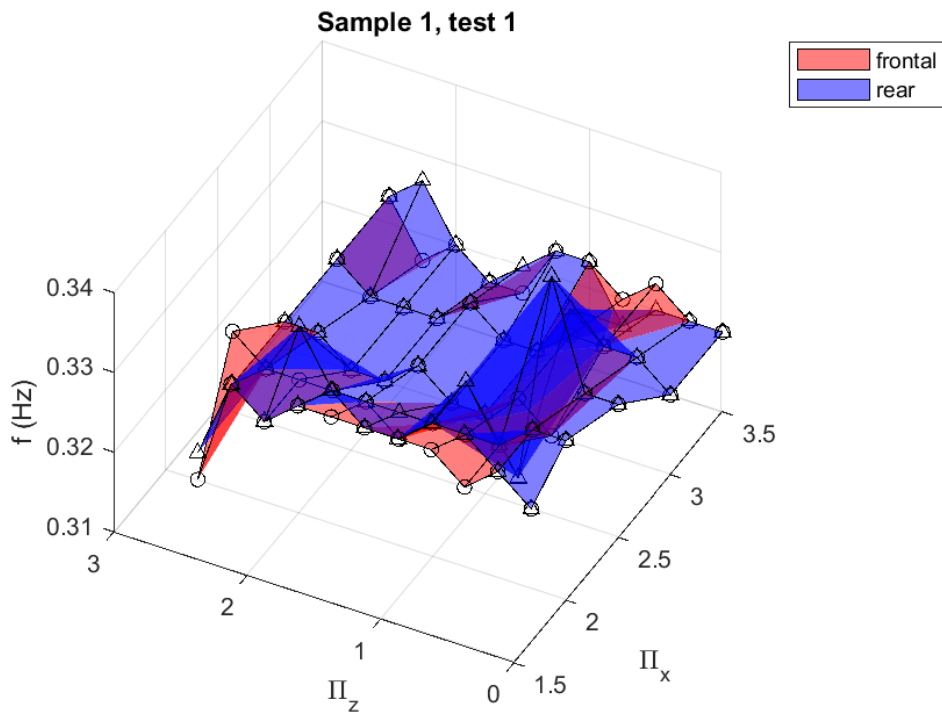
74

Flapping frequency

Figure 4.25: Flapping frequency plot sample 1

It was decided to report only the results from test number 1 for each sample of flags not to create confusion. Indeed the results for the same sample of flags are very similar and almost identical as in the previous section. Figure 4.25 reports the plot of the frequency values over the whole test matrix for sample number 1. It is interesting to notice that the range of flapping frequency is very low, this means that the frontal and rear flag always flap with almost the same period. This is a hint of existing interaction between them.
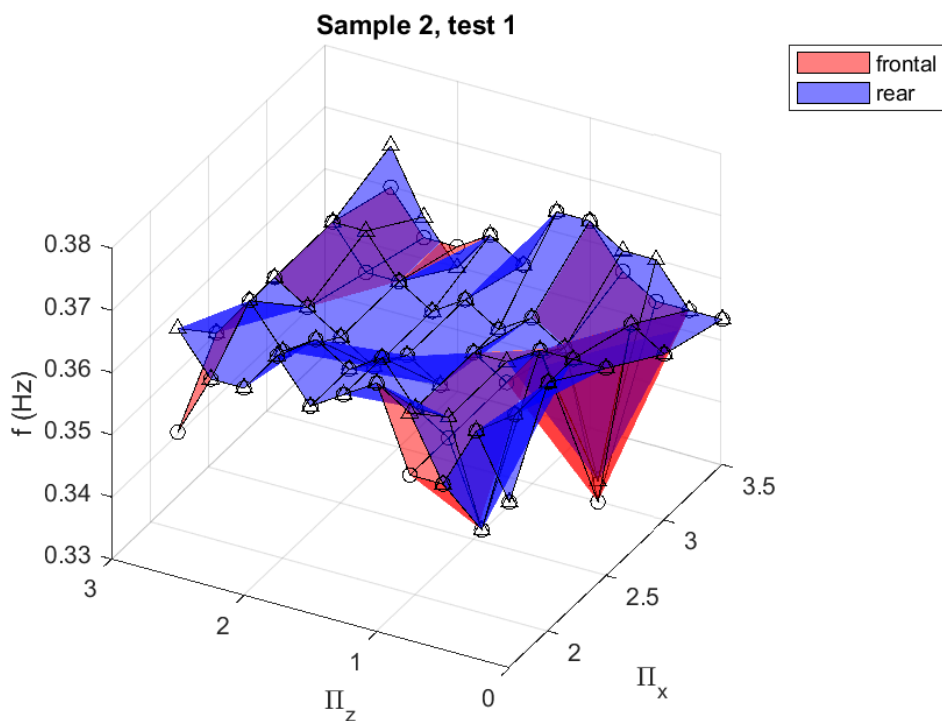

Figure 4.26: Flapping frequency plot sample 2

Figure 4.26 reports the plot of the frequency values over the whole test matrix for sample number 2. The most important detail to notice is that the flapping frequency is higher with respect to sample number 1 on most of the test matrix.
Figure 4.27 reports the plot of the frequency values over the whole test matrix for the third sample couple of flags. Another interesting aspect emerges from this last diagram,

the frequencies of the frontal and the rear flag appear to get away when the flags are farther away one another. This still could potentially be a hint of an existing coupling between the two, in fact the interaction would get weaker as the flags are more distant one to the other.
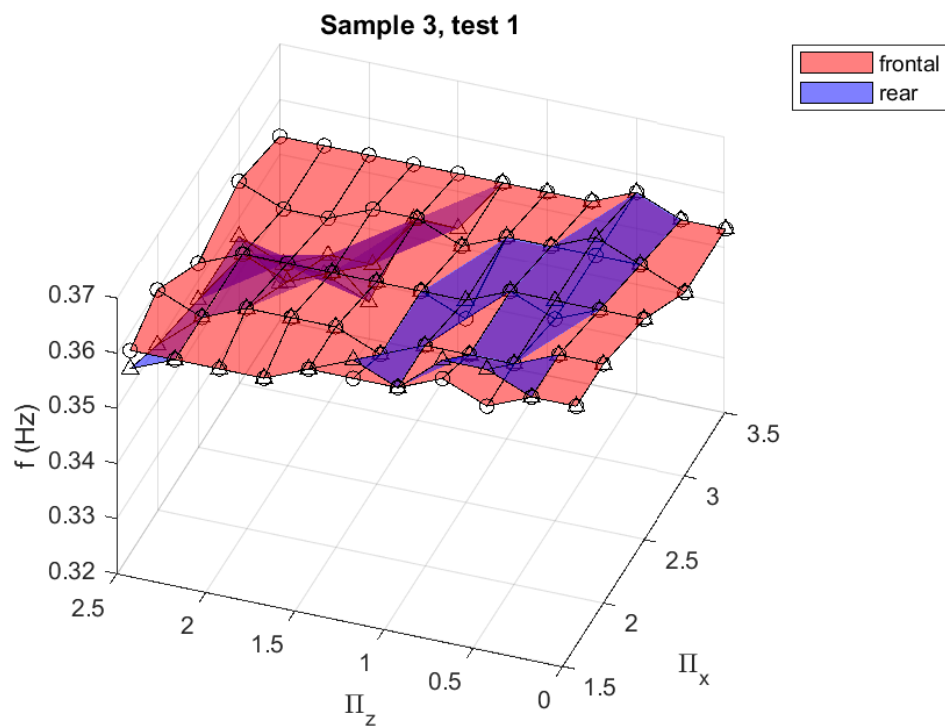

Figure 4.27: Flapping frequency plot sample 3

Phase shift

The phase lag results are presented in a different fashion with respect to the other two parameters. Since only one parameter has to be printed in the diagrams, a simple 2D graph can be used. Figure 4.28 reports the plot of the phase lag values in terms of fraction of the frontal flag's flapping period over the whole test matrix for test number 1 only for the first sample couple of flags.
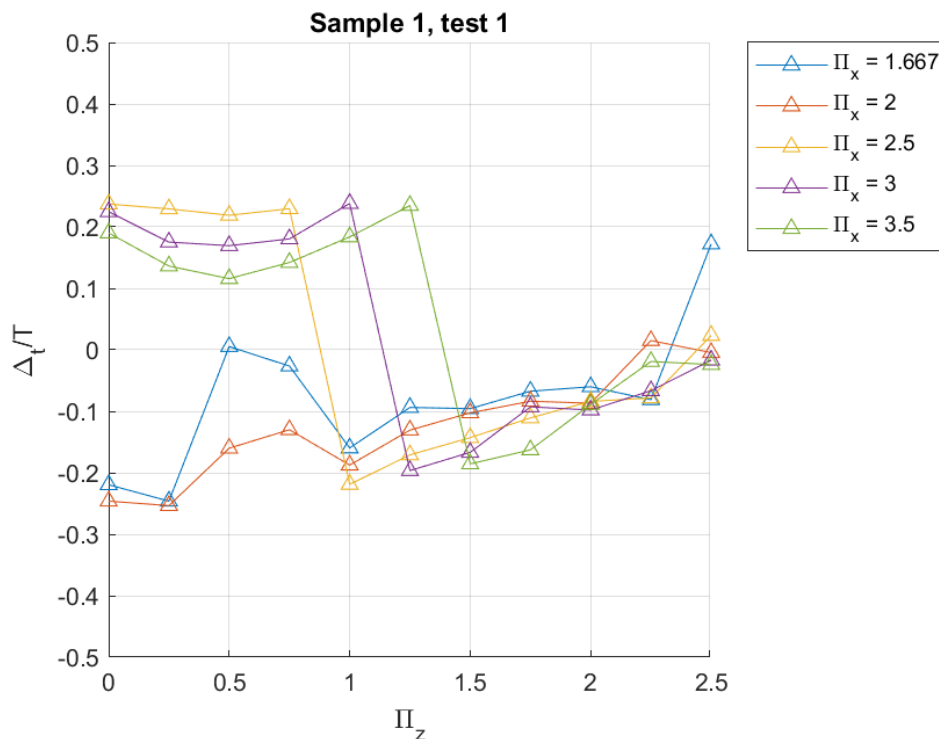

Figure 4.28: Phase lag plot sample 1

Figure 4.29 reports the plot of the phase lag values over the whole test matrix for test number 1 only for the second sample couple of flags.
Figure 4.30 reports the plot of the phase lag values over the whole test matrix for test number 1 only for the third sample couple of flags. The main aspects to highlight are the existence of linear patterns both along Π_x and Π_z and the modulus of the parameter itself which is always between 0 and 0.25.
The first aspect is not easy to visualize because of the phase inversions which occur in the phase lag. It would be better to shift the lag of half a period $(+0.5)$ for all those points which fall in the lower region of the diagrams 4.28 and 4.29, in the same way it is possible to shift specific points of diagram 4.30 of the same quantity to obtain an ordered graph. Since this procedure is quite arbitrary it has not been performed on the results, but it would be valid because of the presence of a correlation peak every half a period of the frontal flapping flag.
The second aspect is related to the nature of the correlation between the frontal and rear drag signals. By considering a time span of one period, two peaks of the correlation coefficients can be found, from what assessed in the phase shift post processing section. Since the peaks are half period apart, the closest to the zero phase lag would not be farther than a quarter of period from the zero.
Because of the uncertainty on the phase lag data, it was decided not to compute an ensemble mean over all the test cases, because it would produce too a high standard deviation due to the phase inversions. Nonetheless the data show linear patterns in the phase lag, this signifies that as the rear flag moves it adapts to the wake vortexes of the frontal flag, justifying the existence of an interaction.

The phase lag for the tandem configuration $(\Pi_z = 0)$ was compared with data from the literature. The reduced velocity U^* for the experiment described in this work is 4.35, as reported in table 3.6, which is higher than the range studied in [15]. Nonetheless it is possible to speculate about the results. The slope of the phase lag along Π_x was calculated by interpolating in the least square sense the lag data. The
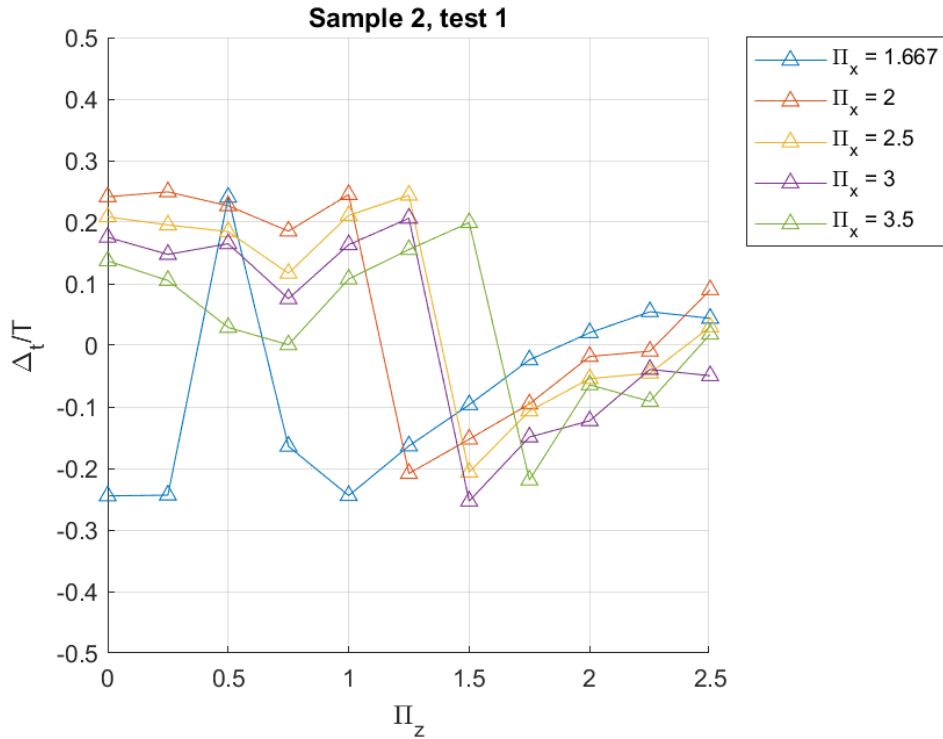
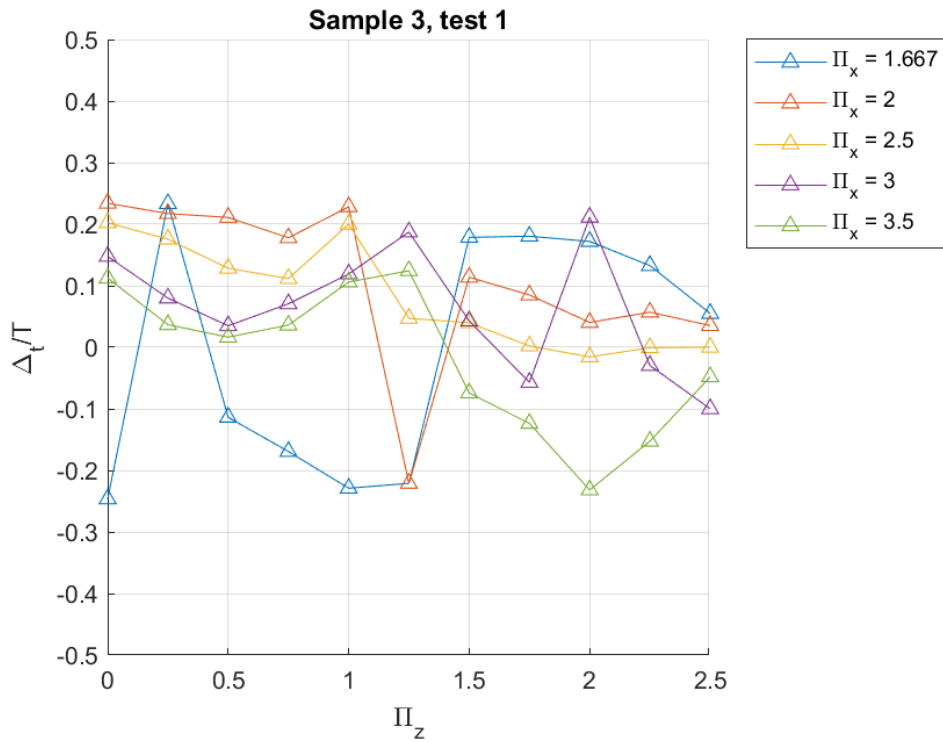Figure 4.29: Phase lag plot sample 2

Figure 4.30: Phase lag plot sample 3

slope was always found to be in between $-0.079 < \frac{\partial (\Delta_t/T)}{\partial \Pi_x} < -0.042$. In their work Hu et al. [15] plots the phase lag for tandem flags. In the regime of interest, which is mainly $\Pi_x \geq 2$ and $U^* \simeq 3.6$, the slope is about -0.067. Even if the reduced velocities are different in the two cases, it is important to keep in mind that the flags' geometry is different, this can explain the difference in the phase lag parameter as well, but still the results are very similar.

Load cell data: final average and standard deviation

Despite the fact that the samples present different results, a final mean is computed over all the performed tests for all the parameters. At the same time the standard deviation is computed for each mean to get an estimation of the uncertainty over the test matrix.
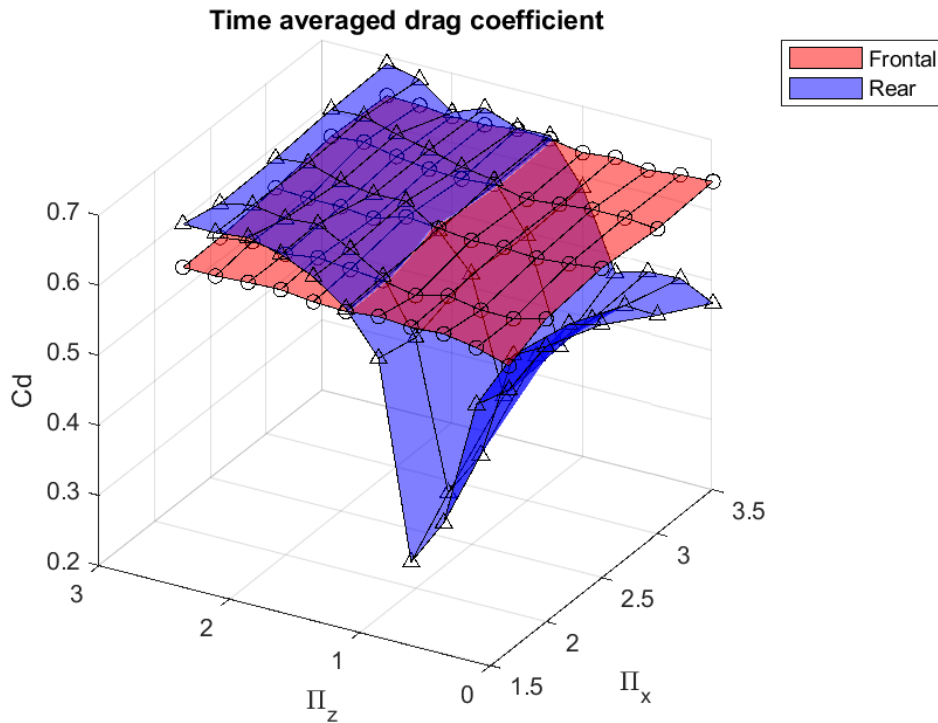
Figure 4.31: Time averaged C_D, ensemble mean
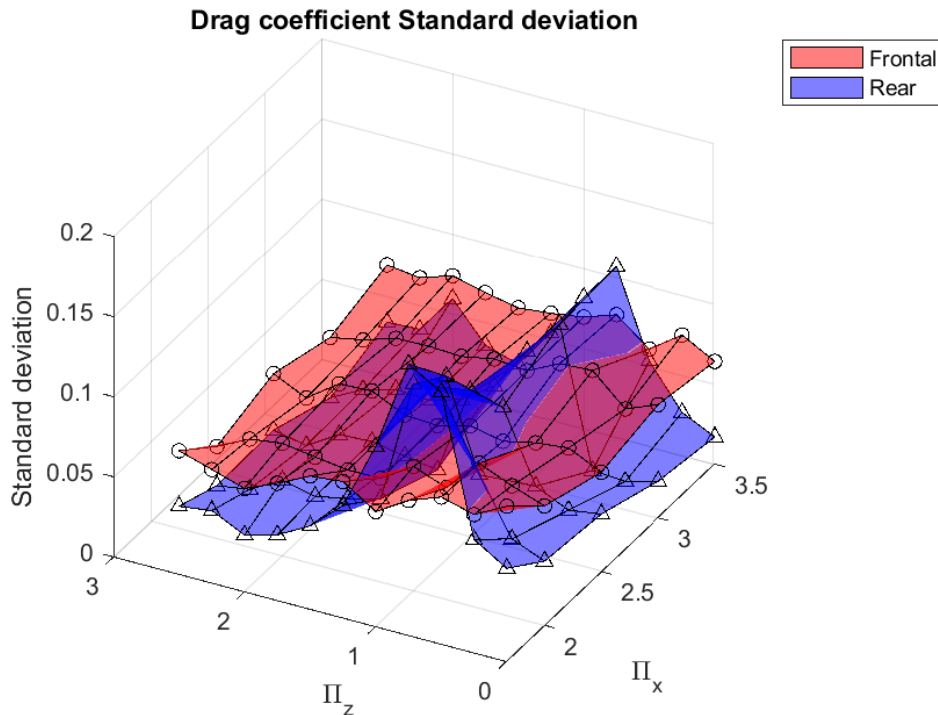
Figure 4.32: Time averaged C_D, standard deviation

The final ensemble average of all the performed tests for the $\bar{C}_D$ parameter is plotted in figure 4.31, and the relative standard deviation[3] is reported in figure 4.32. The result assesses that the most likely behaviour is that the rear flag performance is higher with respect to the frontal flag's when it is out of the incoming wake[4]. At $\Pi_z = 0.75$, that means 25% overlap, the worst performance of the rear flag is observed. In this condition the rear flag usually presents antisymmetric flapping, spending half of the flapping period in the straight mode. Another detail which was already pointed out previously is that the frontal flag is poorly affected by the rear one and its performance is constant over the whole test matrix. The same conclusion can be drawn from figure

---

[3]The standard deviation is computed through the 'std' MATLAB function; it normalizes with respect to n=N-1 where N is the number of tests in this case. The formula is the following: $s = \sqrt{\frac{1}{n}\Sigma_{i=1}^{N}(x_i - \mu_x)^2}$ where x_i is the considered magnitude for each test i and μ_x is the ensemble mean over all the x_i.

[4]Reminder: the tip to tip condition occurs when $\Pi_z = 1$.

4.32. In this last case the red surface is quite flat while the blue one has a saddle at $\Pi_z = 0.75$ where the rear flag performance is worst. The standard deviation is lower where consistent flapping occurs, therefore the lower values of the blue surface with respect to the red one's can signify that an eventual coupling between the two flags can lead to a more consistent flapping of the rear flag.
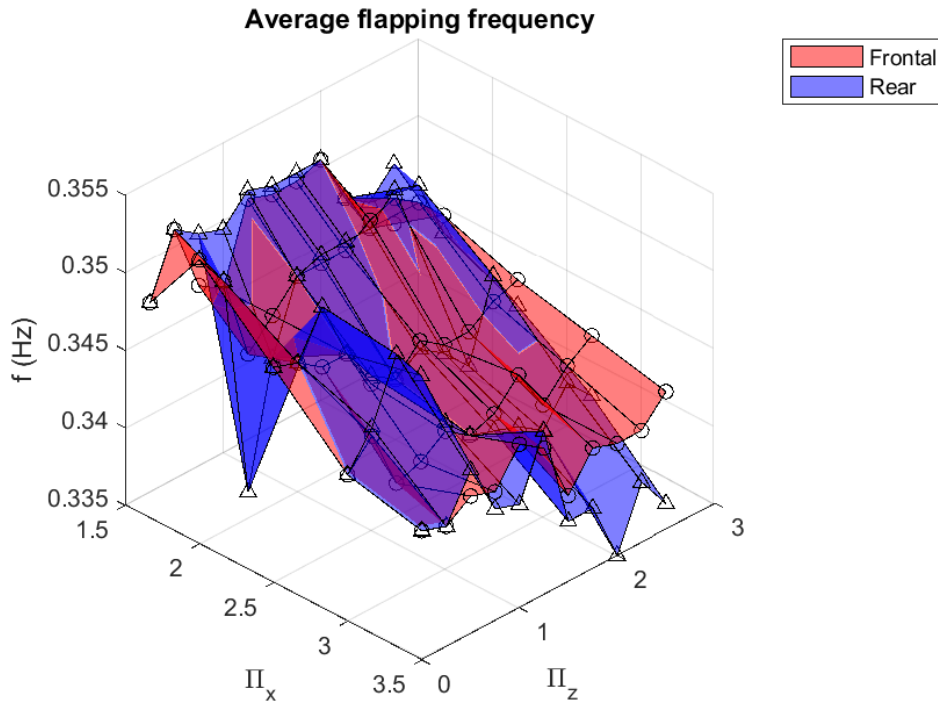

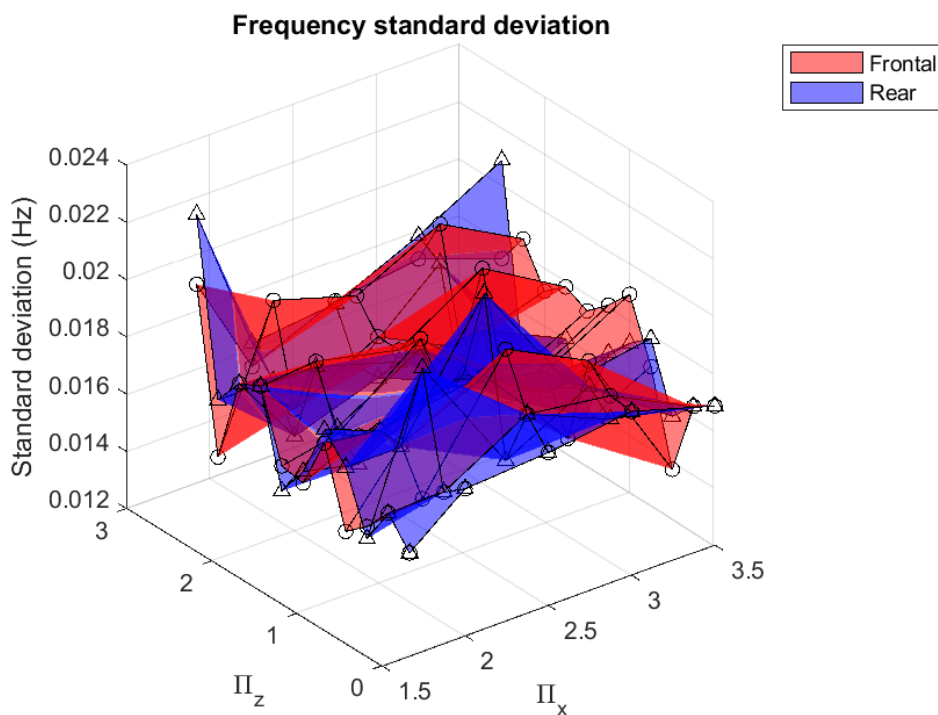Figure 4.33: Flapping frequency, ensemble mean

Figure 4.34: Flapping frequency, standard deviation

Figures 4.33 and 4.34 are the diagrams of the ensemble mean of the flapping frequency over all the six tests and the relative standard deviation respectively. The standard deviation on the flapping frequency being low with respect to the ensemble mean value means that the experiment was successful. The average flapping frequency is about 0.345 Hz on most of the test matrix. An interesting aspect is a neat increase of the ensemble mean for higher Π_z, this implies that when the flags are independent one another, they flap a bit faster.

The performance difference between the two flags at the edge of the test matrix cannot be explained in terms of flapping frequency, because they flap at the same rate. Again it

is pointed out that the highest standard deviation occurs where the performance drops, this is valid also for the flapping frequency parameter. Higher standard deviation of the flapping frequency means more chaos and irregularity of the flag's dynamics and consequently a less consistent flapping.

Synchronized data: final result

From the signal presented in figure 4.17, it is possible to obtain the time averaged drag coefficient and non dimensional bending energy as described in the array of equations 2.28 for each case of the test matrix 4.3.
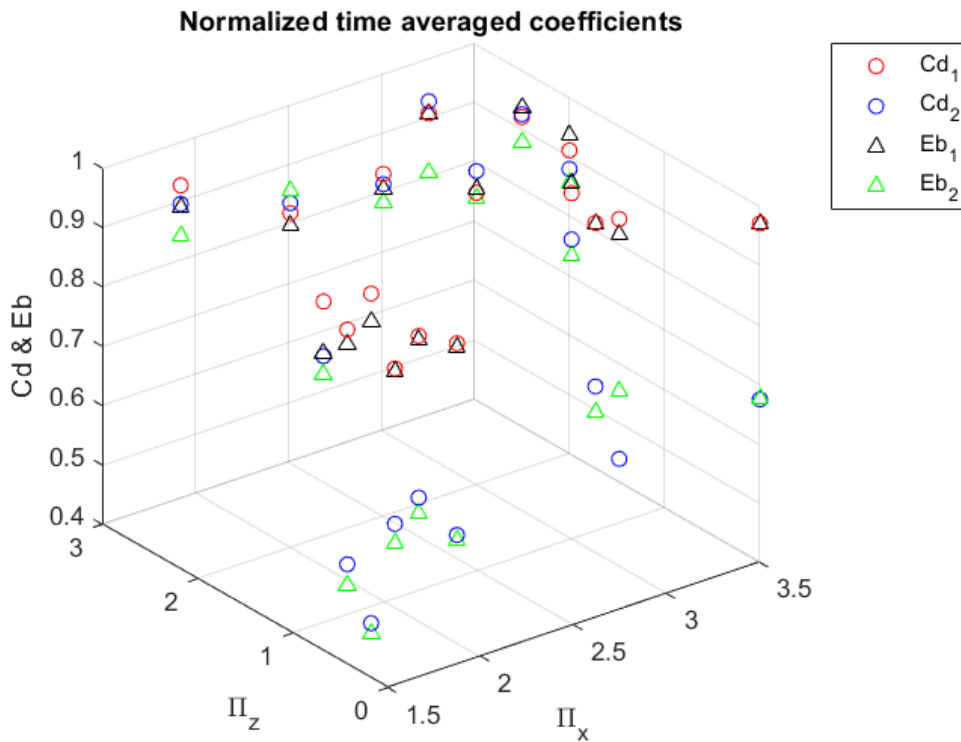

Figure 4.35: Sample 1, synchronized data processing final result
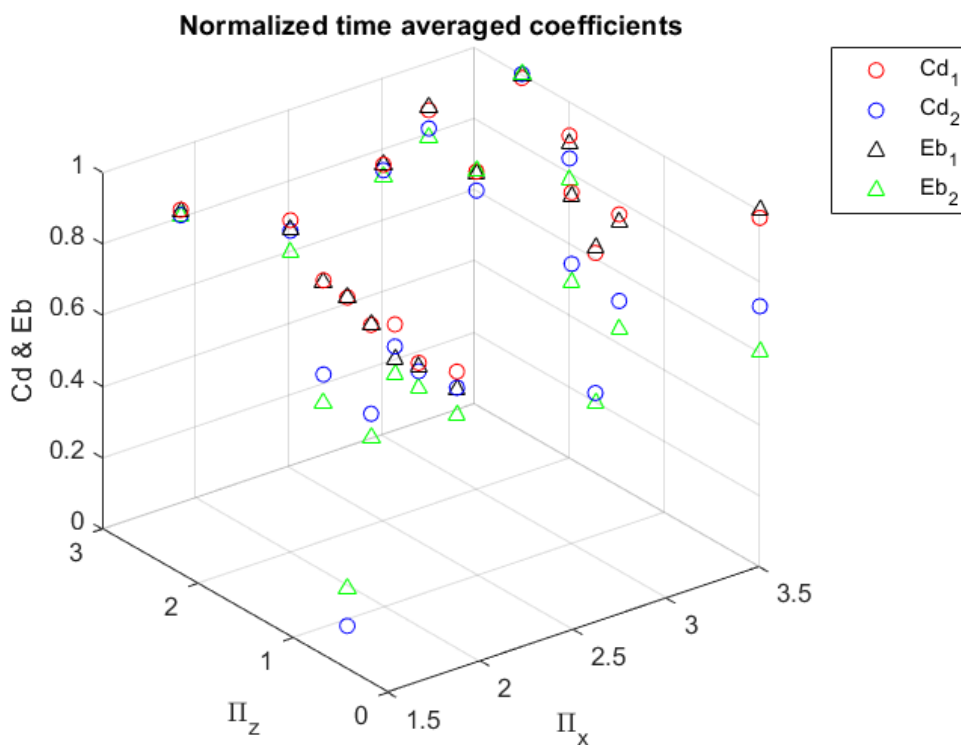

Figure 4.36: Sample 2, synchronized data processing final result

Figures 4.35, 4.36 and 4.37 are the diagrams of the final result obtained by post processing the data collected with the synchronized acquisition respectively for the sample couples of flags 1, 2 and 3. The results are normalized with respect to their own maximum, as done for the result presented in diagram 4.17. The data are plotted on the 17 cases listed in table 4.3 on the test matrix. Notice that there is a correlation between Cd_1 and Eb_1, in the same fashion also Cd_2 and Eb_2 are correlated. The best correlation is observed for sample number 3, figure 4.37.
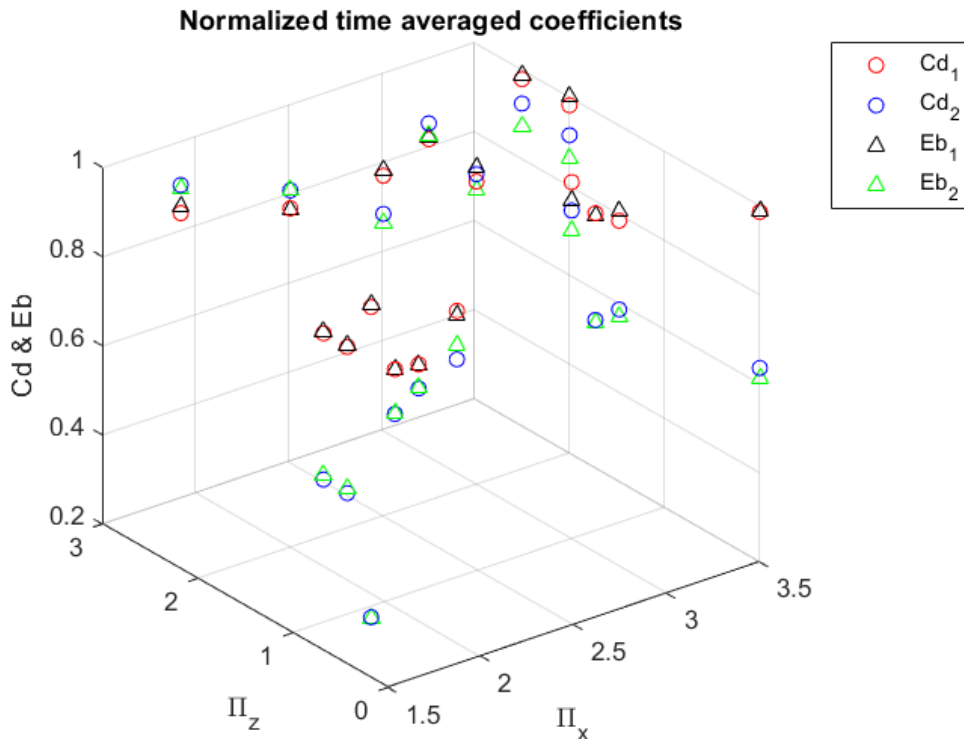

Figure 4.37: Sample 3, synchronized data processing final result

The most important consequence of these results is that the procedure of data acquisition and processing is finally validated.
More information can be extracted from the tracking, but the algorithm still needs to be improved to adapt to different light conditions to obtain good quality tracking for all the registered cases. Indeed cases with high Π_z present high reflection on the rear flag's support, generating artifacts as edge length variations among the different frames in the final tracking. Nonetheless the procedure is good enough to prove validity of the data collection method.

Chapter 5

Conclusion and further research

This study aims at optimizing the overall energy harvesting performance of two slender inverted flags in tandem echelon formation. The configuration was inspired by large migrating birds' formation flight where the members in the rear part of the stock are able to exploit the periodic upwash generated by the birds ahead of them by avoiding the downwash to reduce their induced drag and saving energy during the flight. The main difference between a flapping wing and an inverted flag is that the first is active while the last one is passive, but still it gives most of the energy absorbed from the fluid flow back to it in the form of vortexes, imitating a flapping wing. The reason why a normal tandem configuration of inverted flags has lower performance with respect to the isolated case is the occurrence of destructive merging of leading edge vortexes on the rear flag, which causes this last to flap with lower amplitude than the frontal flag. Therefore this study focuses on how the rear flag intercepts the incoming side edge vortexes from the frontal flag to look for eventual echelons which could potentially optimize the overall energy harvesting performance.

Different echelon configurations have been compared in terms of potential of energy collection to find the optimal working point. Since the best harvesting performance of inverted flags with low bending stiffness ($B < 0.3$) verifies in the symmetric flapping regime, there is the need to use some time independent parameters for comparison. The time averaged drag coefficient was chosen, since its value is linearly correlated with the bending energy which gets accumulated in the flag during its motion. This means that an higher drag coefficient can potentially signify higher energy conversion, and by consequence higher efficiency.

Conclusion

The most relevant result is from diagram 4.31. It plots the ensemble mean of the time averaged drag coefficient over 6 independent tests for each case of the design test matrix 4.2. The red surface refers to the frontal flag, while the blue surface is related to the rear flag. The most important aspects to highlight are: the substantial independence of the frontal flag dynamics from the rear one, since the red surface is flat; the lower performance of the rear flag in all the tandem arrangements ($\Pi_z = 0$) with respect to the isolated flag as described in the literature; the worst performance of the rear flag at location were formation flight predicts the lowest induced drag ($0.5 < \Pi_z < 1$); the occurrence of a plateau at $\Pi_z \geq 2$ for the rear flag; the cross over of the blue surface over the red one at $\Pi_z = 1.25$.

The high performance of the rear flag at $\Pi_z > 1.25$ has two possible explanations:

the first is the possible existence of a coupling between the two flags thanks to the interaction of their side edge vortexes, this hypothesis is supported by the frequency diagram 4.33 where at the considered location on the test matrix the equal frequencies suggest that the rear flag is following the motion of the frontal one;

the second explanation is that the isolated rear flag has better performance than the isolated frontal flag, and when Π_z is sufficiently high the two flags are far apart that they can be almost considered isolated, in this case no coupling should happen. To support this second hypothesis table 4.5 shows that rear flag from sample 2 present clearly higher $\bar{C}_D$ than the rear flag's from the same sample in the isolated case.

By comparing the echelon formation performance with the isolated performance it emerges that the second theory is more likely to be true than the first one. In fact at $\Pi_z \geq 2$ the time averaged drag coefficient of the results in figures 4.22, 4.23 and 4.24 presents values very close to the one from the isolated case listed in table 4.5. Moreover the linear shift of the phase lag along Π_z in diagrams 4.28 and 4.29 suggest that that a coupling affects the rear flag for $\Pi_z < 1.75$.

In conclusion it was found that the positioning along z have high impact on the final configuration's performance and it is more relevant than the positioning along x. Furthermore much higher efficiency with respect to the tandem configuration can be obtained by simply placing the rear flag at $\Pi_z \geq 2$. The best trade off between performance and occupancy is obtained at $\Pi_z = 2$ for slender flags. Finally the worst harvesting potential is registered where birds' formation flight shows highest benefits, at $0.5 < \Pi_z < 1$. The observations were made for $1.67 \leq \Pi_x \leq 3.5$, therefore what has been assessed so far is valid in this range of stream wise separation distances.

Further research

The last aspect mentioned in the previous section could throw new insights on large birds' formation flight aerodynamics, in fact not only the members of the stock could benefit from upwash by the birds' ahead of them, but also their wings could turn out to be more stable to outer perturbations, in the same way as the rear flag in this study shows higher stability in that particular arrangement.

To confirm the absence of coupling in the best performance configuration of the echelon it is necessary to perform some flow visualization or simulation. A successful flow visualization is hard to carry out in this specific case, because of the unsteady behaviour and three-dimensionality of the fluid flow, moreover the body tracking should be performed at the same time. Another feasible approach is to use data from this experiment to build the dynamic boundary conditions for a numerical flow simulation. The stresses and the kinematics of the whole flags can be obtained from the edge tracking result, and the time resolution can be increased by interpolating the edge motion in time. At this point the structural elements which appear in the mathematical model of the flapping flag would be solved, and only the features of the flow field remain to be found. Still the edge tracking algorithm could not adapt effectively to the different light conditions which occurred in the test matrix, therefore it should be optimized to get good tracking in all the test cases.

Bibliography

[1] Samer Ali et al. "Heat transfer and mixing enhancement by free elastic flaps oscillation". In: *International Journal of Heat and Mass Transfer* 85 (2015), pp. 250–264.

[2] Iztok Lebar Bajec and Frank H Heppner. "Organized flight in birds". In: *Animal Behaviour* 78.4 (2009), pp. 777–789.

[3] Sankha Banerjee, Benjamin SH Connell, and Dick KP Yue. "Three-dimensional effects on flag flapping dynamics". In: *Journal of Fluid Mechanics* 783 (2015), pp. 103–136.

[4] C Brown et al. "Piezoelectric materials, a review of progress". In: *IRE Transactions on component parts* 9.4 (1962), pp. 193–211.

[5] Yujia Chen et al. "Heat transfer enhancement of turbulent channel flow using tandem self-oscillating inverted flags". In: *Physics of Fluids* 30.7 (2018).

[6] Chang-Koon Choi and Dae-Kun Kwon. "Wind tunnel blockage effects on aerodynamic behavior of bluff body". In: *Wind Struct Int J* 1.4 (1998), pp. 351–364.

[7] BR Clayton and BS Massey. "Flow visualization in water: a review of techniques". In: *Journal of Scientific Instruments* 44.1 (1967), p. 2.

[8] Olivier Doaré, David Mano, and Juan Carlos Bilbao Ludena. "Effect of spanwise confinement on flag flutter: Experimental measurements". In: *Physics of Fluids* 23.11 (2011), p. 111704.

[9] Li-Hao Feng, Yao-Wei Hu, and Jin-Jun Wang. "Flow-structure interactions of multiple inverted flags in different arrangements". In: *Experiments in Fluids* 62 (2021), pp. 1–16.

[10] C Garcıa-Baena et al. "Numerical analysis of the flow-induced vibrations in the laminar wake behind a blunt body with rear flexible cavities". In: *Journal of Fluids and Structures* 100 (2021), p. 103194.

[11] Mehdi Ghommem and Victor M Calo. "Flapping wings in line formation flight: a computational analysis". In: *The Aeronautical Journal* 118.1203 (2014), pp. 485–501.

[12] S Chad Gibbs IV, Ivan Wang, and Earl H Dowell. "Stability of rectangular plates in subsonic flow with various boundary conditions". In: *Journal of Aircraft* 52.2 (2015), pp. 439–451.

[13] Chang Qin Guo and Michael P Paıdoussis. "Stability of rectangular plates with free side-edges in two-dimensional inviscid channel flow". In: *J. Appl. Mech.* 67.1 (2000), pp. 171–176.

[14] PS Gurugubelli and RK Jaiman. "On the mechanism of large amplitude flapping of inverted foil in a uniform flow". In: *arXiv preprint arXiv:1711.01065* (2017).

[15] Yao-Wei Hu, Li-Hao Feng, and Jin-Jun Wang. "Flow-structure interactions of two tandem inverted flags in a water tunnel". In: *Physics of Fluids* 32.8 (2020).

[16] Haibo Huang, Heng Wei, and Xi-Yun Lu. "Coupling performance of tandem flexible inverted flags in a uniform flow". In: *Journal of Fluid Mechanics* 837 (2018), pp. 461–476.

[17] "IEEE Standards on Piezoelectric Crystals:Determination of The Elastic. Piezoelectric and Dielectric Constants- The Electro mechanical Coupling Factor, 1958". In: *IEEE Std 178-1958 (ANSI C83.23-1960)* (1958), pp. 1–16. DOI: 10.1109/IEEESTD.1958.8941334.

[18] ASTM International. *Standard test method for tensile properties of plastics*. ASTM international, 2014.

[19] Joseph Katz and Allen Plotkin. *Low-speed aerodynamics*. Vol. 13. Cambridge university press, 2001.

[20] Daegyoum Kim et al. "Flapping dynamics of an inverted flag". In: *Journal of Fluid Mechanics* 736 (2013), R1.

[21] Se Hwan Lim and Sung Goon Park. "Numerical analysis of energy harvesting system including an inclined inverted flag". In: *Physics of Fluids* 34.1 (2022).

[22] William Mason and Sergio Iglesias. "Optimum spanloads in formation flight". In: *40th AIAA Aerospace Sciences Meeting & Exhibit*. 2002, p. 258.

[23] Oluwafemi Ojo et al. "Aspect ratio effects in wind energy harvesting using piezoelectric inverted flags". In: *Active and Passive Smart Structures and Integrated Systems XIII*. Vol. 10967. SPIE. 2019, pp. 177–188.

[24] Oluwafemi Ojo et al. "Aspect ratio-dependent hysteresis response of a heavy inverted flag". In: *Journal of Fluid Mechanics* 942 (2022), A4.

[25] Geffrey K Ottman et al. "Adaptive piezoelectric energy harvesting circuit for wireless remote power supply". In: *IEEE Transactions on power electronics* 17.5 (2002), pp. 669–676.

[26] Joe Pahle et al. "An initial flight investigation of formation flight for drag reduction on the C-17 aircraft". In: *AIAA atmospheric flight mechanics conference*. 2012, p. 4802.

[27] Michael P Paidoussis. *Fluid-structure interactions: slender structures and axial flow*. Vol. 1. Academic press, 1998.

[28] Steven J Portugal et al. "Upwash exploitation and downwash avoidance by flap phasing in ibis formation flight". In: *Nature* 505.7483 (2014), pp. 399–402.

[29] Atika Qazi et al. "Towards Sustainable Energy: A Systematic Review of Renewable Energy Sources, Technologies, and Public Opinions". In: *IEEE Access* 7 (2019), pp. 63837–63851. DOI: 10.1109/ACCESS.2019.2906402.

[30] Sophie Ramananarivo et al. "Flow interactions lead to orderly formations of flapping wings in forward flight". In: *Physical Review Fluids* 1.7 (2016), p. 071201.

[31] Shawn Ryan et al. "The Bombora wave energy converter: A novel multi-purpose device for electricity, coastal protection and surf breaks". In: *Australasian Coasts & Ports Conference 2015: 22nd Australasian Coastal and Ocean Engineering Conference and the 15th Australasian Port and Harbour Conference: 22nd Australasian Coastal and Ocean Engineering Conference and the 15th Australasian Port and Harbour Conference*. Engineers Australia and IPENZ Auckland, New Zealand. 2015, pp. 541–546.

[32] Jaeha Ryu et al. "Flapping dynamics of an inverted flag in a uniform flow". In: *Journal of Fluids and Structures* 57 (2015), pp. 159–169.

[33] Salem Saadon and Othman Sidek. "A review of vibration-based MEMS piezoelectric energy harvesters". In: *Energy conversion and management* 52.1 (2011), pp. 500–504.

[34] John E Sader, Cecilia Huertas-Cerdeira, and Morteza Gharib. "Stability of slender inverted flags and rods in uniform steady flow". In: *Journal of Fluid Mechanics* 809 (2016), pp. 873–894.

[35] John E Sader et al. "Large-amplitude flapping of an inverted flag in a uniform steady flow–a vortex-induced vibration". In: *Journal of Fluid Mechanics* 793 (2016), pp. 524–555.

[36] Kourosh Shoele and Rajat Mittal. "Energy harvesting by flow-induced flutter in a simple model of an inverted piezoelectric flag". In: *Journal of Fluid Mechanics* 790 (2016), pp. 582–606.

[37] Yi-Chung Shu and IC Lien. "Efficiency of energy conversion for a piezoelectric power harvesting system". In: *Journal of micromechanics and microengineering* 16.11 (2006), p. 2429.

[38] Swadesh Suman et al. "Numerical investigation and experimental validation of shape and position optimisation of a static wavy flag for heat transfer enhancement". In: *International Journal of Ambient Energy* 43.1 (2022), pp. 3237–3245.

[39] Liaosha Tang, Michael P Païdoussis, and Jin Jiang. "Cantilevered flexible plates in axial flow: energy transfer and the concept of flutter-mill". In: *Journal of Sound and Vibration* 326.1-2 (2009), pp. 263–276.

[40] XD Xie, Q Wang, and N Wu. "Energy harvesting from transverse ocean waves by a piezoelectric plate". In: *International Journal of Engineering Science* 81 (2014), pp. 41–48.

[41] Zhengbao Yang, Alper Erturk, and Jean Zu. "On the efficiency of piezoelectric energy harvesters". In: *Extreme Mechanics Letters* 15 (2017), pp. 26–37.

[42] Yuelong Yu, Yingzheng Liu, and Xavier Amandolese. "A review on fluid-induced flag vibrations". In: *Applied Mechanics Reviews* 71.1 (2019).

[43] XL Zhong et al. "Experimental and numerical study of heat transfer performance of a channel flow with an inverted flag". In: *International Journal of Heat and Mass Transfer* 193 (2022), p. 122969.
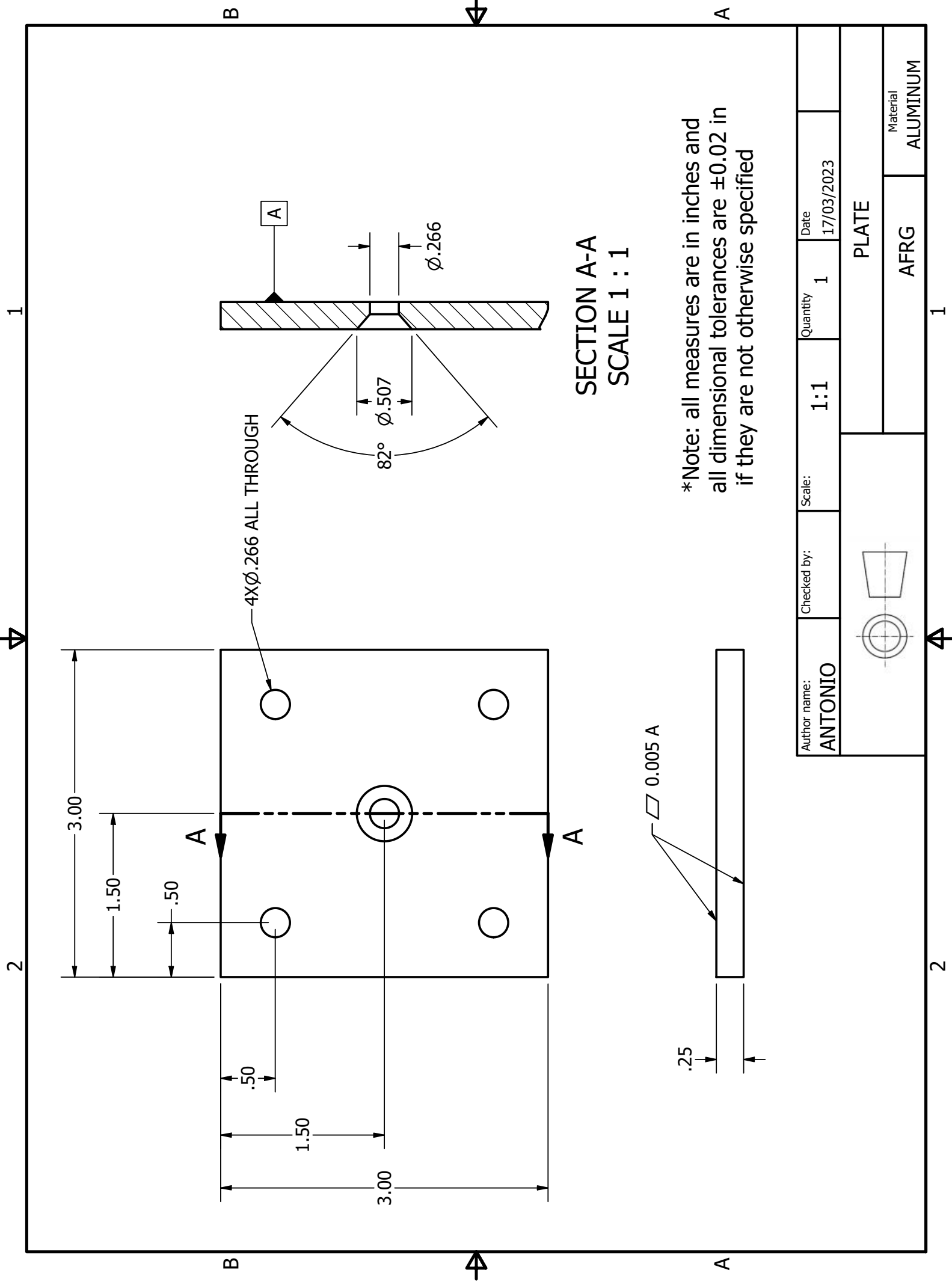
Appendix A

Technical drawings

In this section of the appendix the technical drawings of the setup supporting structure are reported, the views follow the third dihedral standard and the quotes are in inches. The boxed quotes can be considered as datum features, since they describe the dimensions of the starting piece of aluminum to be processed.
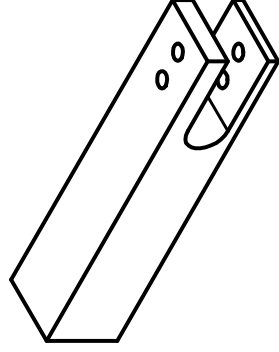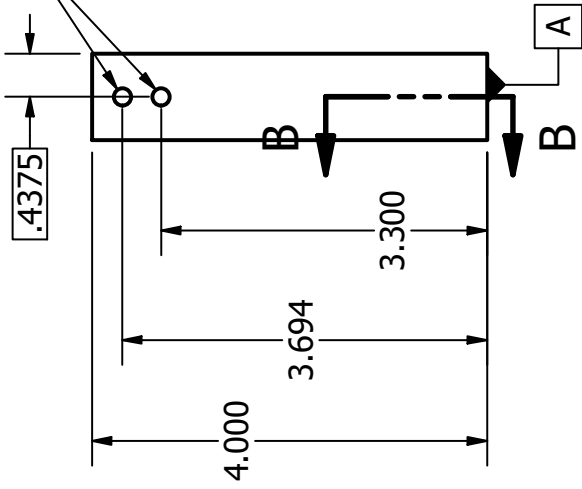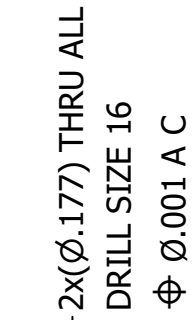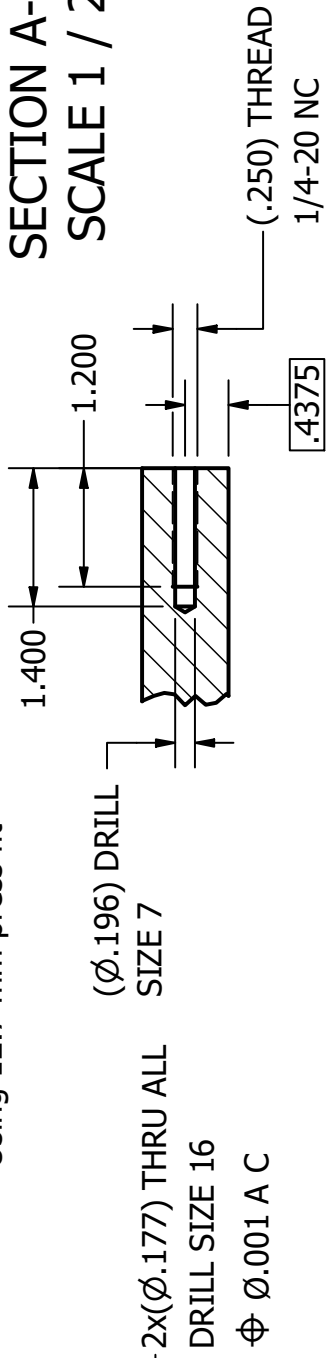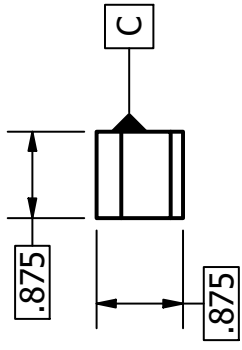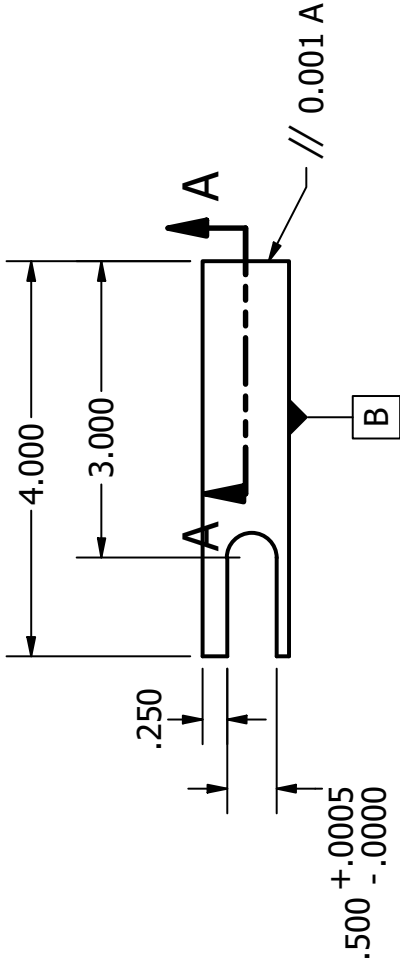
In the given order of the drawings the following pieces are represented:

• the main block to be connected to the unislide;

• the plate on which the frontal flag top support is screwed on;

• the frontal flag top support, the unconventional form of the slot which hosts the load cell has a precise purpose, since the load cell's holes have a thread they will be touching the thickest wall and will be kept in place mainly thanks to the friction force on that surface, but to avoid mechanical vibrations due to loose connections some nuts are placed on the outer part of the thinnest surface to guarantee contact on both sides of the load cell.

• the rear flag top support, it is long in order for the rear flag to be able to go deep in the water;

• the part which connects the load cell to the flag's mast;

• assembly of the frontal support;

• assembly of the rear support, in this drawing element number 1, which is the rear flag top support, will be screwed on the main block.

The mast consists in two metal stripes (element 2 in the frontal support assembly drawing) which fit the thinnest slot of the connection piece. Their drawings are not reported because trivial, more important is their manufacturing process. They are cut with a water jet from an aluminum sheet of the desired thickness, since the sheet has its own residual curvature the stripes will not be perfectly flat, but their residual bending can be annihilated by coupling them in the proper way.

5.984

5.622

4.614

3.976

3.484

A

A

A

B

2.500

2.008

1.371

.362

.659

1.250

1.841

2.500

SECTION A-A
SCALE 1 / 2

2.598 MIN

4xØ.413

2XØ.164 (THREAD 8-32 NC)
⊕ Ø0.002 A B

⬦ 0.005 C

.900

1.000

.498

90°

4xØ.257 ± .002 THRU ALL
⊕ Ø0.004 Ⓜ A B

C

| Author name: | Checked by: | Scale: | Quantity | Date |
| ANTONIO | | 1:2 | 1 | 13/02/2023 |

UNISLIDE CONNECTION

AFRG

| Material |
| ALUMINUM |

SECTION A-A
SCALE 1 : 1

Ø.266

Ø.507

82°

4XØ.266 ALL THROUGH

3.00

1.50

.50

.50

1.50

3.00

.25

0.005 A

*Note: all measures are in inches and
all dimensional tolerances are ±0.02 in
if they are not otherwise specified

Author name: ANTONIO	Checked by:	Scale: 1:1	Quantity 1	Date 17/03/2023	PLATE
				AFRG	Material ALUMINUM
				1	

SECTION A-A
SCALE 1 / 2

// 0.001 A

A

B

4.000

3.000

.250

.500 + .0005 - .0000

Using 12.7 mm press fit

(∅.196) DRILL   SIZE 7

1.200

1.400

.4375

(.250) THREAD
1/4-20 NC

All measurements
are in inches,
tolerances which
are not specified
can be assumend to
be ±0.02 inches

SECTION B-B
SCALE 1 / 2

.4375

C

.875

.875

2x(∅.177) THRU ALL
DRILL SIZE 16
⌖ ∅.001 A C

.4375

B

A

B

3.300

3.694

4.000

2X(∅.170) THRU ALL
DRILL SIZE 16
⌖ ∅.001 Ⓜ A B

.132

82°

SECTION A-A
SCALE 1 / 2

.500 $^{+.0005}_{-.0000}$
Using 12.7 mm
press fit

1.000

.125

C

All measurements
are in inches,
tolerances which
are not specified
can be assumend
to be ±0.02
inches

A

.4375

B

15.194

14.800

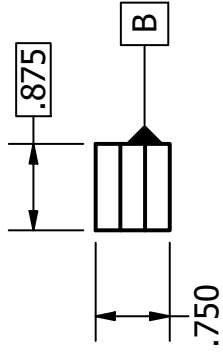2X(∅.177) THRU ALL
DRILL SIZE 16
⌖ ∅.001 Ⓜ A B

A

A

.500

1.484

15.500

.875

.875

.694

.300

2x(∅.177) THRU ALL
DRILL SIZE 16

⌖ ∅.001 Ⓜ A C

3.000

1.500

C

.375

.250 +.001 / -.000

B

.875

.750

2X(∅.129) THRU ALL, DRILL SIZE 30

⌖ ∅.001 Ⓜ A B

A

.4375

1.000

.250

.500

1.200

2.000

3.000

.500 +.0005 / -.0000
Using 12.7 mm
press fit

All measurements are in inches,
tolerances which are not specified
can be assumend to be ±0.02 inches

ELENCO PARTI			
ELEMENTO	QTÀ	NUMERO PARTE	DESCRIZIONE
1	1	Front plate	
2	2	Beam_top	
3	1	Frontal_support	
4	1	Load_cell	
5	1	Connection	
6	3	92210A416	18-8 Stainless Steel Hex Drive Flat Head Screw
7	2	92095A201	Button Head Hex Drive Screw
8	2	93695A120	Left-Hand Threaded Medium-Strength Steel Hex Nut
9	4	97654A215	18-8 Stainless Steel Flanged Button Head Screw
10	4	90592A090_Steel Hex Nut M4	Steel Hex Nut
11	1	92210A542	18-8 Stainless Steel Hex Drive Flat Head Screw
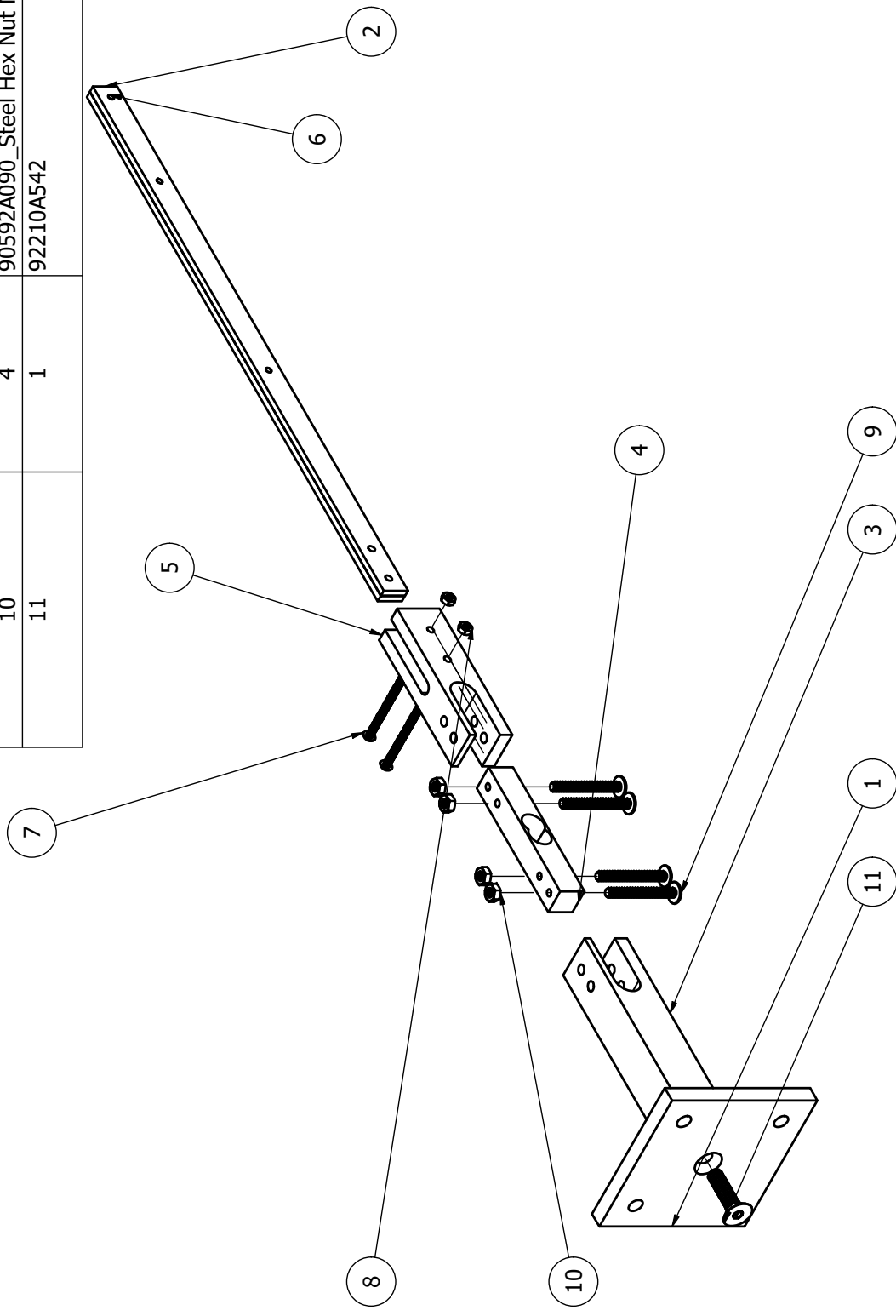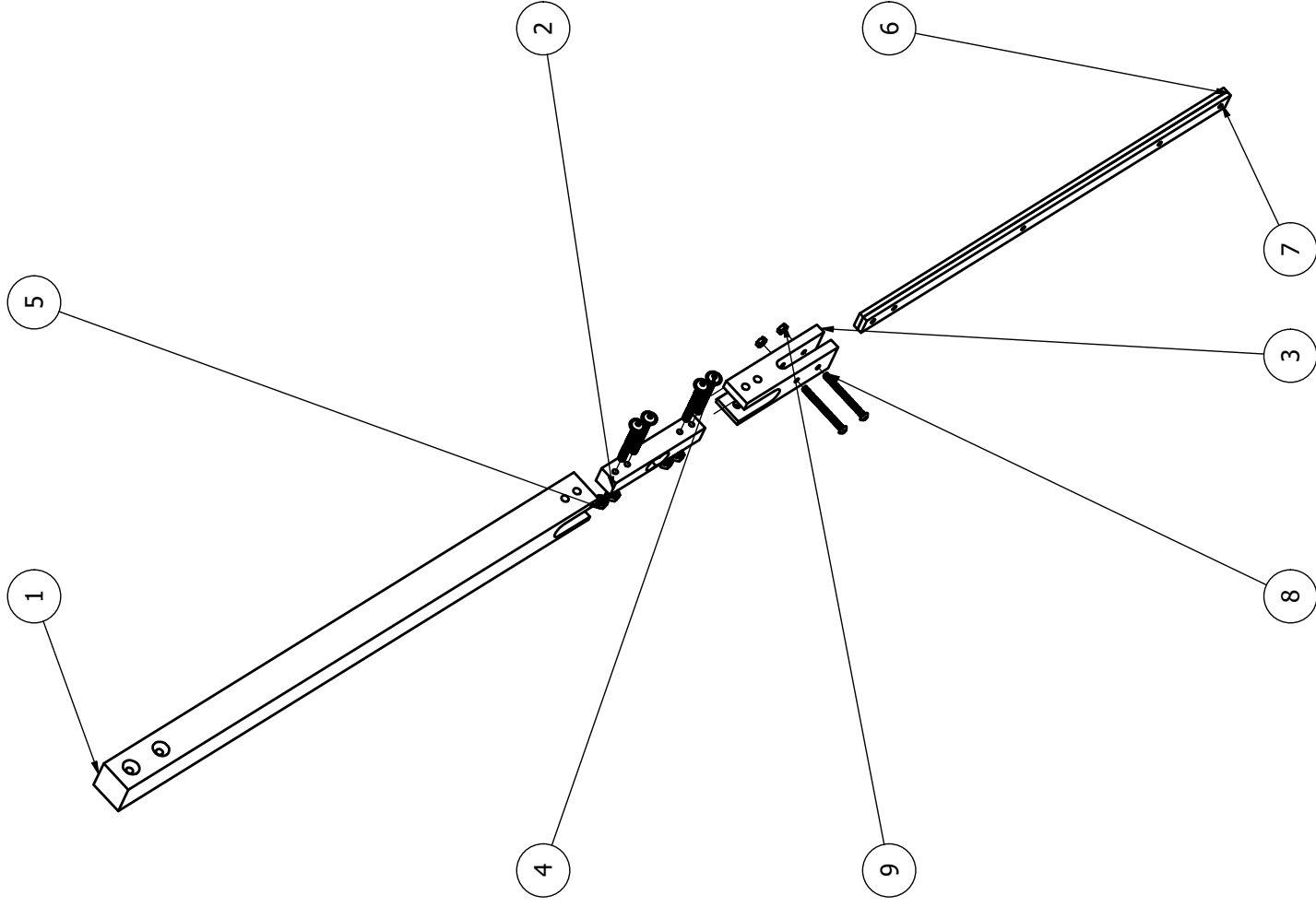
| ELENCO PARTI			
ELEMENTO	QTÀ	NUMERO PARTE	DESCRIZIONE
1	1	Frontal_support	
2	1	Load_cell	
3	1	Connection	
4	4	97654A215	18-8 Stainless Steel Flanged Button Head Screw
5	4	90592A090_Steel Hex Nut M4	Steel Hex Nut
6	2	Beam_top	
7	3	92210A416	18-8 Stainless Steel Hex Drive Flat Head Screw
8	2	92095A201	Button Head Hex Drive Screw
9	2	93695A120	Left-Hand Threaded Medium-Strength Steel Hex Nut

Appendix B

Equipment specifications

B.1   Tal221 load cell

• 500g range silver tone aluminum wired weighing load cell, high accuracy, simple structure, easy installation.

• The surface is anodized to make the product more lustrous and durable. Secondly, the product is protected by silica gel, which can protect against corrosion, moisture and aging.

• Widely used for electronic scales and balance material scales, jewelry scales and control system.

• Wire connection: Red(EXC+), Black(EXC−), Green(SEN+), White(SEN−); Sensitivity(mV/V):0.7±0.15, Error:±0.05 F.S.

• Load Cell Size: 47 x 12 x 6mm (L*W*T).

B.2   ShangHJ 1 kg load cell
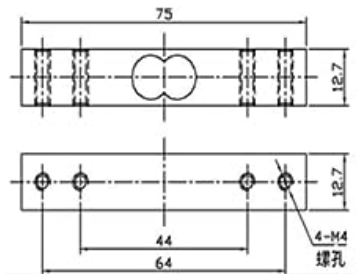
Application	Kitchen scale
Capacity	1kg
Rated output	1.0±0.1mV/V
Nonlinearity	0.03%F.S
Hysteresis	0.03%F.S
Repeatability	0.03%F.S
Creep	0.05%F.S/3min
Zero balance	-0.15±0.05mV/V
Output resistance	1000±10Ω
Corner load error	0.05%F.S
Temperature effect on sensitivity	0.03%F.S/10℃
Temperature effect on zero	0.3%F.S/10℃
Recommended excitation voltage	5V
Operating temperature range	-20∼+65℃
Product size	75x12.7x12.7mm
Load cell material	Aluminium
Method of connecting wire	red Input(+), black Input(-), green output(+), white output(-).

Figure B.1: Drawings and specifics of the load cell

96

B.3 EMBSGB200 Tacuna amplifier

• Factory calibration included - field calibration not required
• Optional 5V only, 6-16V, 8-24V power supply options
• 5V Bridge excitation
• Flexible on-board bridge completion resistor options (sold separately)
– Through hole
– Surface mount (0805 package)
– Prototyping DIP socket (pluggable)
• Precision gain (<0.1% tolerance typical) - actual gain noted on back label
• Configurable gain: 110, 220, 550, 1100, 2200, 5500, 11000
• Manual or programmable gain
– Manual: DIP switch controlled
– RS-232 controlled
• Gain can be customized at time of order 1/11 to 2 times gain range above
• Manual or programmable output offset
– Manual: Potentiometer controlled
– RS-232 controlled
• Variety of outputs available
– 0-5V
– 0-5V and 4-20mA
– RS-232 12bit Digitized ADC
• Noise elimination filter
– Factory default low-pass: -3 dB at 60 Hz with 350 bridge
– Factory adjustable, per request
– User configurable with modification
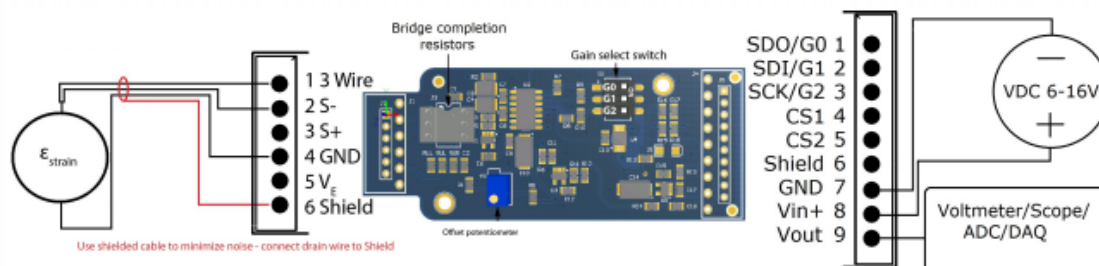• Dimensions: 1.3" x 3.3"

Figure B.2: Tacuna amplifier wiring scheme

B.4 DMD4059 Omega amplifier

• Strain Gauge Input Ranges
-100 Ω to 10,000 Ω bridges at 10 VDC
-Up to four 350 Ω bridges at 10 VDC
Minimum: 0 to 5 mV range 0.5 mV/V sensitivity
Maximum: 0 to 400 mV range 40 mV/V sensitivity
• Excitation Voltage
-Switch Selectable: 0-10 VDC in 1 V increments
-Maximum Output: 10 VDC maximum at 120 mA
-Drive Capability: Up to four 350 Ω bridges at 10 VDC
-Fine Adjustment: $\pm5\%$ via multi-turn potentiometer
-Stability: $\pm0.01\%$ per ºC
• Sense Lead Compensation
-Better than $\pm0.01\%$ per 1 Ω change in leadwire resistance
-Maximum leadwire resistance: 10 Ω with 350 Ω at 10 VDC
• LoopTracker Variable brightness LEDs for input/output loop level and status

• DC Output Ranges
-Voltage (10 mA max.): 0-1 VDC to 0-10 VDC
Bipolar Voltage (±10 mA max.): ±5 VDC or ±10 VDC
-Current: 0-2 mADC to 0-20 mADC
-Compliance, drive at 20 mA: 20 V, 1000 ± drive
• Output Calibration
Multi-turn zero and span potentiometers ±15% of span adjustment range typical Zero
offset switch: ±100% of span in 15% increments
• Output Ripple and Noise
Less than 10 mVRMS ripple and noise
• Linearity
Better than ±0.1% of span
• Ambient Temperature Range and Stability –10°C to +60°C operating ambient
Better than ±0.02% of span per ^{o}C stability
• Response Time
70 milliseconds typical (14.2 Hz) DF option: 10 millisecond (100 Hz) response time
typical
• Dimensions
0.89" W x 4.62" H x 4.81" D
• Power
-Standard: 85-265 VAC, 50/60 Hz or 60-300 VDC
-D option: 9-30 VDC (either polarity) or 10-32 VAC
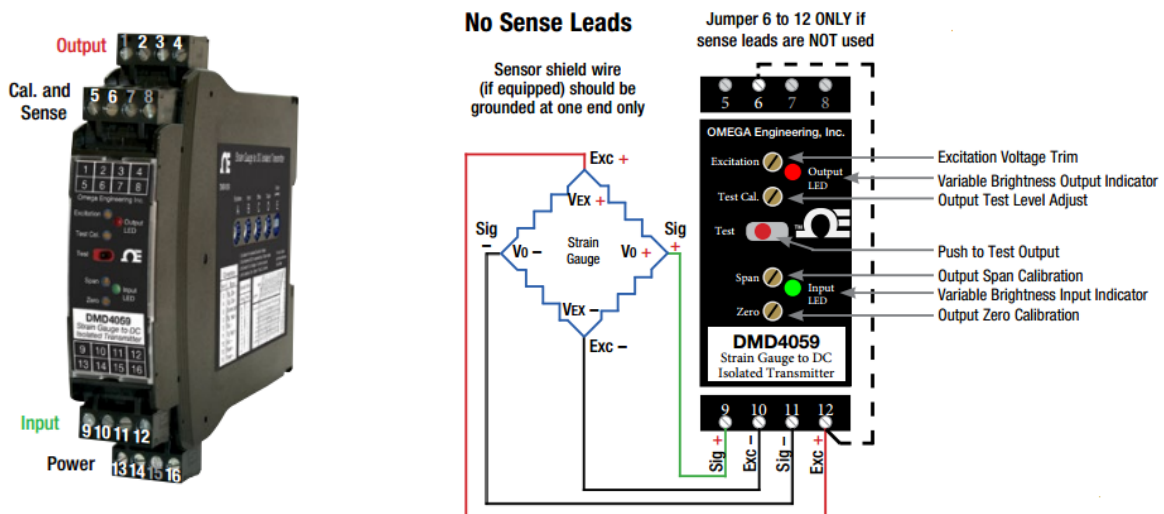-Power: 2 to 5 Watts depending on number of load cells.

Figure B.3: Omega amplifier wiring scheme

B.5 VEO phantom camera 640

Figure B.4: VEO phantom camera 640

	VEO 710 VEO 410	VEO 640 VEO 340	VEO4K 990 & PL VEO4K 590
Max. Resolution	1280 x 800	2560 x 1600	4096 x 2304
FPS @ Max Res	7400 fps (710); 5200 fps (410)	1400 fps (640); 800 fps (340)	938 fps (990); 530 fps (590)
Throughput	7Gpx/sec (710); 5Gpx/sec (410)	6Gpx/sec (640); 3Gpx/sec (340)	9Gpx/sec (990); 5Gpx/sec (590)
Sensor Size @ Full Res	25.6 x 16 mm (super 35mm)		27.6 x 15.6 mm
Pixel Pitch	20 micron	10 micron	6.75 micron
CAR	64 x 8	128 x 4	4096 x 4
Min. Exposure	1 µs standard, 300ns optional on 710 models only		5.6 µs
Straddle Time	395 ns (710); 480 ns (410)	1.73 µs (640); 1.71 µs (340)	7.5 µs (typical) 3.7 µs w/ GS & PIV mode
Native ISO (12232 SAT Method)	Mono: 6400 Color: 2000	Mono: 6400 Color: 1250	Mono: 2500 (GS); 1000 (RS) Color: 640 (GS); 320 (RS)
Recommended Exposure Index (E.I.)	Mono: 6400 - 40,000; Color: 2000 - 10,000	Mono: 6400 - 40,000; Color: 1250 - 6400	Mono: 4000 - 8000 (RS/GS) Color: 800 - 1000 (RS/GS)
Memory	18GB, 36GB or 72GB RAM		36GB or 72GB RAM
Power	16-32 VDC primary power, power supply included. Secondary 12V input on S-models only		
Size/Weight	Approx. 5 x 5.5 x 5 in (12.7 x 12.7 x 12.7 cm) 5.6 lbs (2.5 kg)		Approx. 5 x 5.5 x 6 in (12.7 x 14 x 15 cm) 6.5 lbs (2.9 kg)
Operational Temp	-10° - +50° C		
Shock Rating	Rated 30G (standard); 100G without shutter (optional)		

	Ethernet	Video	OCC/ Buttons	CFast Media	Programmable I/O	Range Data
'L' style	1 GbE with 10GbE option, RJ45 port	Front 3G SDI Din & HDMI	None	None	2 Ports	None
'S' style	1 GbE with 10GbE option, Fischer port	Same as L w/ additional 3G SDI BNC	Full OCC menu + Trigger & Play buttons	Supports CFast 2.0 cards up to 256G	4 Ports	Yes, Dedicated Fischer port

Figure B.5: VEO phantom camera specifics

B.6 Lens

Dimensions	2.5 x 2.5 x 1.54 inches
Item Weight	5.50 ounces
Lens Type	Standard
Maximum aperture	20 mm
Maximum focal length	50 mm
Minimum aperture	0 mm
Minimum focal length	50 mm

Table B.1: Lens specifics

Figure B.6: Nikon nikkor lens af nikkor 50mm f/1.8D

Appendix C

Extra parts

C.1   Pulley system

The pulley system is depicted in figure C.1. It was built by 3D printing the pulley support and its wheel with ABF. To reduce as much as possible the friction a high ratio of outer over inner diameter was selected, moreover a smooth metal pin was used to bear the wheel, while some metal washers have been used to keep the wheel far from the lateral walls. The hook was 3D printed with ABF as well, figure C.2, it has been designed to fit the upper part of the connecting element and to apply the load perpendicularly to the load cell.
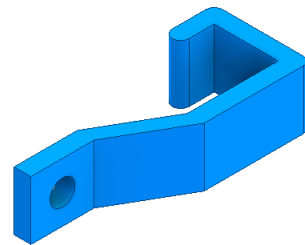

Figure C.1: Pulley system

Figure C.2: Load cell hook

C.2 Surface plate

The plate for surface waves removal is made of ultra high molecular weight (UHMW) black colored polyethylene. It has two slots to host the flags' supports, and some aluminum T-slotted frames are used to connect it to the water tunnel frame in the test section. The aluminum frames are versatile and can be moved to modify the design, furthermore they can be disassembled to be used for other purpose.
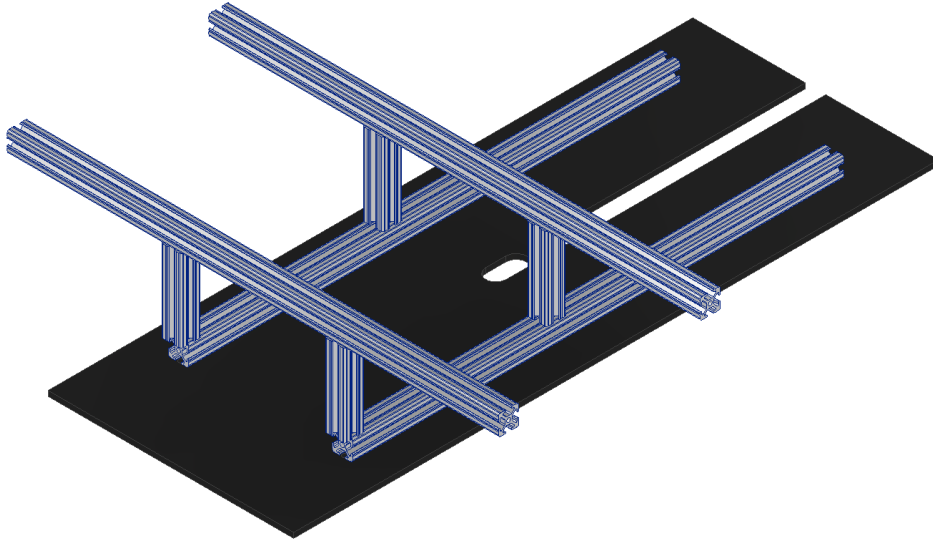
Figure C.3: Surface plate

C.3 Airfoil envelope

The wing is meant to enclose the aluminum flags' supports, which are bluff bodies. The wing hollow section hosts the aluminum bars, while some holes on its surface makes it possible to screw the bars together. A slot to host the flag is placed close to the holes, right on the leading edge. The wing airfoil is a NACA 0024, the thickness percentage needs to be high enough to fit the supports. The wings were 3D printed with blue ABF and uniformly black painted. The CAD of the wing is depicted in figure C.4.
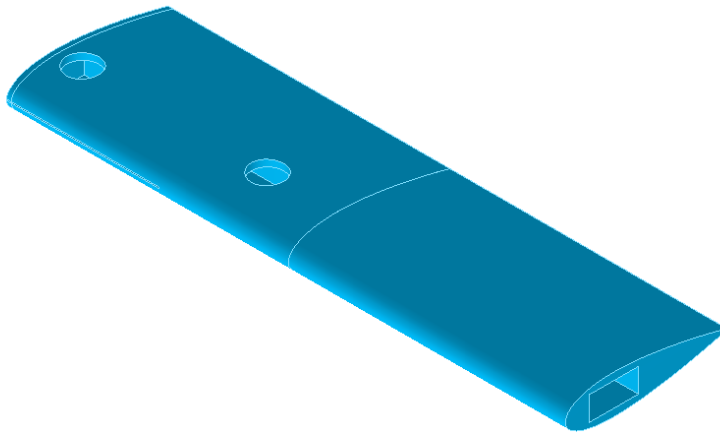
Figure C.4: Airfoil envelope

Appendix D

Software

In this section of the appendix there is an explanation about how the LabVIEW code used for the data acquisition works. LabVIEW uses a graphic interface and this makes the code quite uncomfortable to navigate when it is large and complex, for this reason the diagrams in the next two pages will look confusing. The first page contains the code block diagram for the load cell data acquisition only, while the second page reports the code used for the synchronized acquisition of data from both the load cells and the cameras.

Load cell fast acquisition This paragraph describes the code in the next page, it controls the acquisition from the load cells and the stepper motor at the same time. By starting from the outer part of the diagram, the serial communication with the VP9000 is set through the NI-VISA packet commands, a first case structure lets the user choose if controlling the motors manually without performing any data acquisitions or to start an automatic acquisition and consequent motion of the motor. In case of automatic acquisition, a 'for' loop iterates the acquisition for the number of points where the data needs to be collected. Inside the loop a frame sequence defines the events to be executed in sequence: first the motor is moved of a specific amount of steps if some conditions are satisfied, the second frame is a temporal delay of 10 seconds so that the fluid-structure transients have time to end before the data acquisition from the load cells starts in the third frame; the last frame is responsible for saving the recorded data. Before a new iteration of the frame sequence starts, a delay of two seconds is given for the system to complete the data saving. Since the stepper motor controls the vertical position of the rear flag, each automatic acquisition collects data from a configurable number of points equally Π_z spaced but at constant Π_x. This method allows a quick and precise positioning of the flag, therefore much time is saved during the acquisition considering that it allowed to acquire a whole test matrix in approximately 3 hours. Unfortunately only load cells data can be recorded, in fact the edge tracking requires the rear camera to be adjusted every time the corresponding rear flag is moved. The settings which are modified on the camera in this case are its position, its focus, its resolution and its zero intensity reference.

Synchronized acquisition: load cells + cameras This paragraph describes the code diagram for synchronizing the load cells data acquisition with the camera images. It consists in a frame sequence in which the first frame is responsible for triggering a specific counter output channel of the USB-6218 DAQ as soon as the analog input channels receive a signal from the load cells. The triggering of the counter is set by means of a property node, while the features of the counter signal can be set by the user. The sampling frequency of the analog input was set to be 50 times higher than the frames per second of the cameras, in order for the acquisition to be able to last more time. In fact acquiring at high frames per second results in fast filling of the camera memory. The second and third frame let the acquisition of the load cells' data and the counter signal generation both to reach completion, while the last frame saves the load cells' data. The images from the cameras are saved manually with the PCC software.